Effects of Material Properties on Bore Deformation of Engine Cylinder Liner

右田, 竜聖
九州大学総合理工学府環境エネルギー工学専攻

令和　3　年　度

修　　士　　論　　文

Effects of Material Properties on Bore Deformation of Engine Cylinder Liner

材料物性値が及ぼすエンジン シリンダライナのボア変形への影響

九州大学大学院総合理工学府
環境エネルギー工学専攻
熱機関工学研究室

右田　竜聖

指導教員　田島　博士　准教授

提出年月日　令和 2 年 2 月 7 日

Contents

Chapter 1. Introduction

1.1. Back ground

1.1.1. Environmental issue

Nowadays, the internal combustion engine is essential machine of human society especially for transportation. Moreover, according to *World Energy Outlook*,[1] global transportation-related energy demand is expected to grow by more than 25 percent from 2017 to 2040. With this growing demand, the global environmental issue, especially global warming, should be considered seriously. The greenhouse gas (GHG) emission from these internal combustion engines is one of the biggest factors of global warming. In order to improve this problem, the Paris Agreement has been built in 2015.[2] This protocol is next protocol of Kyoto Protocol which is established in 1997.[3] This Paris Agreement represents the realization of Zero-carbon(emission) society by 2075. This is based on the scientific theory indicated by IPCC (Intergovernmental Panel on Climate Change).[4] According to IPCC report 2018, global average temperature has been increased by 1℃ since industrial revolution because of human life. It is also said that, the global temperature is predicted to be increased by 1.5℃ until 2030, and 4℃ until 2050 if this economic activity keeps working. In order to suppressed this global average temperature increasing by 1.5℃, the zero-carbon society has to be realized until 2050. Paris Agreement published the regulation of emission every 5 years to each country including developed and developing country, based on this scientific theory.

To achieve this regulation, increasing the efficiency of internal combustion engine has still significant potential because the World Energy Outlook expects the demand of internal combustion engines for the transportation sector will still increase all over the world.[1]

1.1.2. Conformability between piston-rings and cylinder liner

There is much possibility to improve the efficiency of internal combustion engine. One way is to improve the conformability between piston-rings and cylinder liner.[5][6] Fig.1-1 shows the simple mechanism of the tribology including piston, three piston-rings and cylinder liner. The lubrication oil is packed between the piston-rings and cylinder liner. So, if conformability of them is not good, the lubrication oil will leak toward crankcase, which is known as blow-by, or back to chamber, which is known as blow-back. This leads to increase of the lubrication oil consumption (LOC). This property is important factor for the reduction of the GHG and efficiency. It is said that lubrication oil accounts for 20~50% of exhaust gas particles from the engine.[7] This means, for example, if the LOC is high, not only even abnormal wear could be occurred between them and friction losses in the engine would be increased, but also this leads to increased GHG emission.[8][9]

To conquer this theme, it is necessary to improve both performance of the piston-rings and cylinder liner. On one hand, piston rings tightness should be high appropriately. If this tightness

is not enough high, lubrication oil cannot be sealed perfectly and will leak. But also, too much tightness leads more friction losses from the engine and more GHG.[8] However, it is current issue that higher piston rings tightness is necessary to cover the clearance between piston rings and cylinder liner due to the bore deformation of the cylinder liner. Actually, the bore of the cylinder liner cannot be perfect cylindrical shape in high temperature and pressure condition like engine operation. This means that suppression of this bore deformation has the significant potential to reduce the GHG emission and friction losses, ultimately leads to higher efficiency, because the possibility to improve the piston rings ability is limited.[10]

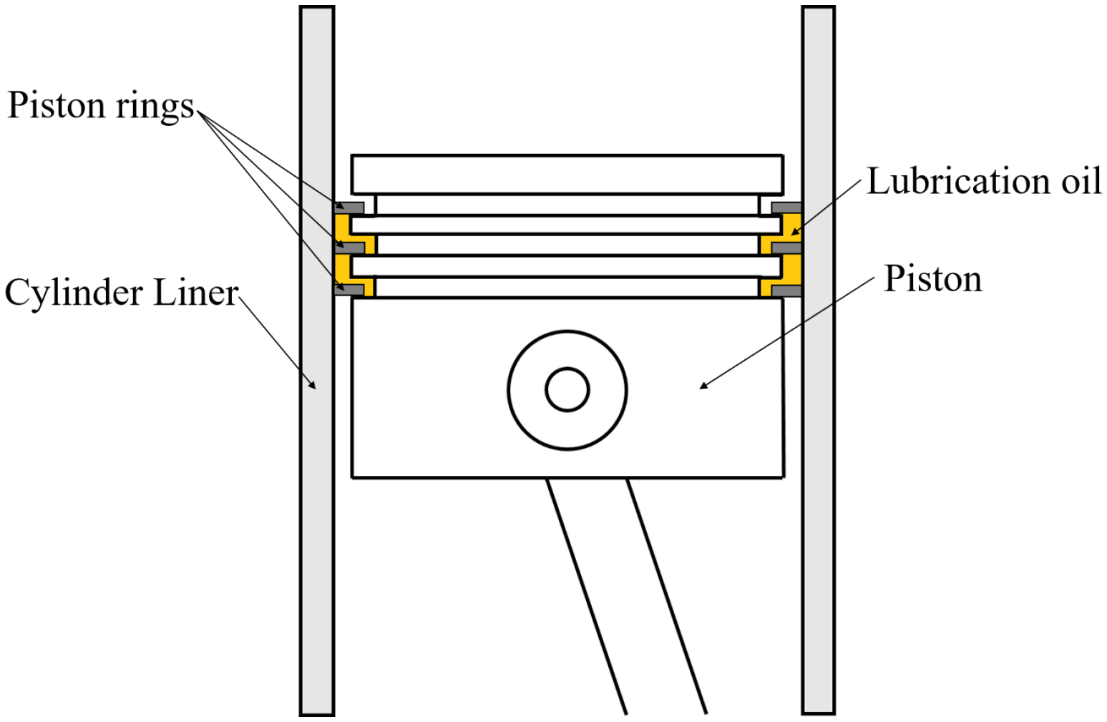

Fig.1-1

1.2. Purpose of study

In order to suppress the bore deformation of the cylinder liner, there are two types of possible approaches. One is geometric modification of the cylinder liner, which is investigated using simulation by Alshwawra A. [11][12] Another is material modification of that and this is the topic of this thesis. Recently, gray cast iron is used for cylinder liner considering wear resistance and low thermal expansion coefficient. Besides, gray cast iron or aluminum alloy is used for cylinder block considering low density and cost for assemble process.

In this investigation, the simulation model for this thermal and mechanical bore deformation of the liner has been built. Moreover, it is investigated how this bore roundness would change if material property is operated using this simulation model. Only the simulation is the possible to conduct this kind of investigation like operating only each property of materials, because this cannot be conducted experimentally.

That is why, the purpose of this study is to find the best each material property for the cylinder liner and block, and make it basic concept to develop the new future material for them.

Chapter 2. Calculation and simulation model

2.1. Finite element method (FEM)

In this section, the overflow of FEM is expressed. The simple algorithm is shown as Fig. 2-2. First of all, the solid model for analysis is divided into small elements as shown in Fig.2-1. Next, the boundary conditions like material property, thermal load or pressure are set as pre-process. FEM starts from this step. Firstly, based on the boundary condition and equation (2.1.1), calculate element stiffness matrix $[K_e]$ about each element meshed by pre-process.

$$[K_e]\{u_e\} = \{F_e\} \tag{2.1.1}$$

$\{u_e\}$: nodal displacement vector

$\{F_e\}$: nodal applied load vector as boundary condition

With the superposition of this $[K_e]$, global stiffness matrix $[K]$ is calculated. Next, the surface stress vector is integrated and the global nodal load vector $\{F\}$ is calculated. Through this process, the huge simultaneous linear equation (2.1.2) can be written below.

$$[K]\{u\} = \{F\} \tag{2.1.2}$$

Solving this linear equation, the nodal displacement vector $\{u\}$ is calculated. Moreover, by strain-displacement relationship equation (2.1.3) and stress-strain relationship equation (2.1.4), each element stress and strain are calculated.

$$\{\varepsilon\} = [B]\{u\} \tag{2.1.3}$$

$$\{\sigma\} = [D]\{\varepsilon\} \tag{2.1.4}$$

Finally, the result is visualized by post process software as output.

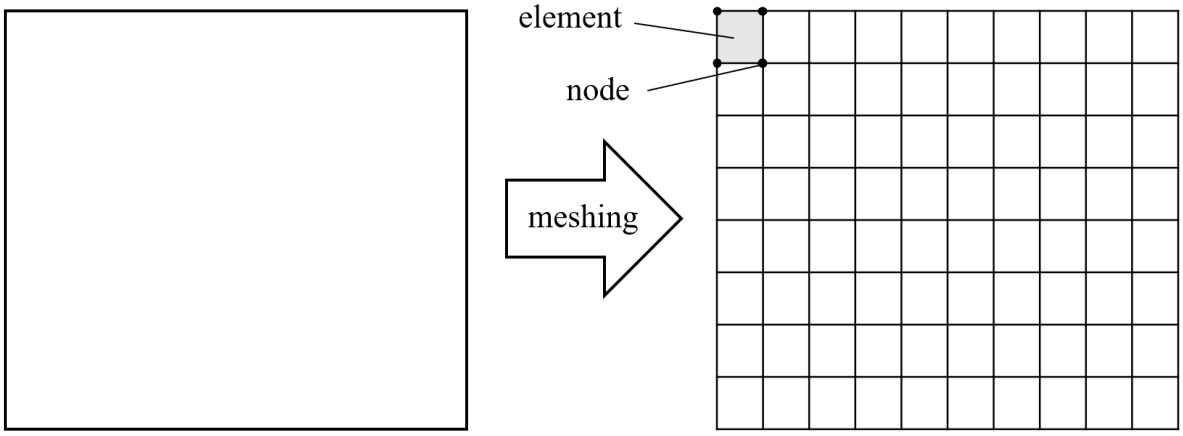

Fig. 2-1 meshing

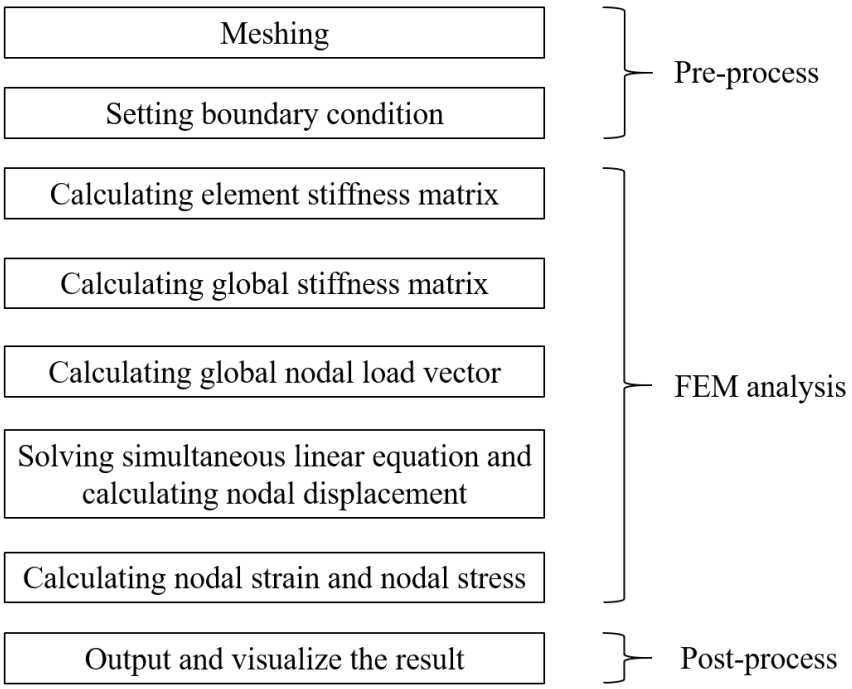

Fig.2-2 algorithm of FEM

2.2. ANSYS MECHANICAL

ANSYS MECHANICAL is one tool of ANSYS software products to simulate mechanical phenomenon based on the finite element method (FEM). In this investigation, ANSYS MECHANICAL APDL 2019.R3 is used. The calculation mechanism is based on following dominant equation.[13]

2.2.1. Thermal-structural coupled field analysis method

In this investigation, the simulation for the liner deformation must be calculated considering both of the thermal and mechanical load, so the thermal-structural coupled field analysis is necessary. In ANSYS MECHANICAL, there are two types of coupled field calculation methods, which are strong coupling and weak coupling. The program automatically controls to use better method for each simulation model, so the operator doesn't have to care which method is better for each simulation. But each method can be specified on the purpose. The detail of these methods is shown as following.

i). Strong coupling

The matrix equation is the form shown as following:

$$\begin{bmatrix}[M] & [0]\\ [0] & [0]\end{bmatrix}\begin{Bmatrix}\{\ddot{u}\}\\ \{\ddot{T}\}\end{Bmatrix}+\begin{bmatrix}[C] & [0]\\ [C_{tu}] & [C_t]\end{bmatrix}\begin{Bmatrix}\{\dot{u}\}\\ \{\dot{T}\}\end{Bmatrix}+\begin{bmatrix}[K] & [K_{ut}]\\ [0] & [K_t]\end{bmatrix}\begin{Bmatrix}\{u\}\\ \{T\}\end{Bmatrix}=\begin{Bmatrix}\{F_{nd}\}+\{F_{pr}\}+\{F_{ac}\}\\ \{Q_{nd}\}+\{Q_g\}+\{Q_c\}\end{Bmatrix} \quad (2.2.1)$$

Where:

$[M]$: element mass matrix

$[C]$: element structural damping matrix

$[C_t]$: element specific heat matrix

$[C_{tu}]$: element thermoelastic damping matrix

$[K]$: element structural stiffness matrix

$[K_t] = [K_{tb}] + [K_{tc}]$: element thermal conductivity matrix

$[K_{tb}]$: element diffusion conductivity matrix

$[K_{tc}]$: element convection surface conductivity matrix

$[K_{ut}]$: element thermoelastic stiffness matrix

$\{F_{nd}\}$: applied nodal force vector as boundary condition

$\{F_{pr}\}$: pressure load vector

$\{F_{ac}\}$: force vector caused by acceleration effects

$\{Q_{nd}\}$: applied nodal heat flow rate vector as boundary condition

$\{Q_g\}$: heat generation rate vector for causes other than Joule heating

$\{Q_c\}$: element convection surface heat flow vector

This method provides for a coupled response in the solution after one iteration.

ii). Weak coupling

The matrix equation is the form shown as following:

$$\begin{bmatrix}[M] & [0]\\ [0] & [0]\end{bmatrix}\begin{Bmatrix}\{\ddot{u}\}\\ \{\ddot{T}\}\end{Bmatrix}+\begin{bmatrix}[C] & [0]\\ [0] & [C_t]\end{bmatrix}\begin{Bmatrix}\{\dot{u}\}\\ \{\dot{T}\}\end{Bmatrix}+\begin{bmatrix}[K] & [0]\\ [0] & [K_t]\end{bmatrix}\begin{Bmatrix}\{u\}\\ \{T\}\end{Bmatrix}=\begin{Bmatrix}\{F_{nd}\}+\{F_{pr}\}+\{F_{ac}\}+\{F_{th}\}\\ \{Q_{nd}\}+\{Q_g\}+\{Q_c\}+\{Q_{ted}\}\end{Bmatrix} \quad (2.2.2)$$

Where:

$\{F_{th}\}$: thermal strain force vector

$\{Q_{ted}\}$: heat generation rate vector for thermoelastic damping

At least two iterations are required to achieve a coupled response.

The derivation methods of each matrix of equation (2.2.1) and (2.2.2) are described below.

2.2.2. Dominant equation for stress and strain

Firstly, the strain can be divided into elastic strain and thermal strain.

$$\{\varepsilon\} = \{\varepsilon_{el}\} + \{\varepsilon_{th}\} \quad (2.2.3)$$

The basic dominant equation for stress-strain relationship is following:

$$\{\sigma\} = [D]\{\varepsilon_{el}\} \quad (2.2.4)$$

$$\{\sigma\} = \text{stress vector} = \{\sigma_x\ \sigma_y\ \sigma_z\ \sigma_{xy}\ \sigma_{yz}\ \sigma_{zx}\}^t \quad (2.2.5)$$

Where: $\sigma_x,\ \sigma_y,\ \sigma_z$ is normal strain and $\sigma_{xy},\ \sigma_{yz},\ \sigma_{zx}$ is shear strain, as shown Fig.2-3.

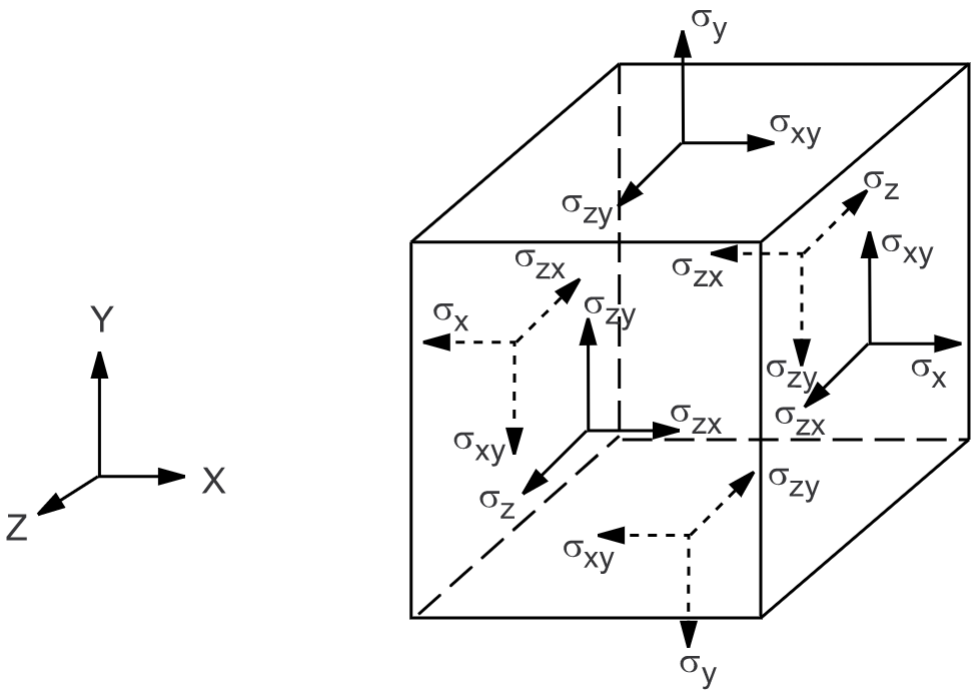

Fig.2-3. Stress tensor

With equation (2.2.3) and (2.2.4),

$$\{\varepsilon\} = \{\varepsilon_{th}\} + [D]^{-1}\{\sigma\} \tag{2.2.6}$$

$$[D]^{-1} = \begin{bmatrix} 1/E_x & -\nu_{xy}/E_x & -\nu_{xz}/E_x & 0 & 0 & 0 \\ -\nu_{yx}/E_y & 1/E_y & -\nu_{yz}/E_y & 0 & 0 & 0 \\ -\nu_{zx}/E_z & -\nu_{zy}/E_z & 1/E_z & 0 & 0 & 0 \\ 0 & 0 & 0 & 1/G_{xy} & 0 & 0 \\ 0 & 0 & 0 & 0 & 1/G_{yz} & 0 \\ 0 & 0 & 0 & 0 & 0 & 1/G_{zx} \end{bmatrix} \tag{2.2.7}$$

Where typical terms are:

E_x : Young's modulus in the x direction

ν_{xy} : major Poisson's ratio

ν_{yx} : minor Poisson's ratio

G_{xy} : shear modulus in the xy plane

The difference between ν_{xy} and ν_{yx} is described below.

$$\frac{\nu_{yx}}{E_y} = \frac{\nu_{xy}}{E_x} \tag{2.2.8}$$

$$\frac{\nu_{zx}}{E_z} = \frac{\nu_{xz}}{E_x} \tag{2.2.9}$$

$$\frac{\nu_{zy}}{E_z} = \frac{\nu_{yz}}{E_y} \tag{2.2.10}$$

The thermal strain $\{\varepsilon_{th}\}$ can be expressed as following:

$$\{\varepsilon_{th}\} = \Delta T\{\alpha_x \quad \alpha_y \quad \alpha_z \quad 0 \quad 0 \quad 0\}^t \tag{2.2.11}$$

$$\Delta T = T - T_{ref} \tag{2.2.12}$$

Where typical terms are:

α_x : average (secant) thermal expansion coefficient in the x direction (see chapter 2.2.3. for temperature-dependent thermal expansion coefficient)

T : current temperature at the point in question

T_{ref} : reference (strain-free) temperature

Expanding equation (2.2.6) with equation (2.2.7) through (2.2.11),

$$\varepsilon_x = \alpha_x \Delta T + \frac{\sigma_x}{E_x} - \frac{\nu_{xy}\sigma_y}{E_x} - \frac{\nu_{xz}\sigma_z}{E_x} \tag{2.2.13}$$

$$\varepsilon_y = \alpha_y \Delta T - \frac{\nu_{yx}\sigma_x}{E_y} + \frac{\sigma_y}{E_y} - \frac{\nu_{yz}\sigma_z}{E_y} \tag{2.2.14}$$

$$\varepsilon_z = \alpha_z \Delta T - \frac{\nu_{zx}\sigma_x}{E_z} - \frac{\nu_{zy}\sigma_y}{E_z} + \frac{\sigma_z}{E_z} \tag{2.2.15}$$

$$\varepsilon_{xy} = \frac{\sigma_{xy}}{G_{xy}} \tag{2.2.16}$$

$$\varepsilon_{yz} = \frac{\sigma_{yz}}{G_{yz}} \tag{2.2.17}$$

$$\varepsilon_{zx} = \frac{\sigma_{zx}}{G_{zx}} \tag{2.2.18}$$

Based on these equations (2.2.13) through (2.2.18), the ANSYS MECHANICAL is solving the structural calculation.

2.2.3. Temperature-dependent instantaneous thermal expansion coefficient

With equation (2.2.11) and assumption that thermal expansion is same in each x, y, z directions, the general thermal strain can be expressed as following:

$$\varepsilon_{th} = \alpha(T)\big(T - T_{ref}\big) \tag{2.2.19}$$

If the temperature-dependent instantaneous thermal expansion coefficient $\alpha_{in}(T)$ is applied for certain material property, with the input parameter $\alpha_{in}(T)$, the average thermal expansion coefficient $\alpha(T)$ can be calculated as following:

$$\alpha(T) = \frac{\int_{T_{ref}}^{T} \alpha_{in}(T)dT}{T - T_{ref}} \tag{2.2.20}$$

Therefore, with equation (2.2.19) and (2.2.20), ultimately thermal strain can be converted as following:

$$\varepsilon_{th} = \int_{T_{ref}}^{T} \alpha_{in}(T)dT \tag{2.2.21}$$

Based on this (2.2.21) equation, the equation (2.2.13) through (2.2.15) can be calculated.

2.2.4. Derivation of Structural matrices

The principle of virtual work states that a virtual very small change of the internal strain energy must be external work due to the applied loads as boundary condition. Therefore,

$$\delta U = \delta W \tag{2.2.22}$$

$$\delta U = \delta U_1 + \delta U_2 \tag{2.2.23}$$

$$\delta W = \delta W_1 + \delta W_2 + \delta W_3 \tag{2.2.24}$$

δU : virtual change of the internal strain energy

δW : external work

The virtual strain energy is:

$$\delta U_1 = \int_V \{\delta\varepsilon\}^t \{\sigma\} dV \tag{2.2.25}$$

From equation (2.2.6):

$$\{\sigma\} = [D]\{\varepsilon\} - [D]\{\varepsilon_{th}\} \tag{2.2.26}$$

With equation (2.2.26), equation (2.2.25) is converted to following:

$$\delta U_1 = \int_V (\{\delta\varepsilon\}^t [D]\{\varepsilon\} - \{\delta\varepsilon\}^t [D]\{\varepsilon_{th}\}) dV \tag{2.2.27}$$

From equation (2.1.3), the strains can be related to the nodal displacements.

$$\delta U_1 = \{\delta u\}^t \int_V [B]^t [D][B] dV \{u\} - \{\delta u\}^t \int_V [B]^t [D]\{\varepsilon_{th}\} dV \tag{2.2.28}$$

Another form of virtual strain energy is when a surface moves against a distributed resistance. This can be written as:

$$\delta U_2 = \int_S \{\delta w_n\}^t \{\sigma_n\} dS \tag{2.2.29}$$

δw_n : very small vertical motion to the surface

σ_n : stress or pressure carried by the surface

This point-wise vertical displacement is related to the nodal displacements by:

$$\{w_n\} = [N_n]\{u\} \tag{2.2.30}$$

$[N_n]$: matrix of shape functions for vertical motions at the surface

Moreover:

$$\{\sigma_n\} = k\{w_n\} = k[N_n]\{u\} \tag{2.2.31}$$

k : the foundation stiffness in units of force per length per unit area

With equation (2.2.30) and (2.2.31), the equation (2.2.29) is converted to following:

$$\delta U_2 = k\{\delta u\}^t \int_S [N_n]^t [N_n] dS \{u\} \tag{2.2.32}$$

Next, the external virtual work will be considered. The inertial effects will be studied first:

$$\delta W_1 = -\int_V \{\delta w\}^t \frac{\{F_a\}}{V} dV \tag{2.2.33}$$

$\{w\}$: vector of displacements of a general point

$\{F_a\}$: acceleration (D'Alembert) force vector

According to Newton's second law:

$$\frac{\{F_a\}}{V} = \rho \frac{\partial^2 \{w\}}{\partial t^2} \tag{2.2.34}$$

The displacements within the element are related to the nodal displacements by:

$$\{w\} = [N]\{u\} \tag{2.2.35}$$

$[N]$: matrix of shape functions

With equation (2.2.34) and (2.2.35), equation (2.2.33) is converted to following:

$$\delta W_1 = -\{\delta u\}^t \rho \int_V [N]^t [N] dV \frac{\partial^2 \{u\}}{\partial t^2} \tag{2.2.36}$$

The pressure force vector formulation starts with:

$$\delta W_2 = \int_S \{\delta w_n\}^t \{P\} dS \tag{2.2.37}$$

$\{P\}$: applied pressure vector

With equation (2.2.30), equation (2.2.37) will be following:

$$\delta W_2 = \{\delta u\}^t \int_S [N_n]\{P\} dS \tag{2.2.38}$$

Furthermore, nodal forces applied to the element can be accounted for by:

$$\delta W_3 = \{\delta u\}^t \{F_{nd}\}$$

$\{F_{nd}\}$: applied nodal force vector as boundary condition

Finally, equation (2.2.22) is converted to following:

$$\{\delta u\}^t \int_V [B]^t [D][B] dV \{u\} - \{\delta u\}^t \int_V [B]^t [D]\{\varepsilon_{th}\} dV + k\{\delta u\}^t \int_S [N_n]^t [N_n] dS \{u\}$$
$$= -\{\delta u\}^t \rho \int_V [N]^t [N] dV \frac{\partial^2 \{u\}}{\partial t^2} + \{\delta u\}^t \int_S [N_n]\{P\} dS + \{\delta u\}^t \{F_{nd}\} \tag{2.2.39}$$

To simplify this:

$$\left([K] + [K_f]\right)\{u\} - \{F_{th}\} = [M]\{\ddot{u}\} + \{F_{pr}\} + \{F_{nd}\} \tag{2.2.40}$$

Where typical terms are followings:

$[K] = \int_V [B]^t [D][B] dV$: element structural stiffness matrix

$[K_f] = k \int_S [N_n]^t [N_n] dS$: element foundation stiffness matrix

$[F_{th}] = \int_V [B]^t [D]\{\varepsilon_{th}\} dV$: thermal strain force vector

$[M] = \rho \int_V [N]^t[N]dV$: element mass matrix

$\{\ddot{u}\} = \frac{\partial^2\{u\}}{\partial t^2}$: acceleration vector

$\{F_{pr}\} = \int_S [N_n]\{P\}dS$: pressure load vector

2.2.5. Dominant equation for thermal conductivity and head transfer

By the first law of thermodynamics, the thermal energy has to be conserved. Thus,

$$\rho c(\frac{\partial T}{\partial t} + \{v\}^t\{\nabla\})T + \{\nabla\}^t\{q\} = \dot{H} \tag{2.2.41}$$

By Fourier's law,

$$\{q\} = -[\lambda]\{\nabla\}T \tag{2.2.42}$$

With equation (2.2.42), equation (2.2.41) can be converted as following:

$$\rho c\frac{\partial T}{\partial t} + \rho c\{v\}^t\{\nabla\}T - \{\nabla\}^t[\lambda]\{\nabla\}T = \dot{H} \tag{2.2.43}$$

Where, typical terms are,

ρ : density

c : specific heat capacity

t : time

T : temperature

v : velocity for mass transport of heat

q : heat flux

λ : thermal conductivity

$\dot{H}$: internal heat generation per unit volume

$$\{\nabla\} = \begin{pmatrix} \frac{\partial}{\partial x} \\ \frac{\partial}{\partial y} \\ \frac{\partial}{\partial z} \end{pmatrix}, \qquad \{v\} = \begin{pmatrix} v_x \\ v_y \\ v_z \end{pmatrix}, \qquad [\lambda] = \begin{pmatrix} \lambda_x & 0 & 0 \\ 0 & \lambda_y & 0 \\ 0 & 0 & \lambda_z \end{pmatrix} \tag{2.2.44}$$

Equation (2.2.41) can be written as following:

$$\rho c\left(\frac{\partial T}{\partial t} + v_x\frac{\partial T}{\partial x} + v_y\frac{\partial T}{\partial y} + v_z\frac{\partial T}{\partial z}\right) - \frac{\partial}{\partial x}\left(\lambda_x\frac{\partial T}{\partial x}\right) - \frac{\partial}{\partial y}\left(\lambda_y\frac{\partial T}{\partial y}\right) - \frac{\partial}{\partial z}\left(\lambda_z\frac{\partial T}{\partial z}\right) = \dot{H} \tag{2.2.45}$$

From here, 3 types of boundary condition are considered.

i). When the temperature is specified as boundary condition over surface S_1

$$T = T^* \tag{2.2.46}$$

ii). When the heat flux is specified as boundary condition over surface S_2

$$\{q\}^t\{n\} = -q^* \tag{2.2.47}$$

Where:

T^* : specified temperature

$\{n\}$: unit outward normal vector

q^* : specified heat flux

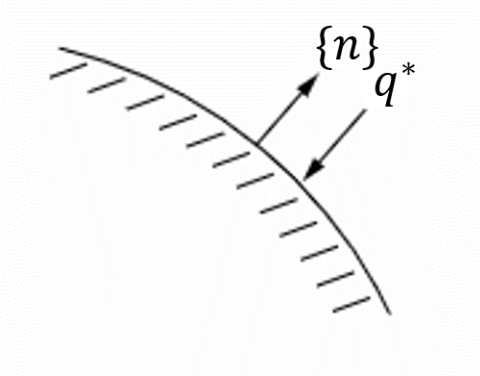

Fig. 2-4 heat flux

iii). When the convection heat transfer is specified as boundary condition surface S_3

$$\{q\}^t\{n\} = h(T_s - T_b) \tag{2.2.48}$$

Where:

h : specified film coefficient

$T_s(=T)$: temperature at the surface S_3

T_a : specified ambient temperature

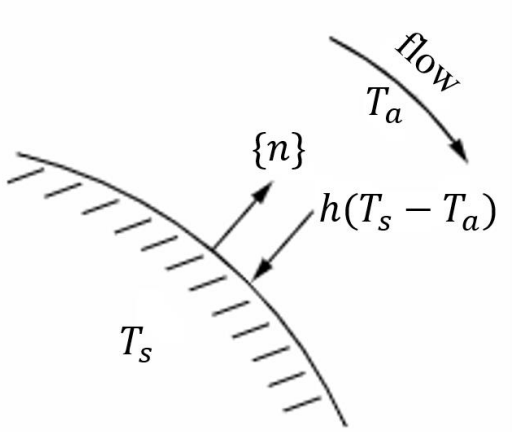

Fig. 2-5 convection heat transfer

Combining equation (2.2.42) with equation (2.2.47) and equation (2.2.48),

$$\{n\}^t[\lambda]\{\nabla\}T = q^* \tag{2.2.49}$$

$$\{n\}^t[\lambda]\{\nabla\}T = h(T_a - T_s) \tag{2.2.50}$$

Pre-multiplying equation (2.2.43) by a virtual temperature change, integrating over the volume of the element, and converting with equation (2.2.49) and equation (2.2.50),

$$\int_V \left\{\rho c\ \delta T\left(\frac{\partial T}{\partial t}+\{v\}^t\{\nabla\}T\right)+\{\nabla\}^t\ \delta T[\lambda]\{\nabla\}T\right\}dV$$
$$=\int_{S_2}(\delta T q^*)dS_2+\int_{S_3}\{\delta T h(T_a-T)\}dS_3+\int_V\left(\delta T\dot{H}\right)dV \quad (2.2.51)$$

Where:

V : volume of element

δT : an allowable virtual temperature

Equation (2.2.51) is the ultimate dominant equation for thermal analysis.

2.2.6. Derivation of Heat flow matrices

Firstly, the temperature is related to the nodal temperature vector by:

$$T=\{N\}^t\{T_e\} \quad (2.2.52)$$

Where:

$T=T(x,y,z,t)$: volume of element

$\{N\}=\{N(x,y,z)\}$: element shape functions

$\{T_e\}=\{T_e(t)\}$: nodal temperature vector of element

Thus, the time derivatives of equation (2.2.52) and δT can be written as:

$$\dot{T}=\frac{\partial T}{\partial t}=\{N\}^t\{\dot{T}_e\} \quad (2.2.53)$$

$$\delta T=\{N\}^t\{\delta T_e\}=\{\delta T_e\}^t\{N\} \quad (2.2.54)$$

The combination of $\{\nabla\}T$ is written as:

$$\{\nabla\}T=\{\nabla\}\{N\}^t\{T_e\}=[B]\{T_e\} \quad (2.2.55)$$

Where:

$$[B]=\{\nabla\}\{N\}^t \quad (2.2.56)$$

With equation (2.2.53) through (2.2.56), equation (2.2.51) can be written as:

$$\int_V \rho c\{\delta T_e\}^t\{N\}\{N\}^t\{\dot{T}_e\}dV+\int_V \rho c\{\delta T_e\}^t\{N\}\{v\}^t[B]\{\dot{T}_e\}dV$$
$$+\int_V \{\delta T_e\}^t[B]^t[\lambda][B]\{\dot{T}_e\}dV=\int_{S_2}\{\delta T_e\}^t\{N\}q^*dS_2$$
$$+\int_{S_3}\{\delta T_e\}^t\{N\}h(T_a-\{N\}^t\{T_e\})dS_3+\int_V\{\delta T_e\}^t\{N\}\dot{H}dV \quad (2.2.57)$$

ρ is constant over the volume of the element, on the other hand, c and $\dot{H}$ will change over the element. Moreover, $\{T_e\}$ and $\{\dot{T}_e\}$ are constant over the element, so they can be out of integral. Finally, equation (2.2.57) is written as:

$$\rho \int_V c\{N\}\{N\}^t dV\{\dot{T}_e\} + \rho \int_V c\{N\}\{v\}^t [B] dV\{T_e\} + \int_V [B]^t[\lambda][B] dV\{T_e\} = \int_{S_2} \{N\} q^* dS_2 + \int_{S_3} hT_a\{N\} dS_3 - \int_{S_3} h\{N\}\{N\}^t dS_3\{T_e\} + \int_V \dot{H}\{N\} dV \quad (2.2.58)$$

To simplify this:

$$[C_t]\{\dot{T}_e\} + ([K_{tm}] + [K_{tb}] + [K_{tc}])\{T_e\} = \{Q_f\} + \{Q_c\} + \{Q_g\} \quad (2.2.59)$$

Where typical terms are followings:

$[C_t] = \rho \int_V c\{N\}\{N\}^t dV$: element specific heat matrix

$[K_{tm}] = \rho \int_V c\{N\}\{v\}^t [B] dV$: element mass transport conductivity matrix

$[K_{tb}] = \int_V [B]^t[\lambda][B] dV$: element diffusion conductivity matrix

$[K_{tc}] = \int_{S_3} h\{N\}\{N\}^t dS_3$: element convection surface conductivity matrix

$\{Q_f\} = \int_{S_2} \{N\} q^* dS_2$: element mass flux vector

$\{Q_c\} = \int_{S_3} hT_a\{N\} dS_3$: element convection surface heat flow vector

$\{Q_g\} = \int_V \dot{H}\{N\} dV$: heat generation rate vector for causes other than Joule heating

2.2.7. Derivation of damping matrices structural mass matrix

In this simulation, transient analyze has be chosen for more accurate result rather than static analyze. The transient analyze should consider damping effect. The damping matrices $[C]$ and $[C_{tu}]$ in equation (2.2.1) and (2.2.2) can be calculated by following equations.

$$[C] = \alpha'[M] + \beta'[K] + \frac{f}{2\pi\Omega}[K] \quad (2.2.60)$$

α' : mass matrix multiplier (input by operator)
$[M]$: structural mass matrix
β' : stiffness matrix multiplier (input by operator)
$[K]$: structural stiffness matrix
f : constant structural damping coefficient (input by operator)
Ω : frequency for the calculation of equivalent viscous damping

$$[C_{tu}] = -T_0[K_{ut}] \quad (2.2.61)$$

$[K_{ut}] = -\int_V [B]^t[D]\{\alpha\}[N]^t dV$: element thermoelastic stiffness matrix

$T_0 = T_{ref} + T_{off}$: absolute reference temperature

T_{off} : offset temperature from absolute zero to zero

2.3. Roundness error evaluation methods

To evaluate the roundness of the cross section of deformed liner, generally there are 4 methods, which is Minimum Zone Circle (MZC), Least Squares Circle (LSC), Maximum Inscribed Circle (MIC) and Minimum Circumscribed Circle (MCC). The difference in the accuracy between these methods are small according to previous study,[14][15] so LSC method has been used in this investigation.

2.3.1. LSC method

Fig.2-6 shows the simple mechanism of LSM method. Firstly, certain center of the circle is set so that the sum of squares of the deviation for measured profile is minimized. Next, while this center is as the center coordinate of the measured profile, the inscribed circle and circumscribed circle is drawn. The roundness error ΔR is the difference between the radial of the inscribed circle $R_{\min}$ and the radial of the circumscribed circle $R_{\max}$.

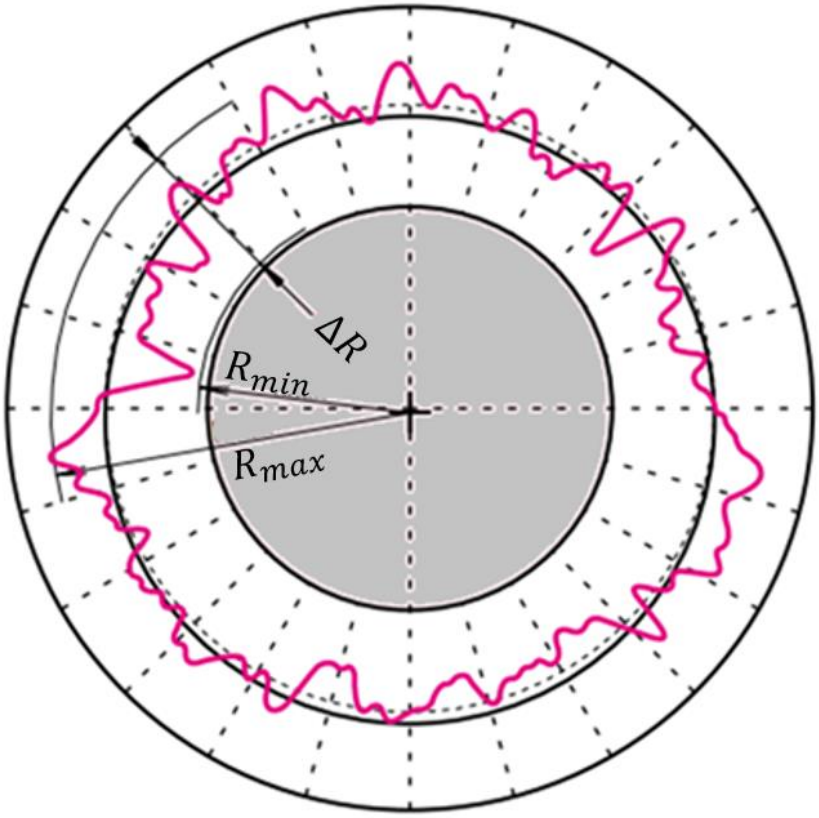

Fig.2-6. LSC method

2.3.2. Calculation method

When the center coordinate of the measured profile is expressed as (a, b), the radial of each plot for the measured profile can be expressed as following:

$$R = \sqrt{(x_i - a)^2 + (y_i - b)^2} \tag{2.3.1}$$

Thus, the squared average of this radial is:

$$E = \bar{R}^2 = \frac{1}{n}\sum_{i=1}^{n}\{(x_i - a)^2 + (y_i - b)^2\} \tag{2.3.2}$$

a, b is determined so that R is minimized, so the partial differential of E with respect to a and b should be zero.

$$\begin{cases} \dfrac{\partial E}{\partial a} = \dfrac{1}{n}\displaystyle\sum_{i=1}^{n}\{2(x_i - a)\cdot(-1)\} = \dfrac{2}{n}\sum_{i=1}^{n}(a - x_i) = 0 \\ \dfrac{\partial E}{\partial b} = \dfrac{1}{n}\displaystyle\sum_{i=1}^{n}\{2(y_i - b)\cdot(-1)\} = \dfrac{2}{n}\sum_{i=1}^{n}(b - y_i) = 0 \end{cases} \tag{2.3.3}$$

$$\Downarrow$$

$$\begin{cases} a = \dfrac{1}{n}\displaystyle\sum_{i=1}^{n} x_i \\ b = \dfrac{1}{n}\displaystyle\sum_{i=1}^{n} y_i \end{cases} \tag{2.3.4}$$

Based on these a and b, $R_{\max}$ and $R_{\min}$ can be determined easily using python code. Then the roundness error can be expressed as following:

$$\Delta R = R_{\max} - R_{\min} \tag{2.3.5}$$

Chapter 3. Validating simulation model

3.1. The physical engine 3D model

The physical engine model is based on NISSAN CA18 engine which is used by Hitosugi H to investigate liner deformation experimentally.[7] This is a water-cooled, 4-stroke, in line 4-cylinder gasoline engine, with total displacement of 1809cc and bore × stroke = 83mm × 83.6mm.[7] The cylinder block is made of gray cast iron and the head is made of aluminum alloy. The liner has dry liner structure, 80μm clearance toward cylinder inner wall and made of 1.6mm thickness gray cast iron.[7] The physical 3D model is shown below Fig.3-1 and same model without head for visualization of the other components structure. This assemble model consist of seven components, which are four bolts, liner, cylinder block and head. This model is focused on just only 1st and half of 2nd cylinder, because 1st or 4th cylinder liner deformation would be larger more unsymmetric than 2nd or 3rd cylinder liner deformation due to the unsymmetric thermal load as shown Fig.3-3. Especially, the deformation or distortion of the Siamese (Rear) side could be crucial because of no water jacket path.

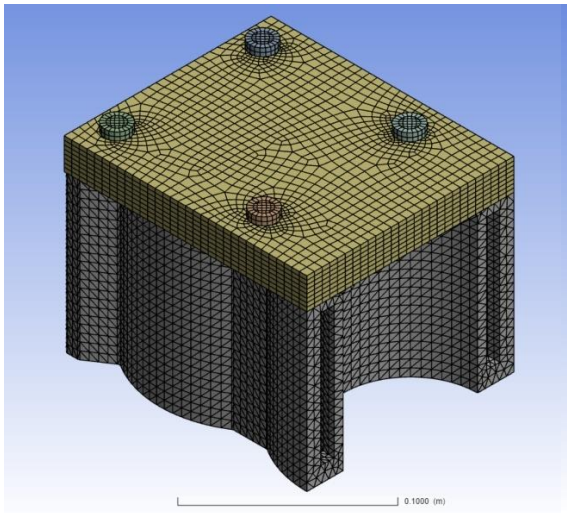

Fig.3-1 physical model with head

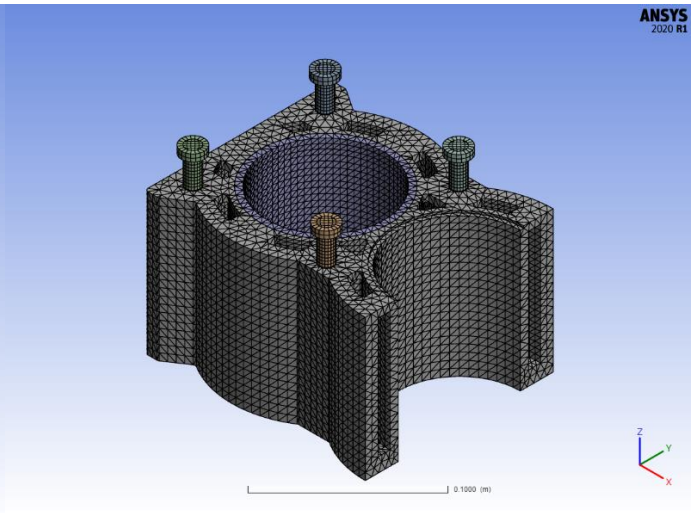

Fig.3-2 physical model without head

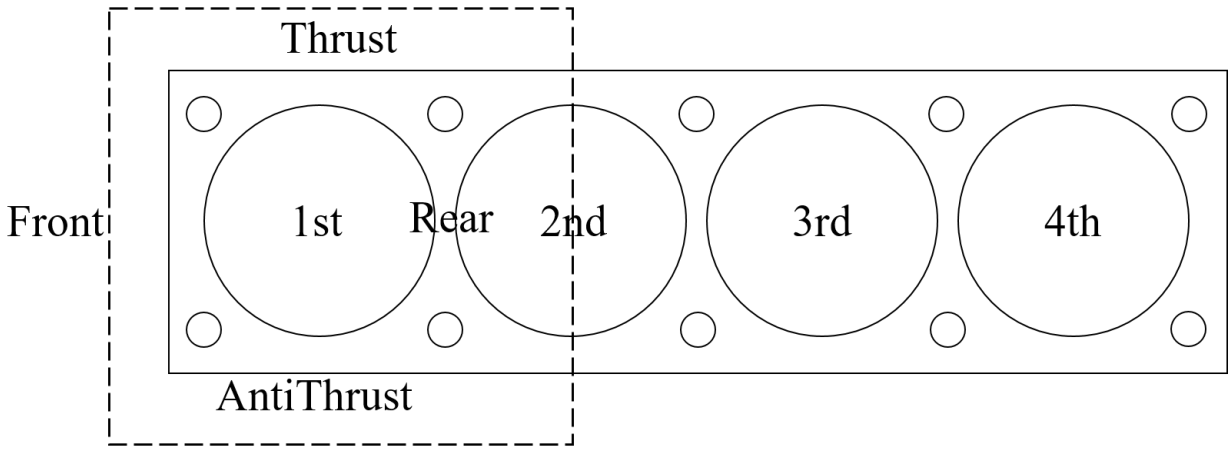

Fig.3-3 physical model focusing on only 1st and half of 2nd Cylinder

3.2. Adoptive meshing

Meshing is very important to get accurate result for FEM. This means high density mesh is better for simulation but that also takes more computation time. Thus, the adoptive meshing, not too fine or too rough, is required. Fig.3-4 shows the computation time to solve it and the average difference from 1 million nodes mesh result while the meshing is changed variously. From this result, the 246274 nodes and 130575 elements can be judged as adoptive mesh for this model. Moreover, as shown in Fig.3-1, mesh density is higher especially in the contact region between the components like head and bolts. This is general and efficient approach to produce adoptive mesh. With this approach, saving the number of nodes and computation time while keeping accuracy. This research needs many times of calculation, so computation time should be as less as possible. Furthermore, these all calculations are calculated in the cluster computer, which is chosen to use 8 processor parallelly.

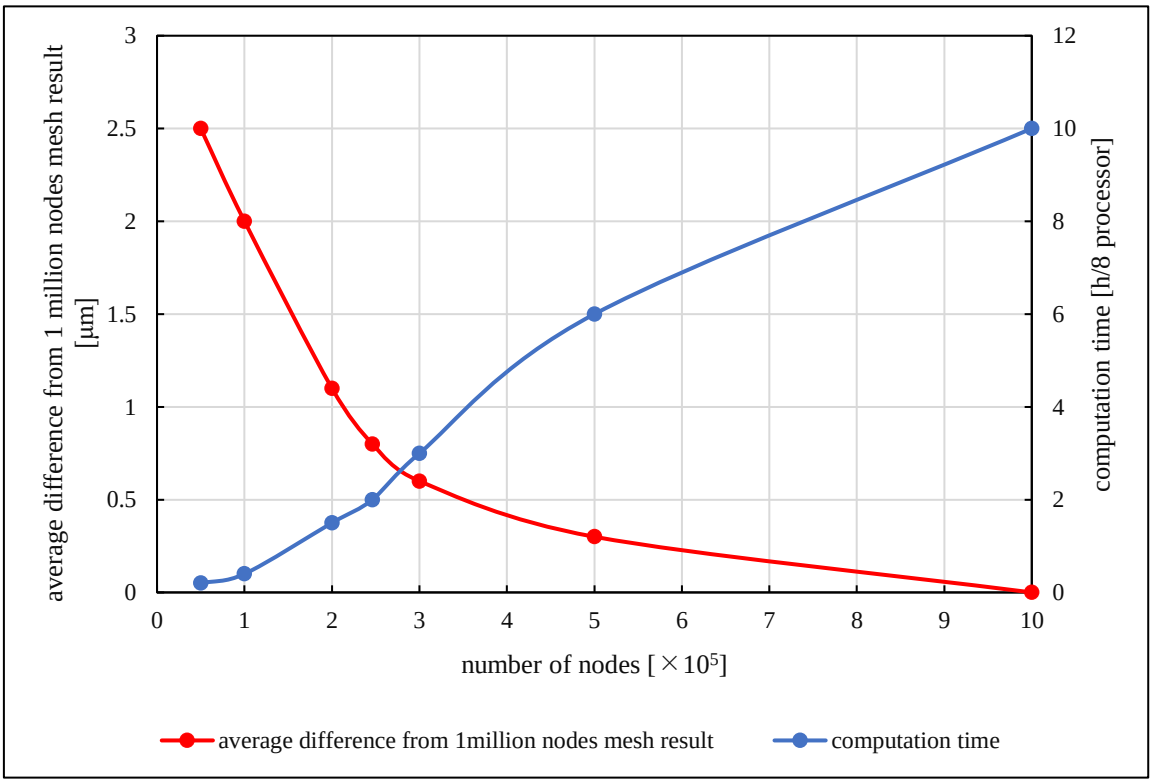

Fig.3-4 adoptive meshing test

3.3. Structural boundary condition

3.3.1. Contact definition between components

In the ANSYS MECHANICAL, five types of contact definition can be selected, which is bonded, frictional, frictionless, rough and no separation. Generally, frictional is set for almost every contact region definition. There are three exceptions of this. Firstly, the contacts between head and cylinder block top face, head and liner top face are set as bonded because of the gasket. In the test engine, there is the gasket between them to seal the combustion area, so bonded is the

best for this contact definition in this simulation model. Secondly, the contact between the liner and the cylinder block is set as frictionless because there is 80μm clearance between them in the test engine. Finally, the contacts between 4 bolts and cylinder block are set as bonded while the contacts region about the other bolts face and other components are frictional. Fig.3-5 shows the comparison with the bolt used in the test engine and the bolt used in the physical model. (a) in Fig.3-5 is the semi-thread M10 bolt picture generally used in the engine and (b) in the Fig.3-5 is the physical model of the bolt and (c) shows the contact definition for each contact regions. According to Montgomery J [15] the thread of the bolt physical model does not need to get accurate result in the general FEM. Instead of that, the contact definition for thread region should be set as bonded like (c) in Fig.3-5 because that face is fixed due to the threads.

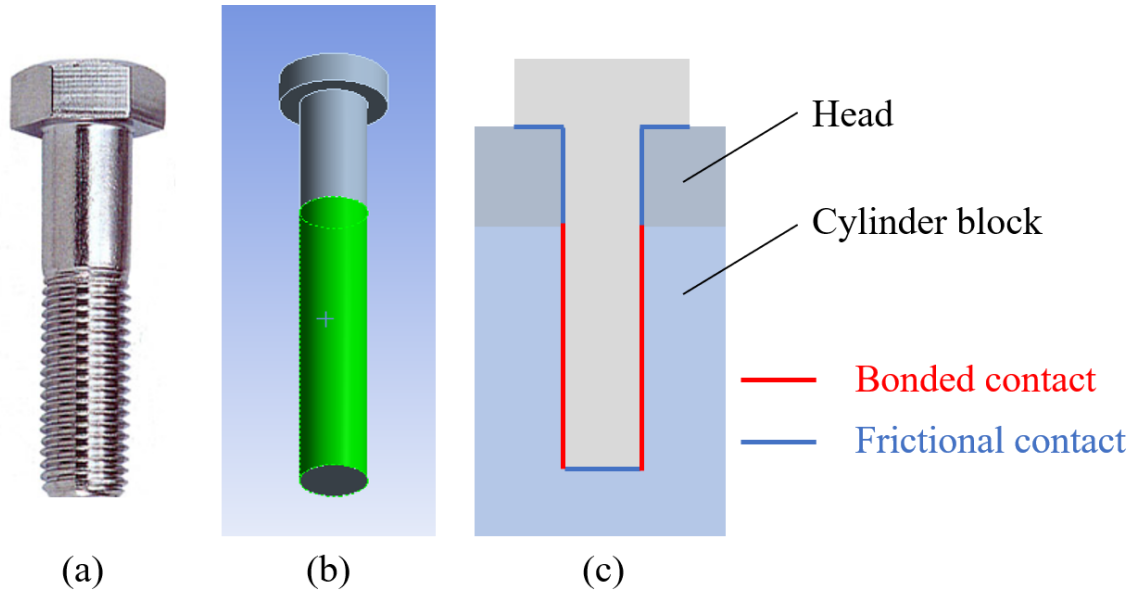

Fig.3-5 physical model of the bolt

3.3.2. Bolt pretension load

The bolts pretension load caused by assembling and tightening the bolts is applied in this simulation model for more accurate structural load and results. This pretension load is preload boundary condition so this load is applied in the first physical time step in this transient analysis. The applied value of the pretension load is calculated by hand based on the following general equation

$$T = kdF \tag{3.1}$$

Where:

T : bolt tightening torque [N · m]
F : bolt pretension load [N]
d : bolt diameter [m]
k : torque coefficient [−]

Generally, the torque coefficient is 0.2 and the bolt diameter is 0.01m. according to JIS bolt

tightening standards,[17] the tightening torque is $44\,\mathrm{N}\cdot\mathrm{m}$. Based on equation (3.1), the bolt pretension load is calculated following:

$$F = \frac{T}{kd} = \frac{44}{0.2 \times 0.01} = 22000[N] \tag{3.2}$$

This value is applied for each 4 bolts pretension load as boundary condition.

3.4. Thermal boundary condition

In this simulation model, the liner deformation is calculated by structural and simple thermal load without combustion phenomenon, because this simulation model is based on the experimental data under 4000rpm full load condition conducted by Hitosugi H et al and that investigation data shows just temperature data and deformation data without detail combustion information.[7] Due to this no reference data about combustion, this simulation model is calculated by only structural and thermal load. However, this has the benefits which are saving computation time and simplifying simulation model. Moreover, the next chapter 4 indicates that this simulation without combustion phenomenon is enough accurate to evaluate the roundness error of the liner, which is the most important value for this investigation.

3.4.1. Temperature condition

In this simulation model, the temperature of the liner inner wall and 2nd cylinder inner wall is fixed as boundary condition based on the experimental data by Hitosugi H et al.[7] Moreover, the temperature of the liner and cylinder block is considered to be distributed along the depth, so the physical model of the liner and cylinder block is divided into 5 parts along the depth direction, which are top-10mm, 10mm-50mm, 50mm-80mm, 80mm-90mm, 90mm-bottom, and applied different temperature in each depth area. Fig.3-6 and Fig.3-7 show the applied temperature distribution of them as boundary condition for each depth area and it is shown that the temperature is applied simply so that the deeper the depth from the top deck is, the lower the average temperature is. The temperature from 90mm depth to the bottom of them is not applied as boundary condition, because the piston-stroke of this engine model is 83.6mm.

The initial temperature and reference temperature must be applied as boundary condition for this calculation, because the thermal strain is calculated based on this value (written in chapter 2). These temperatures generally must be same and set to be 22℃ as default, but these are set 85℃ in this simulation model. This is because exclude the extra liner deformation from this calculation. The engine components near the combustion area are manufactured considered to be deformed by thermal load. For example, the top face diameter of the piston head is smaller than the bottom face diameter of that in the room temperature so that the piston head shape is proper cylinder in combustion temperature. This structure is built considering that the top face diameter of that would be expand bigger than the bottom face diameter of that, because the top of that has higher temperature than the bottom of that. Considering this example and similar structure of other engine

components, the liner deformation measured after the engine is run for a whole and get warmed. This is why, the extra deformation must be excluded and reference and initial temperatures are set to 85℃.

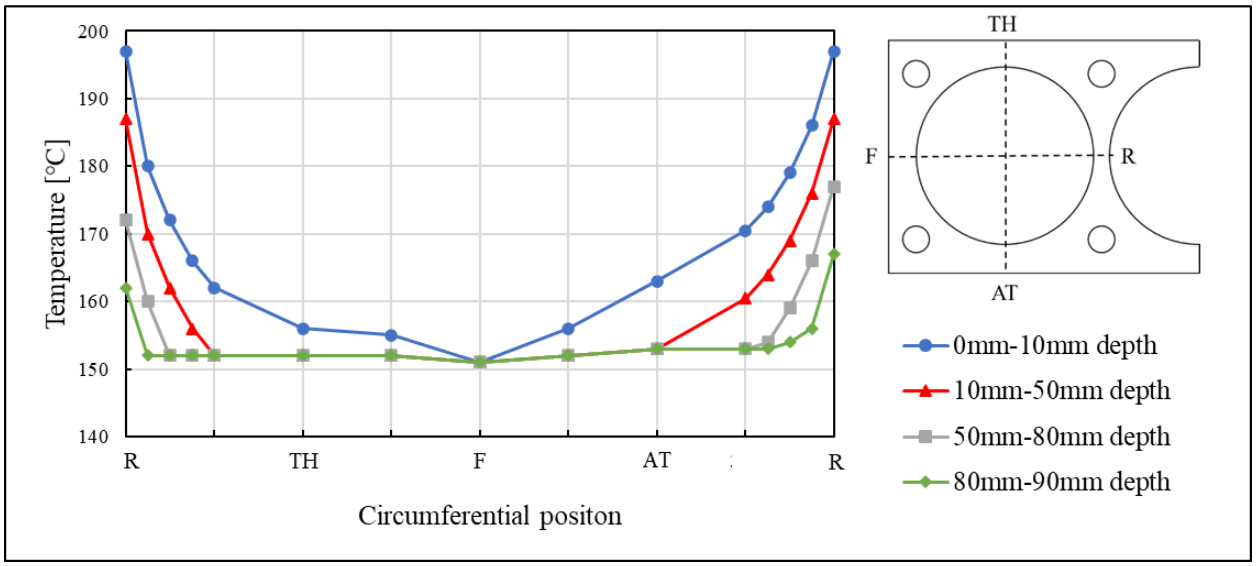

Fig.3-6 applied liner inner wall temperature as boundary condition

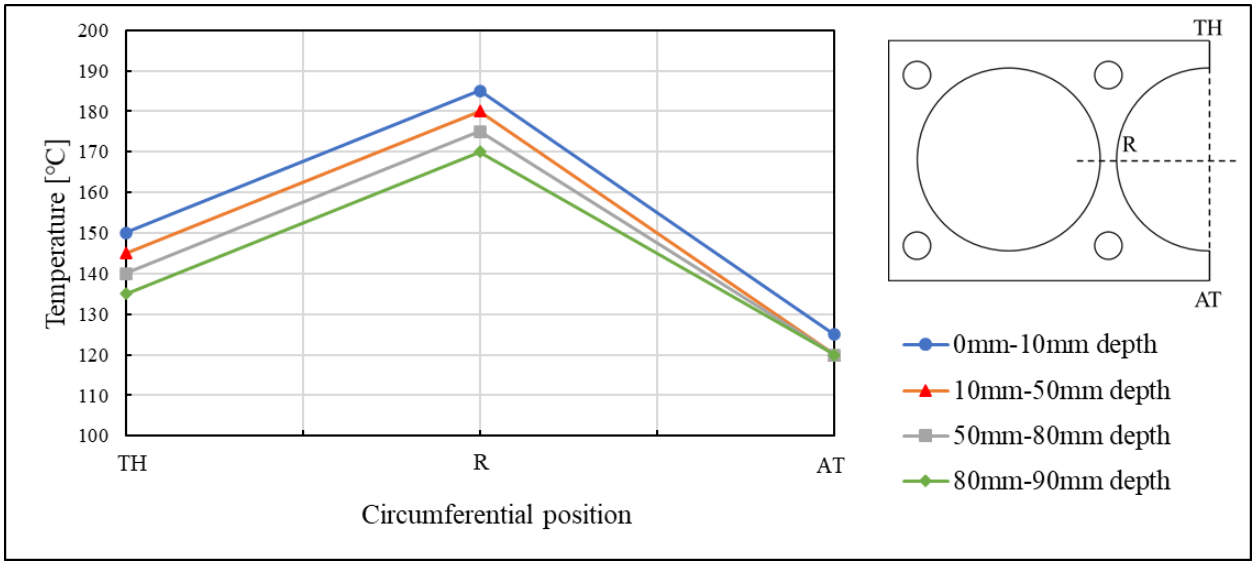

Fig.3-7 applied 2nd cylinder inner wall temperature as boundary condition

3.4.2. Convection heat transfer condition

Fig.3-8 shows the cooling water path in the physical 3Dmodel of the engine. In this simulation, the convection heat transfer coefficient and ambient (cooling water) temperature must be specified for the water jacket path wall as boundary condition. Generally, the cooling water temperature is around 80℃~90℃, so 85℃ is set as boundary condition. Karamangil MI et al [18] investigated the parameter of cylinder and jacket side convective heat transfer coefficients using very similar gasoline engine to the test engine of Hitosugi H et al.[7] Fig.3-9 is a part of results estimated by Karamangil MI et al.[18] Fig.3-9 shows the convection heat transfer coefficient

between cylinder block jacket path wall and cooling water under 4000rpm full load condition is estimated to around 7500W/m^{2}K, so the coefficient is set to 7500W/m^{2}K against all the surface of jacket path.

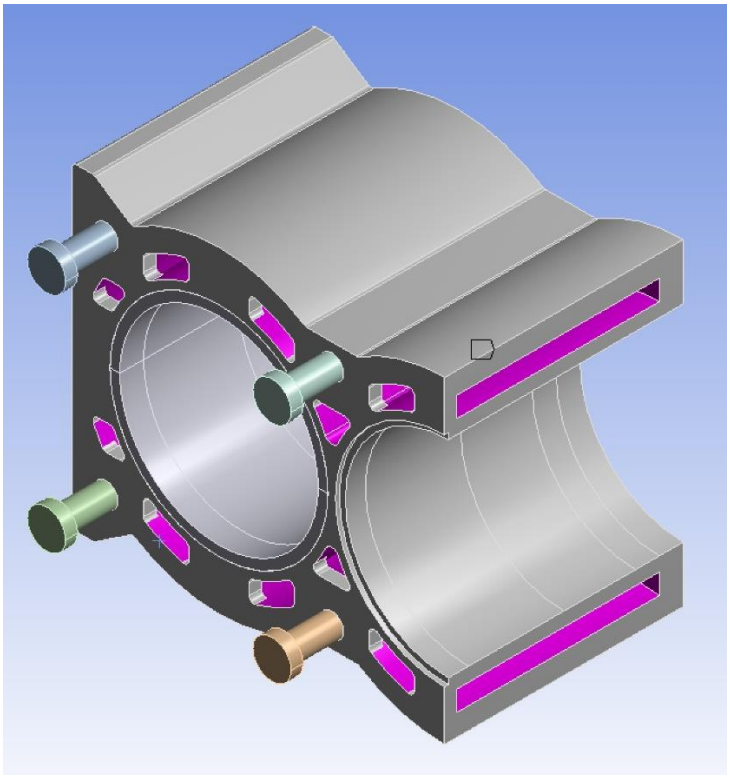

Fig.3-8 cooling water jacket path

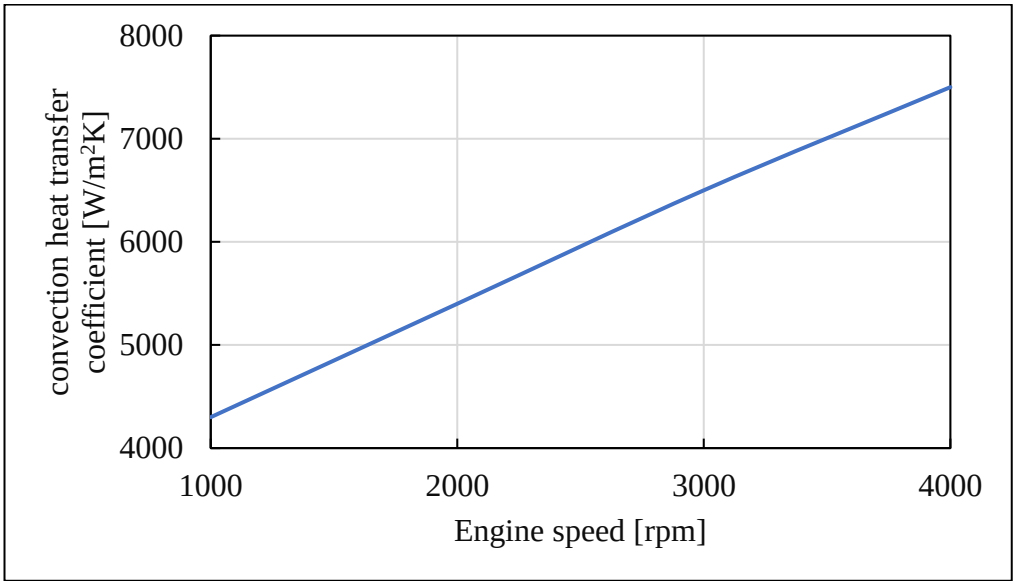

Fig.3-9 convection heat transfer coefficient in various engine speed

Chapter 4. Validation result

4.1. Bolt stress by pretension load

Fig.4-1 shows the simulation result of stress and strain caused by only bolt pretension load. This result is just after first physical time step of transient analysis, when only the bolt pretension load is applied to simulate assembling load. This result is very similar to the bolt pretension load simulation result conducted by J Montgomery,[16] so the bolt pretension load can be judged to be validated sufficiently.

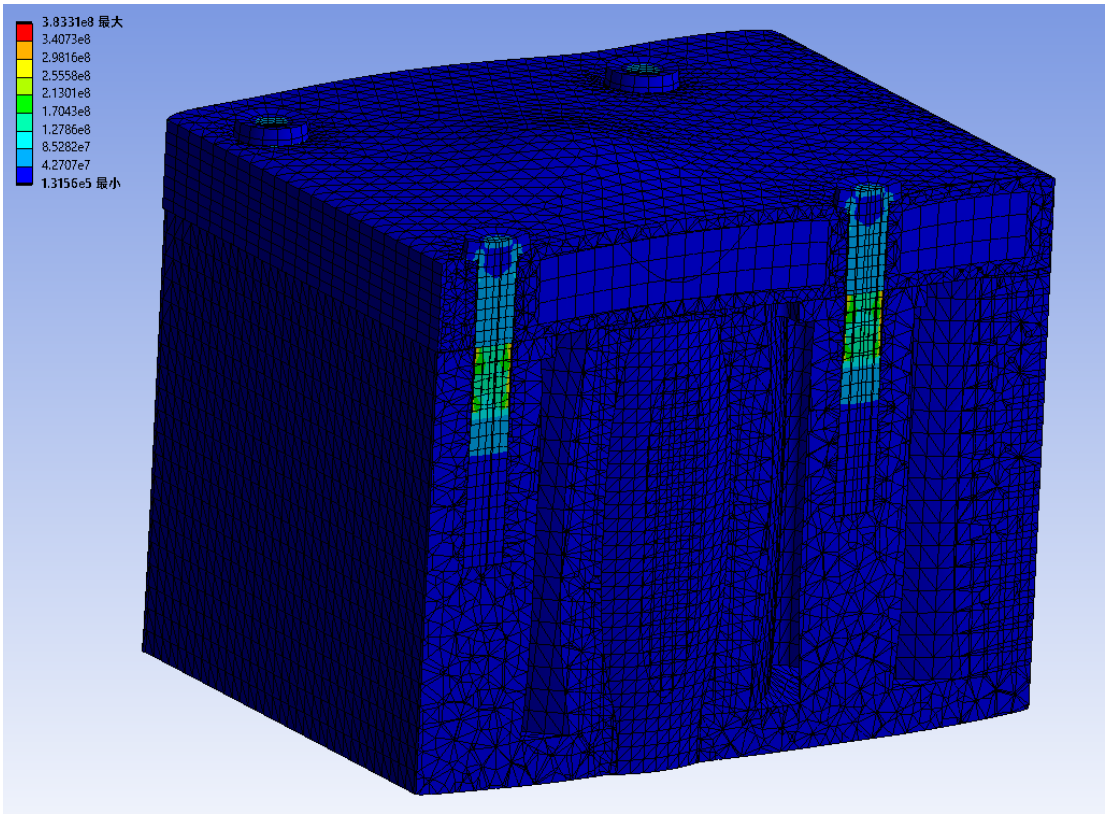

Fig.4-1 the equivalent stress caused by bolt pretension load

4.2. Temperature distribution

Fig.4-2 shows comparison result between the temperature distribution of simulation and that of experiment conducted by Hitosugi H et al. [7] These temperatures are all at the 10mm depth from the top deck. Both comparison result of the liner temperature and cylinder block temperature are very similar. Moreover, Fig4-3 shows the 3D simulation temperature distribution of all physical model of the liner and cylinder block. The temperature in Siamese side of both of the liner and cylinder block are higher than other sides because of no cooling water jacket path. Thus, this temperature boundary condition can be judged to be validated sufficiently.

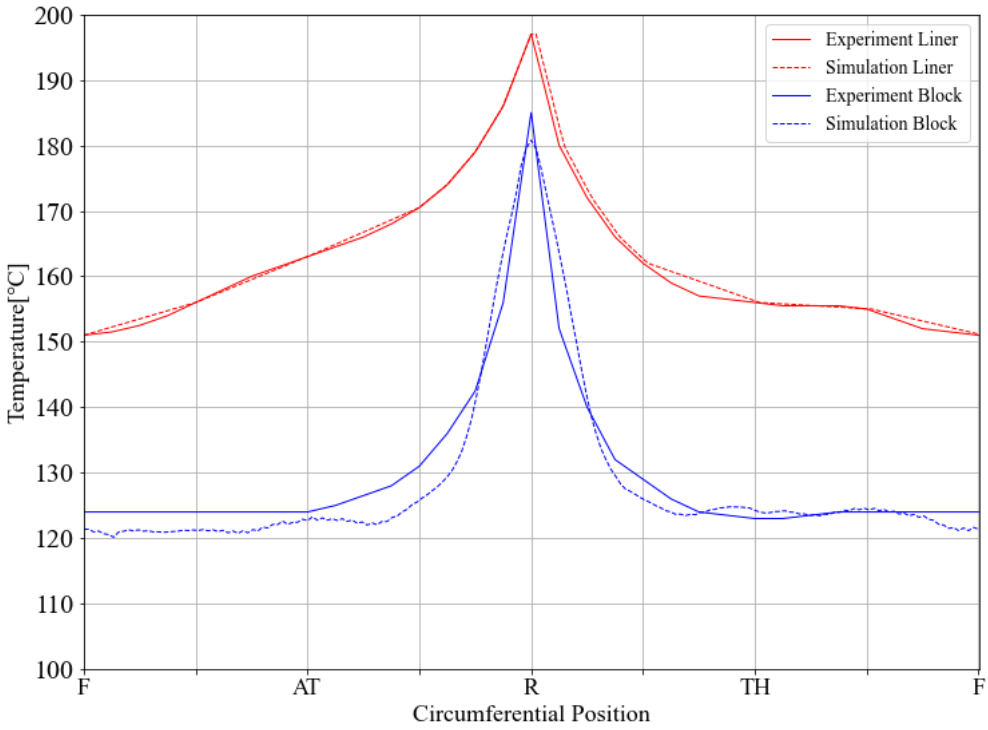

Fig.4-2 comparison between simulation temperature and experimental temperature

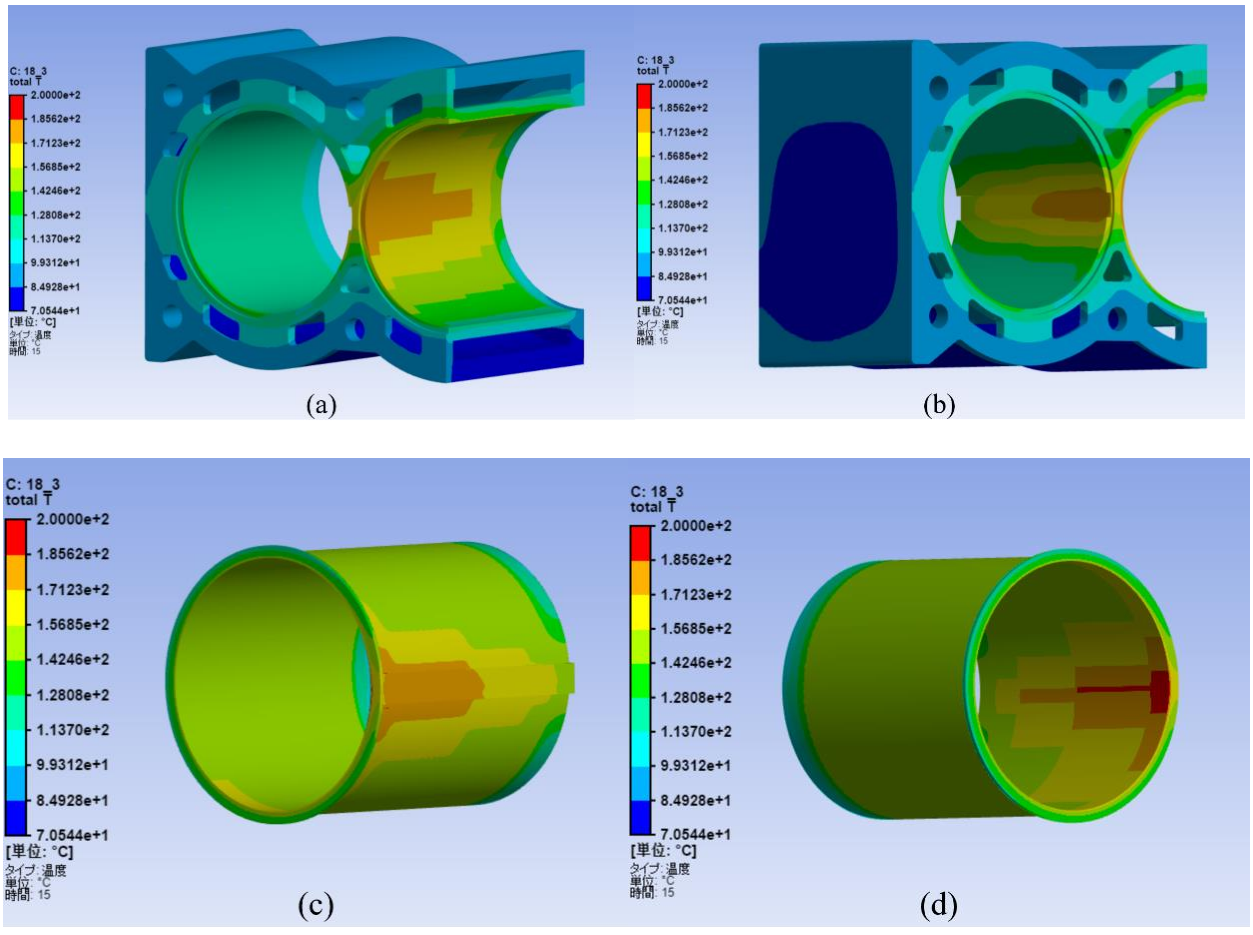

Fig.4-3 temperature distribution of liner and cylinder block by simulation

4.3. Bore deformation of Cylinder Liner

Fig.4-4 shows the comparison result between experimental liner deformation and simulation liner deformation on both of 10mm depth from top deck and 90mm depth from top deck. Generally, this kind of validation such as deformations, it is important to fit both of the values like roundness error and the deformation trend. As shown in Fig.4-4, the deformed bore of simulation and that of experiment have almost same deformation trend, and the value of average difference between simulation bore and experimental bore $\overline{\Delta r}$ calculated based on equation (4.1) is less than 7μm. This is enough to evaluate roundness error of deformed liner bore. The accuracy of roundness error is calculated based on equation (4.2). That accuracy is around ±15%. Fig.4-5 shows the 500 times scale total deformation of the liner and cylinder block to see the deformation trend of them easily.

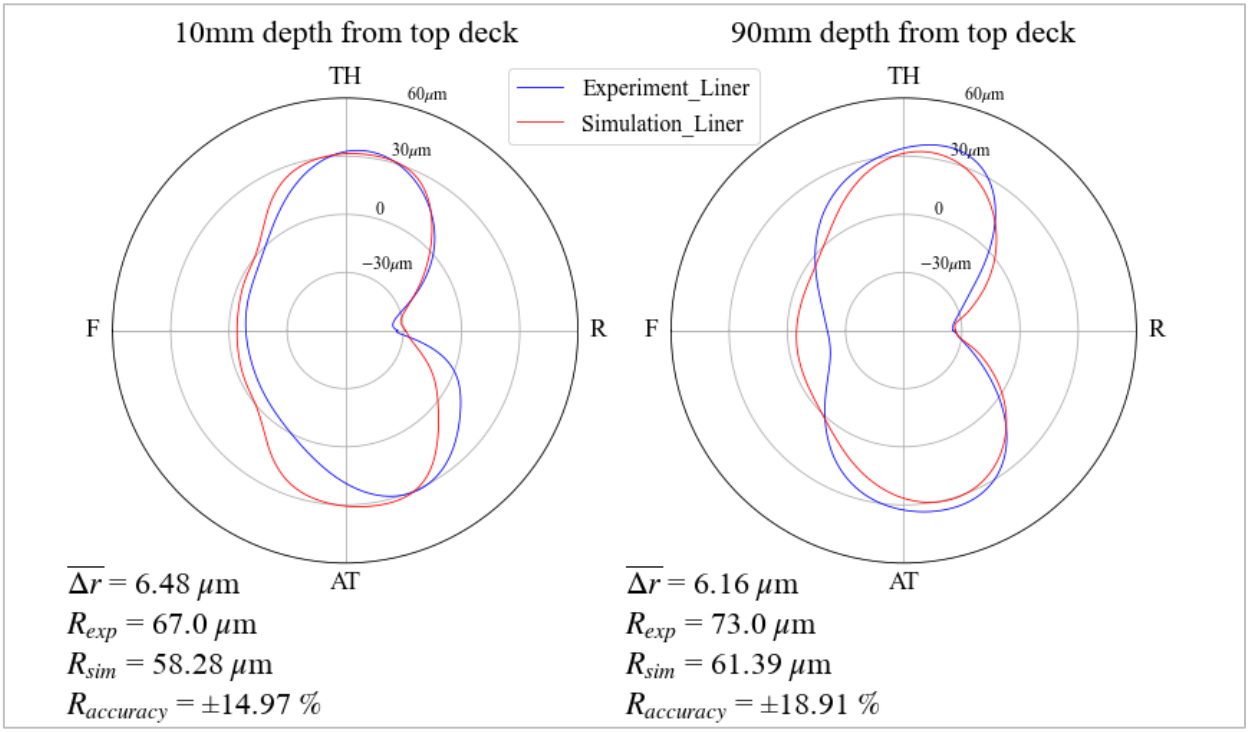

Fig.4-4 comparison between liner deformations of simulation and that of experiment

$$\overline{\Delta r} = \frac{1}{n}\sum_{i=1}^{n}\left(r_{exp,i} - r_{sim,i}\right) \tag{4.1}$$

$$R_{accuracy} = \frac{|R_{sim} - R_{exp}|}{R_{sim}} \times 100 \tag{4.2}$$

$\overline{\Delta r}$: average difference between simulation bore and experimental bore [μm]

$r_{exp,i}$: radius of deformed liner in the experiment [μm]

$r_{sim,i}$: radius of deformed liner in the simulation [μm]

$R_{accuracy}$: error range (accuracy) of roundness error [%]

R_{exp} : roundness error of deformed liner in the experiment [μm]

R_{sim} : roundness error of deformed liner in the simulation [μm]

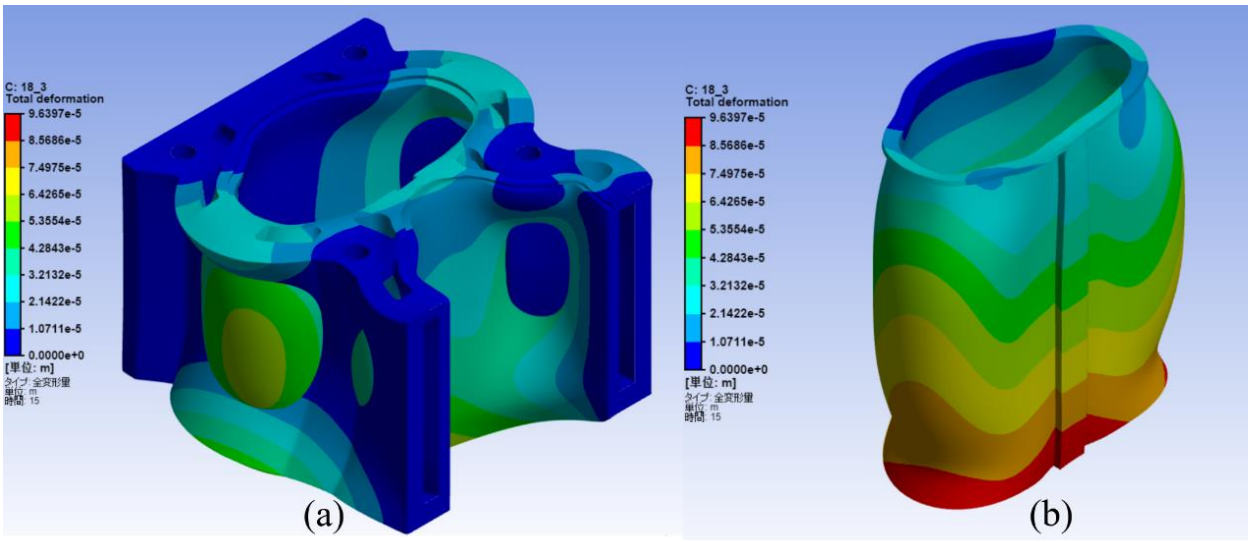

Fig.4-5 total deformation of the cylinder and liner (deformation scale × 500)

4.4. Physical time of transient analysis

Fig.4-6, 4-7, 4-8, 4-9 show the convergence of temperature distribution and deformation for the liner and cylinder block in physical time. In these figures, green plot, blue plot and red plot express the maximum value, average value and minimum value in the 3D-physical model respectively. From these convergence results, every temperature and deformation is converged until 15 second. This means that 15 second is quite enough for the physical time in this transient analysis model. So physical time is set to 15 seconds for this simulation model.

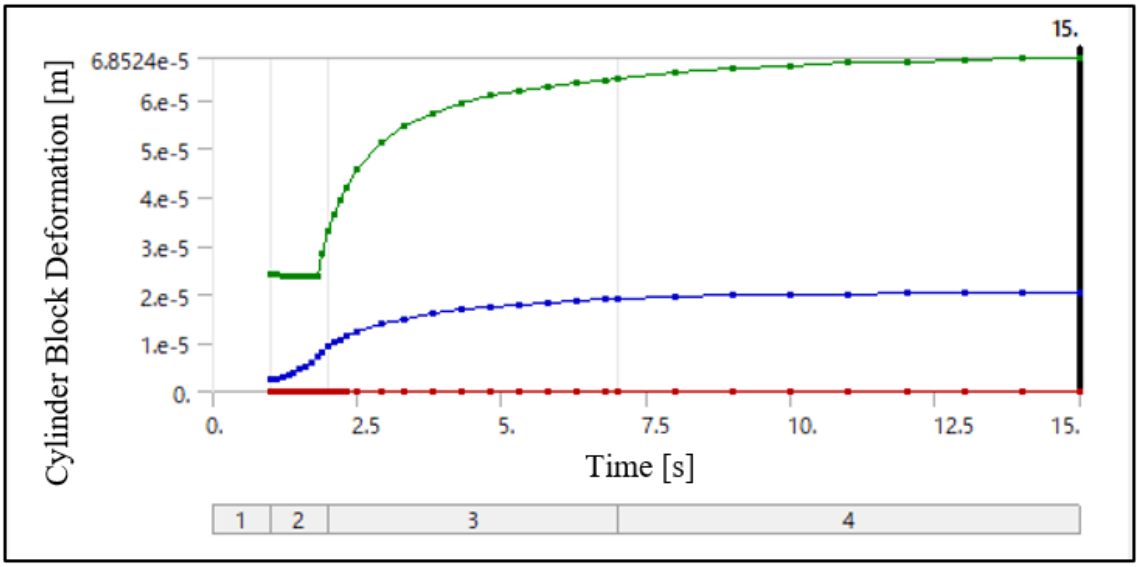

Fig.4-6 convergence of cylinder block deformation

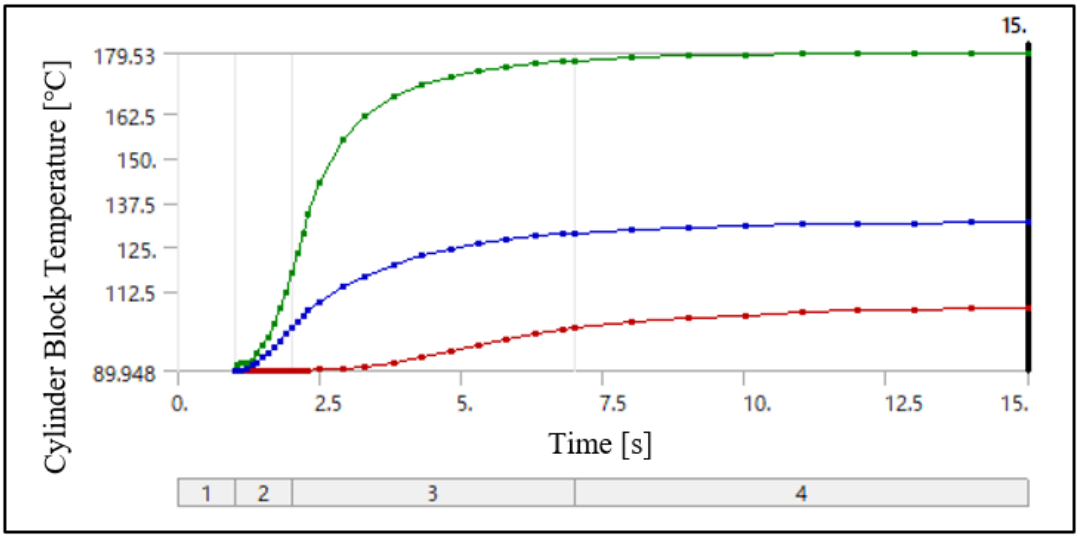

Fig.4-7 convergence of cylinder block temperature

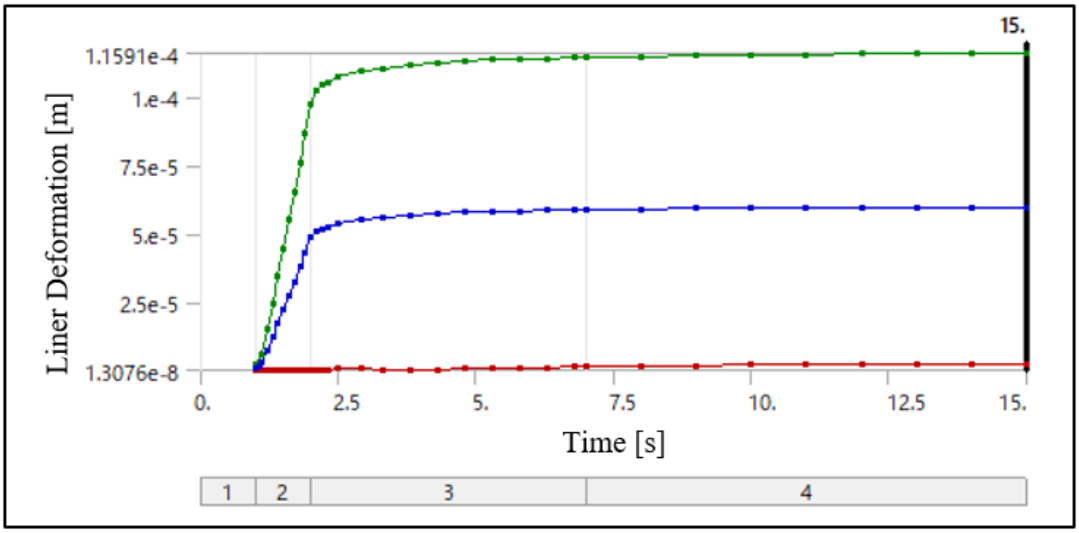

Fig.4-8 convergence of liner deformation

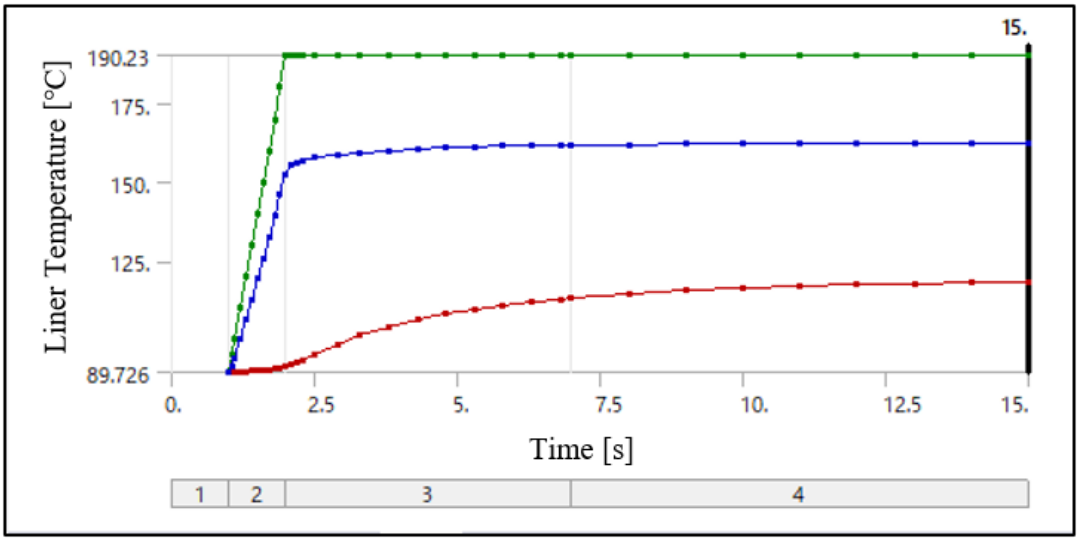

Fig.4-9 convergence of liner temperature

Chapter 5. The bore deformation result while changing material property and temperature

5.1. The effect on liner bore deformation while changing material property

Based on the physical theory, the potential material properties to affect the bore deformation of the liner are thermal expansion coefficient (TEC), thermal conductivity, Young's modulus and Poison's ratio. In this section, it is indicated that the most affectable parameter among these 4 material properties, which is investigated by this simulation model.

In order to investigate the most affectable material property on this bore deformation of the liner and roundness of that, the bore deformations are simulated while only each a parameter of TEC, thermal conductivity, Young's modulus, Poisson's ratio are changed by small value, and the other parameters are kept same. The gray cast iron is applied for the liner material in this validated simulation model, so basically these operated material properties are operated in the range which is possible to achieve that property with recent metal materials or alloy materials.

Fig.5-1 through Fig.5-5 shows the roundness error and average displacement amount of bore radius in each 10mm, 50mm, 80mm, 90mm depth of the liner while changing only the TEC, thermal conductivity, Young's modulus, Poisson's ratio of the liner material properties. The average displacement amount of bore radius is calculated by equation (5.1).

$$\overline{\Delta r} = \frac{1}{n}\sum_{i=1}^{n} \Delta r_i \tag{5.1}$$

Where:

$\overline{\Delta r}$: average displacement amount of bore radius

n : number or plots

Δr_i : displacement amount of bore radius in arbitrary plot i

It is possible to judge the overall deformation is expanding or shrinking with this value. As these results, TEC is the most affectable material property on the bore deformation. Overall, the higher the TEC is, the higher the roundness error of the liner are with a small maximum value around zero. The cause of this maximum value is seemed to be transition of the whole deformation from expansion to shrinkage due to the negative TEC. On the other hand, there is the minimum value of roundness error between the range of zero and 5 [10^6/°C]. This could be the key to reduce the roundness error of cylinder liner bore in the engine operation. Moreover, Young's modulus and Poisson's ratio don't affect on the bore deformation of the liner, and the higher a little the thermal conductivity is, the higher both of the roundness error and average displacement amount of bore radius of the liner are.

Fig.5-6 through Fig.5-9 shows the roundness error and average displacement amount of bore radius in each 10mm, 50mm, 80mm, 90mm depth of the liner while changing only the TEC,

thermal conductivity, Young's modulus, Poisson's ratio of the cylinder block material properties. The result is almost same as those result of the liner, but there is no maximum value when the TEC is changing. Furthermore, it is indicated that the influence on the bore deformation by changing TEC of the liner is bigger than that of the cylinder block.

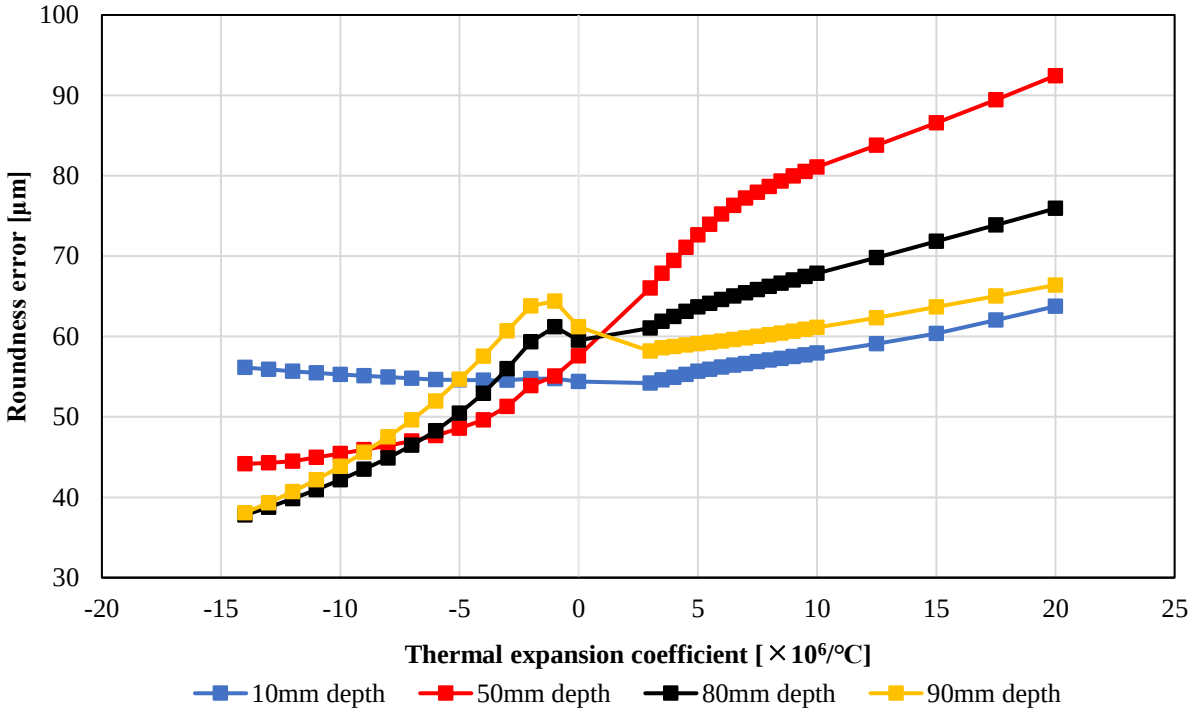

Fig.5-1 Roundness error while changing TEC of the liner

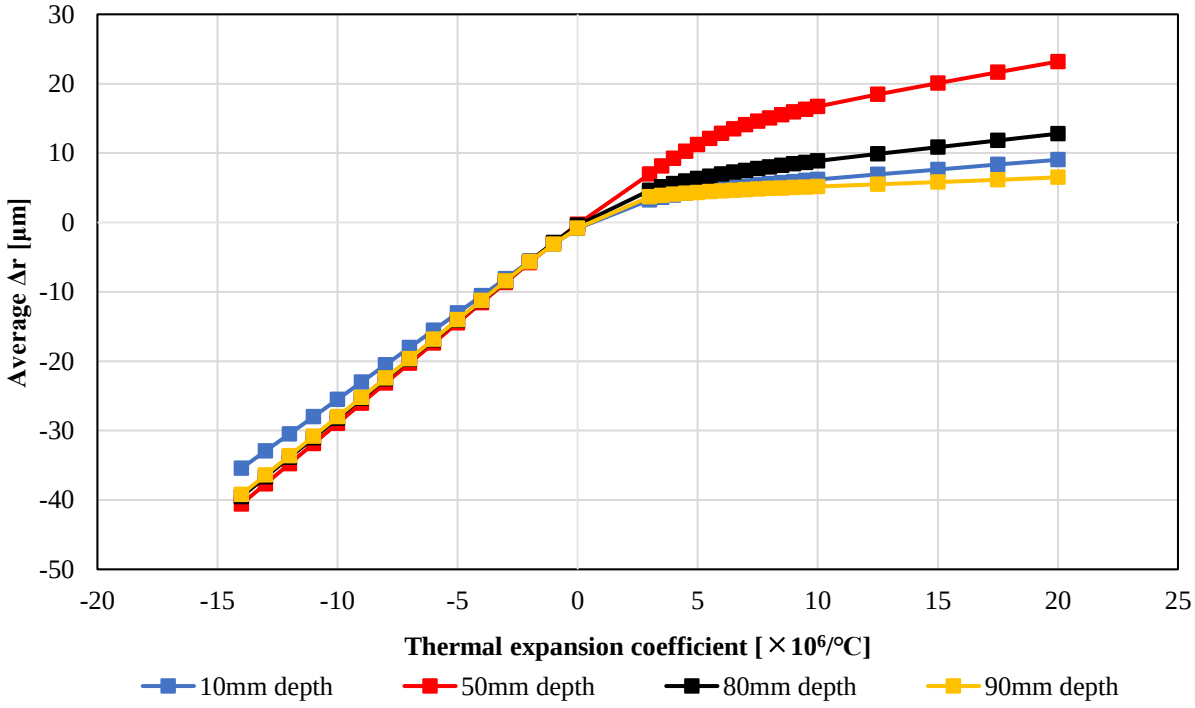

Fig.5-2 Average delta radius while changing TEC of the liner

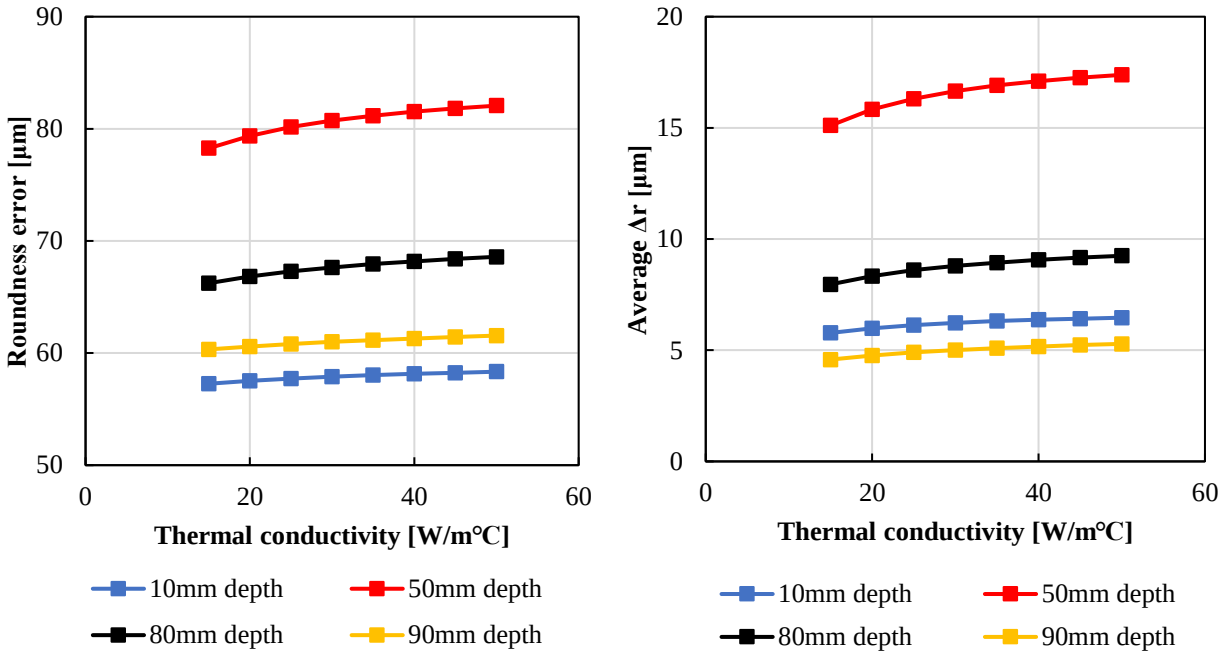

Fig.5-3 Roundness error and average delta radius
while changing thermal conductivity of the liner

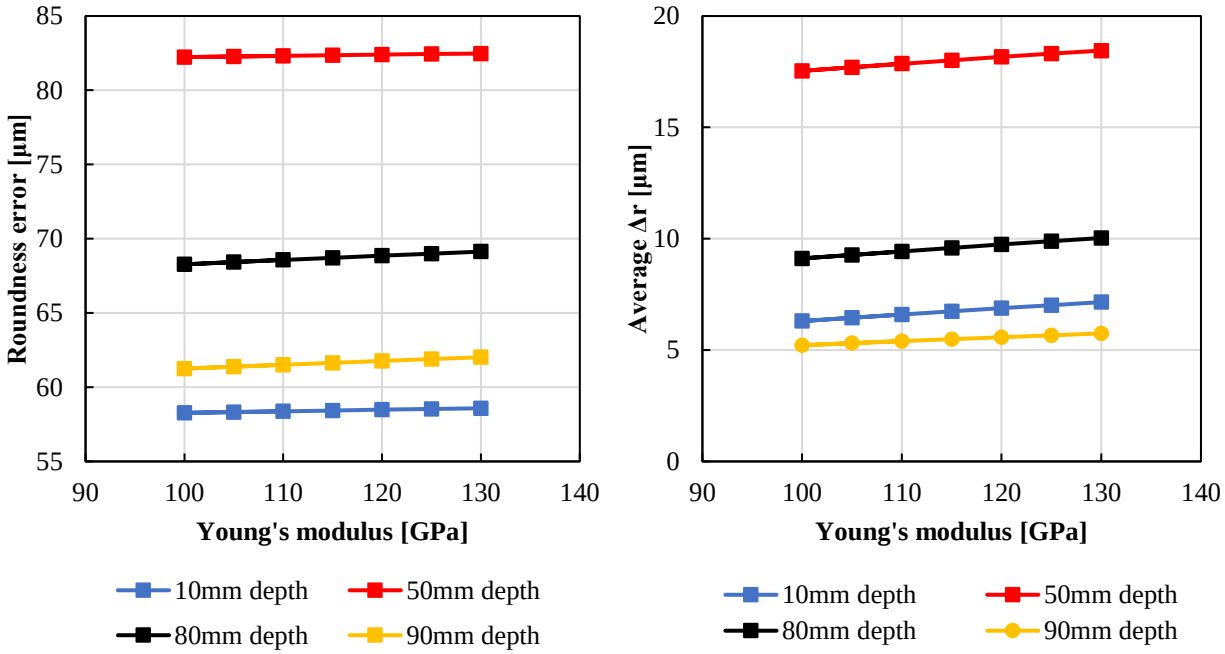

Fig.5-4 Roundness error and average delta radius
while changing Young's modulus of the liner

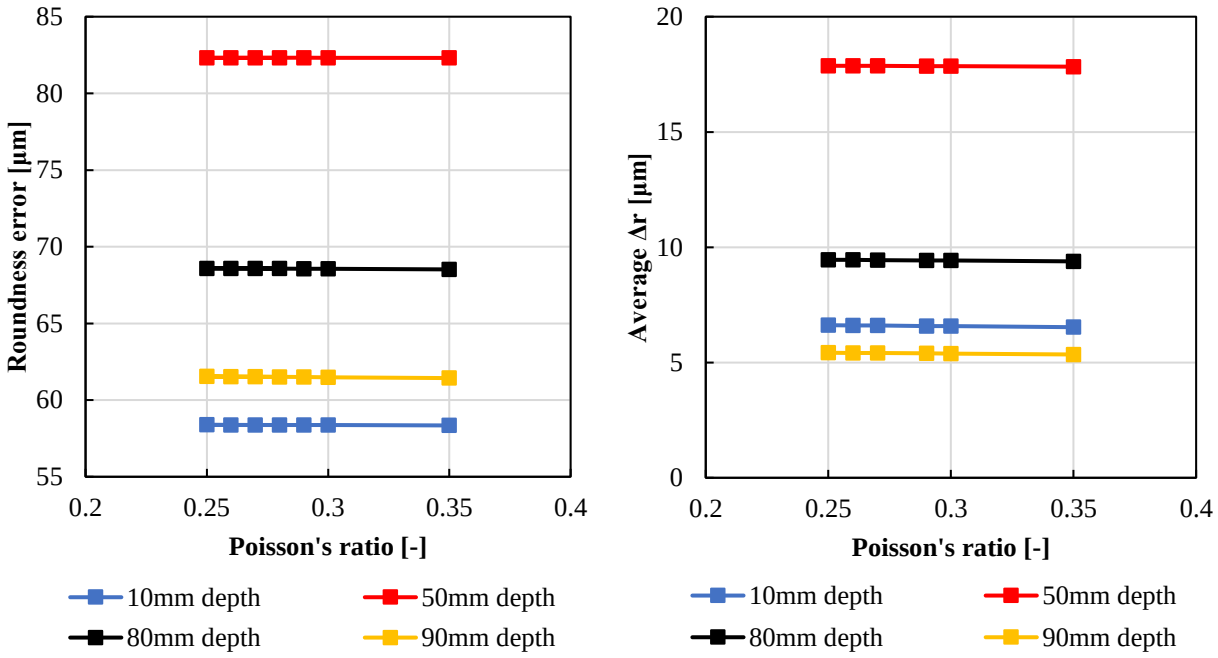

Fig.5-5 Roundness error and average delta radius
while changing Poisson's ratio of the liner

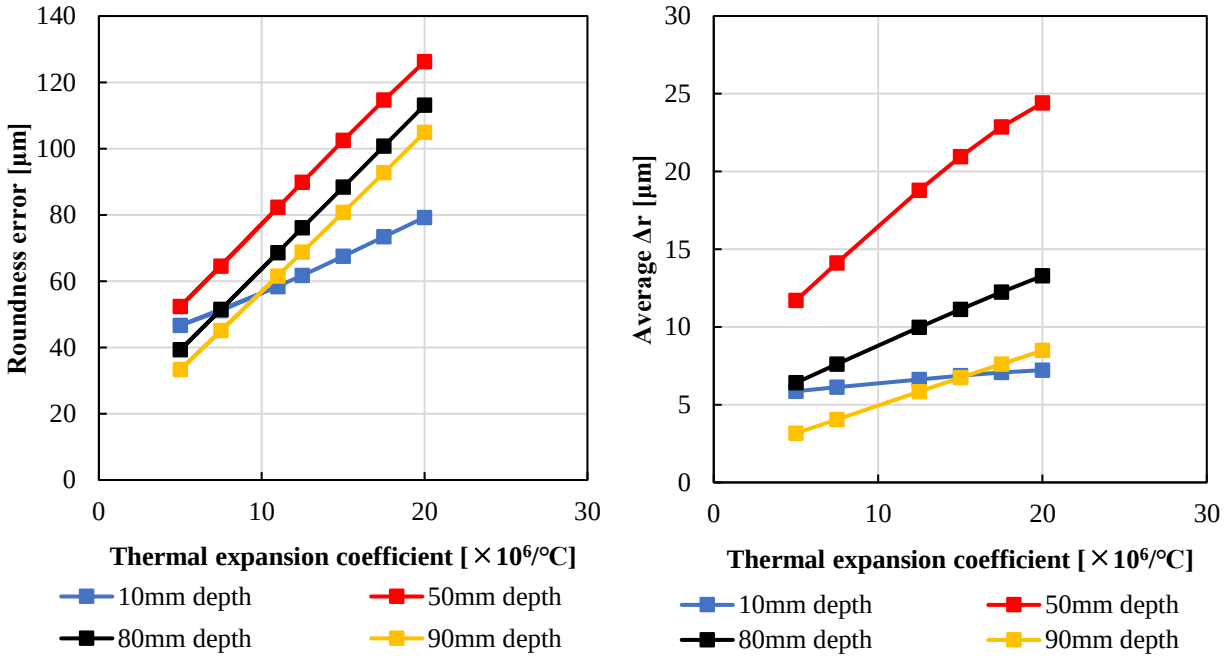

Fig.5-6 Roundness error and average delta radius
while changing TEC of the cylinder block

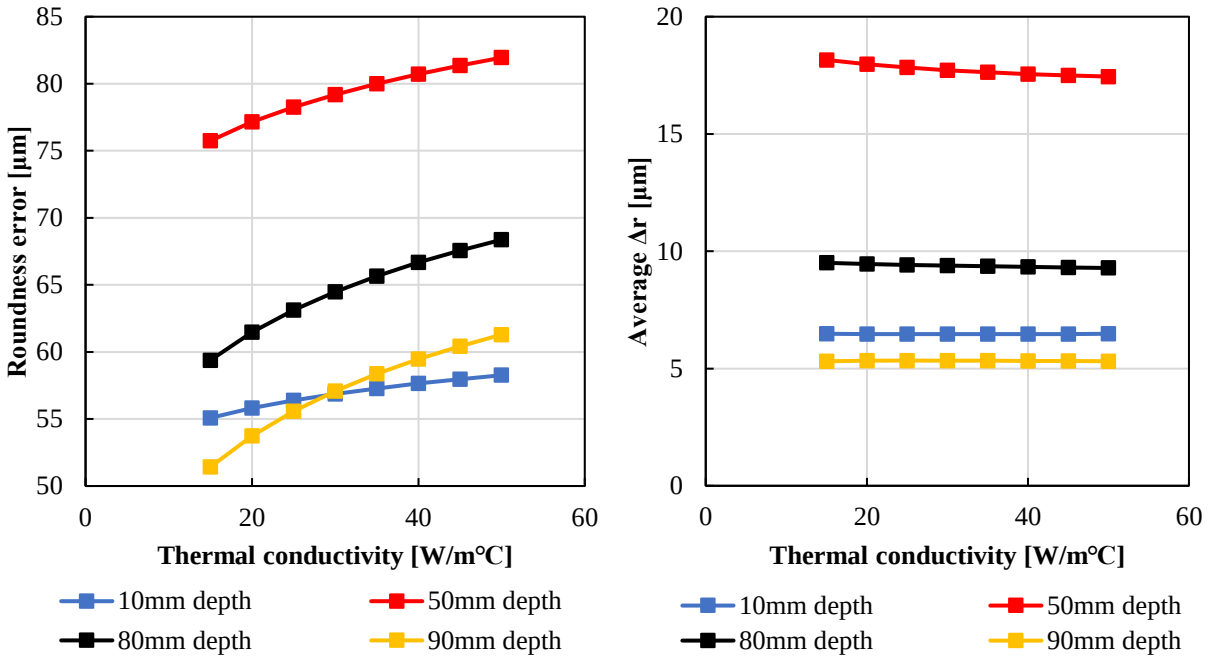

Fig.5-7 Roundness error and average delta radius
while changing thermal conductivity of the cylinder block

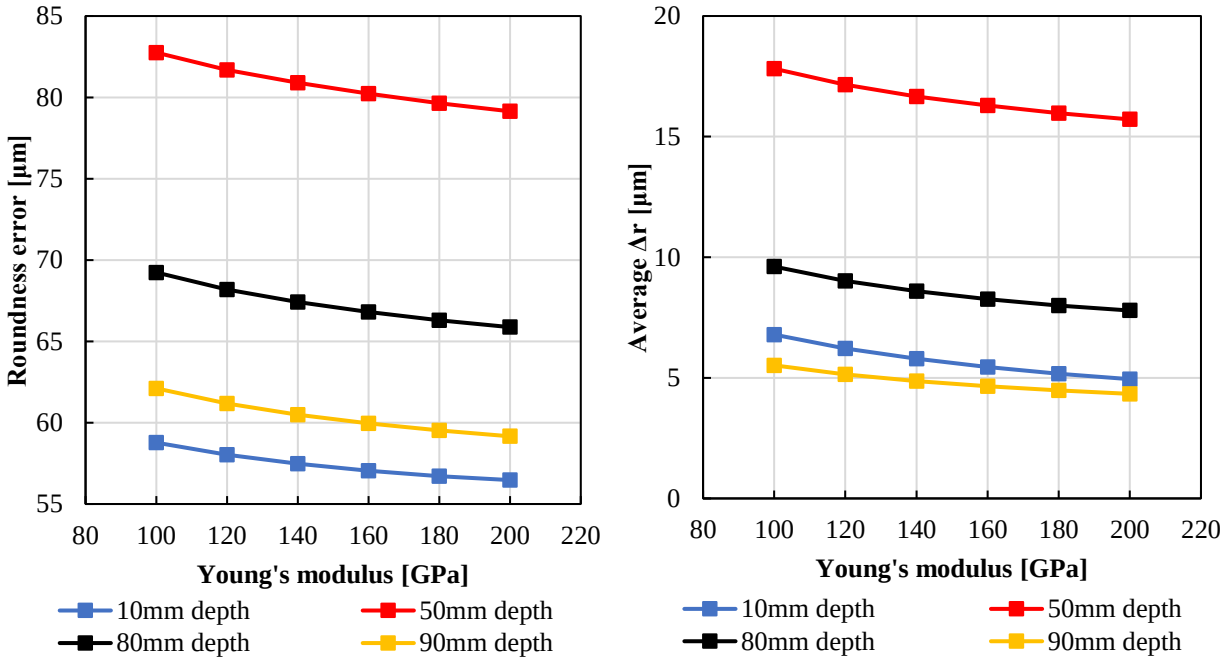

Fig.5-8 Roundness error and average delta radius
while changing Young's modulus of the cylinder block

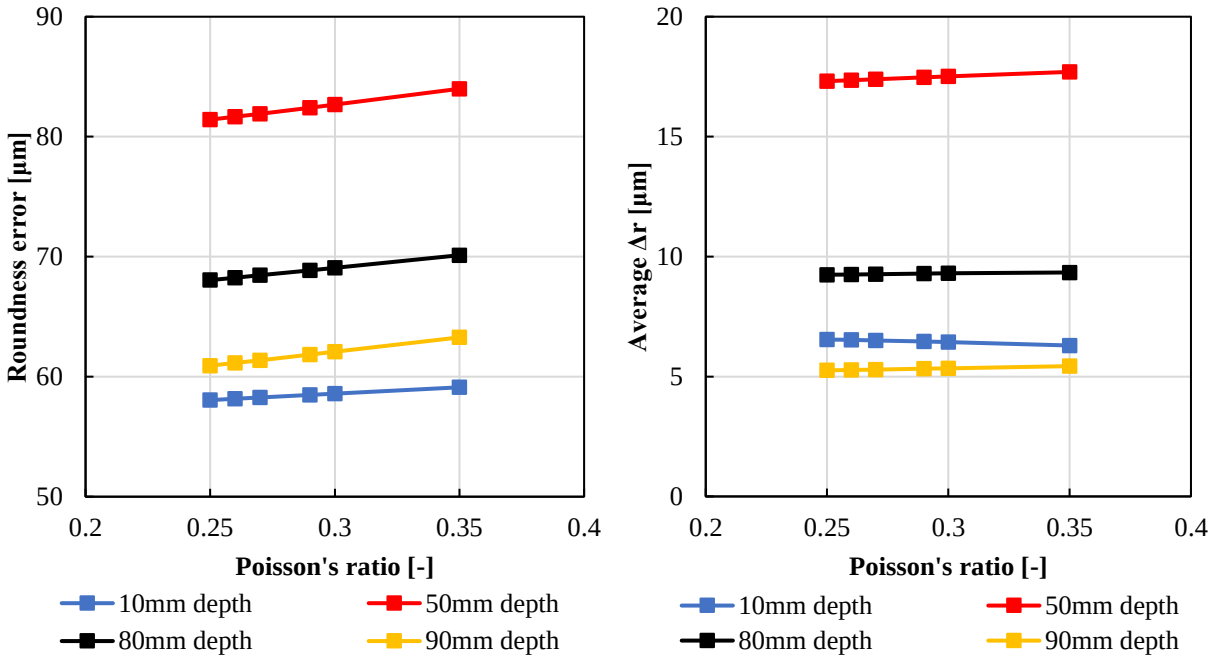

Fig.5-9 Roundness error and average delta radius
while changing Poisson's ratio of the cylinder block

5.2. The bore deformation in various temperature scale with unique thermal expansion coefficient

5.2.1. Thermal expansion coefficient of graphene

In the result of section 5.1, it is found that the TEC is the most affectable property on bore deformation, whose TEC is constant along temperature. But actually, the TEC depends on temperature slightly. Therefore, in this section, the bore deformation with temperature dependent TEC is simulated and the roundness error and average displacement amount of bore radius are calculated.

By the result of section 5.1, the TEC should be negative or around zero in temperature range of engine operation. The general metal or alloy material don't have negative TEC, but the graphene has it according to recent study. The free-standing graphene is observed by Geim AK et al and Novoselov KS et al [19]-[21] for the first time in 2004 and they won the Novel Prize. The graphene is made from the mono layer having honeycomb structure of carbon. Due to this unique structure, graphene has unique physical properties, so it gets highly attention. The TEC is one of the physical properties, which could be negative value in wide range of temperature including room temperature and engine operation temperature. However, there are various opinions about this negative value of the TEC, because this is recent new material and it is difficult to measure precise TEC or other physical properties too. Therefore, three representative TEC is applied in the simulation as TEC of the material property, which are measured or calculated by Mounet N et al [22], Duhee Y et al [23], Shibing T et al [24]. The TEC estimated by

Mounet N et al is based on density functional perturbation theory calculation, so this is a calculated estimation and could not be precise rather than measurement. On the other hand, the TEC estimated by Duhee Y et al is measured using Raman spectroscopy in 2011. Furthermore, Shibing T the free-standing TEC estimated more reliable TEC by measurement considering the mismatch of TEC between graphene and substrate in 2016. Fig.5-10 shows temperature dependency of those TEC properties in temperature range of engine operation. Each three properties are very unique, for example, one has a minimum value and other is changing from negative to positive. Due to these uncertainty and variety of those estimation, all of these three properties are applied as TEC of liner material in the simulation and investigate the effect on bore deformation of the liner.

Fig.5-11 shows the comparison result of roundness error and average displacement amount of bore radius in each 10mm, 50mm, 80mm, 90mm depth of the liner with various three TEC conditions. Comparing the result of gray cast iron, roundness error of simulations by three TEC conditions are reduced especially in 50mm depth from top deck. This cause is seemed that TEC is very close to zero in temperature range of engine operation, from 400K to 500K. The simulations with TEC estimated by Mounet N et al and Duhee Y et al get lower roundness error value than that of Shibing T's but average displacement amount of bore radius is too negative. This means averagely the bore of the liner is shrinking so this leads also increase of lubrication oil consumption. On the other hand, as a result simulated with TEC estimated by Shibing T et al, average displacement amount of bore radius is almost near to zero. This means bore is averagely not expanding or shrinking. This result indicates that TEC like Shibing T's estimation is seemed to be the most optimal value for cylinder liner material to reduce lubrication oil consumption.

Therefore, the graphene has interesting potential to improve the conformability between cylinder liner and piston by reducing roundness error of bore deformation. This estimation would be a key to produce a new alloy material or alloy material concept.

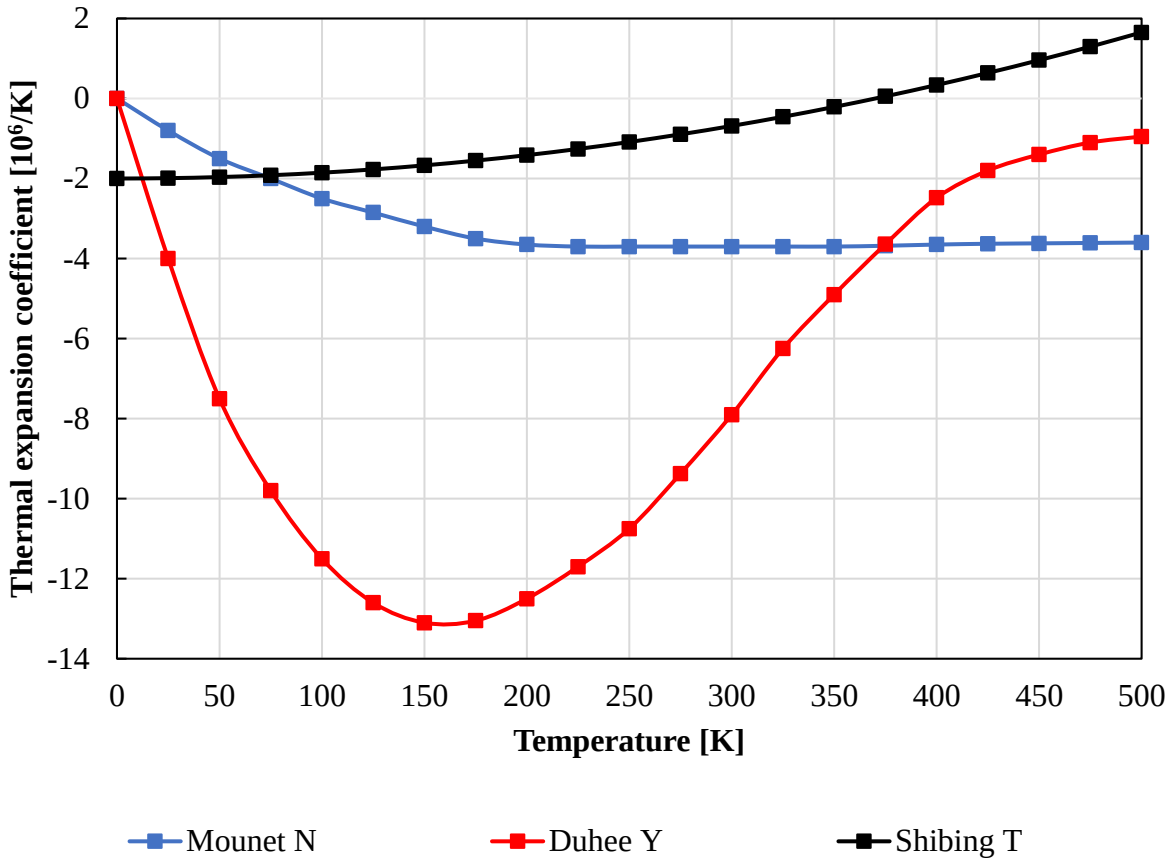

Fig.5-10 Unique thermal expansion coefficient estimated by recent study

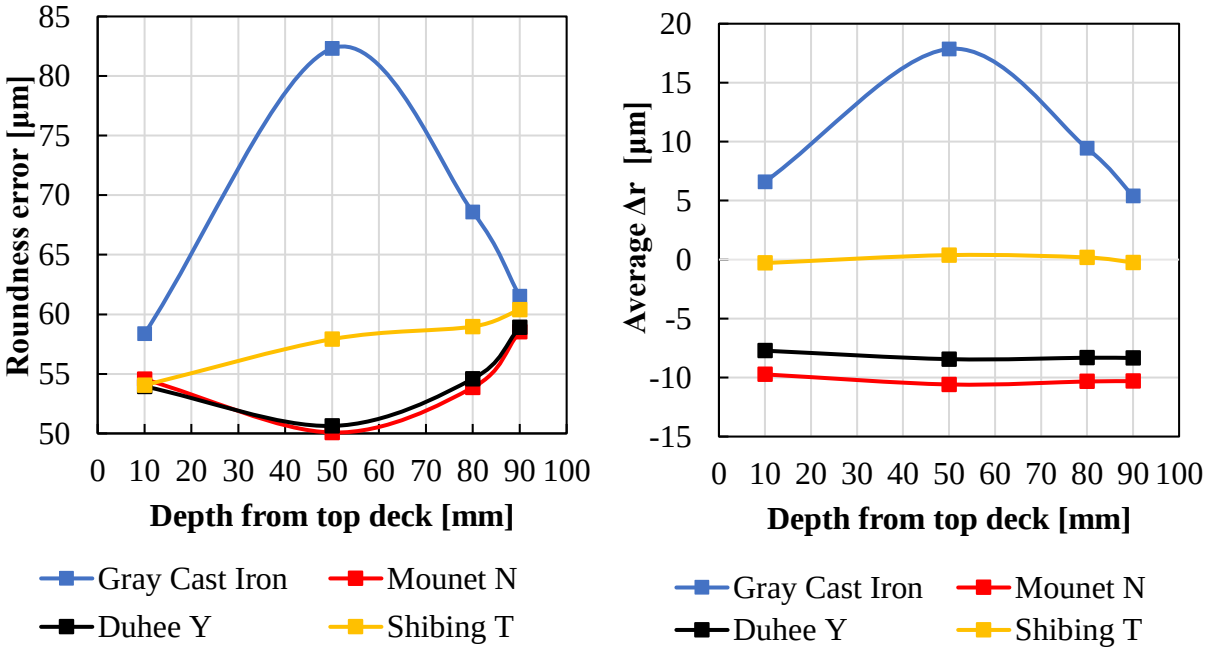

Fig.5-11 Roundness error and average delta radius
with unique TEC parameter of the liner (Temperature scale is 1.0)

5.2.2. The bore deformation in various temperature condition

Section 5.2.1 shows the result simulated 4000rpm full load temperature condition (temperature scale is 1.0). In this section 5.2.2, it is written that how the bore deformation will change when temperature condition is changed.

In order to change temperature condition while keeping the validity of this simulation model, all of applied temperature value as boundary condition is multiplied by temperature scale, which is from 0.95 to 0.7. Fig.5-12 through Fig.5-17 show the temperature distribution of liner and cylinder block with that of experiment conducted by Hitosugi H et al. In the experimental data of these figure, temperature distribution in the condition of 2000rpm 1/4 load, which is approximately the engine operation when standard cars are driven normally, is also show. As shown in Fig.5-16. The simulated temperature distribution is quite similar to experimental temperature data in the condition of 2000rpm 1/4 load when temperature scale is 0.75. Thus, this method to operate simulated temperature condition is still valid.

Next, in the same way as section 5.2.1, roundness error and average displacement amount of bore radius when the temperature scale is changed are investigated. Fig.5-18 through Fig.5-25 show the results simulated with various TEC in various temperature scale, and Fig.1 through Fig.28 show the deformation trend of those. As a simulation result with gray cast iron, the lower the temperature scale is, the lower the roundness error is getting slightly as shown in Fig.5-18 and Fig.5-19. As a simulation result with TEC estimated by Mounet N et al, it is found that roundness error can be reduced especially in bottom of the liner like 90mm depth from top deck when temperature scale is lower as shown in Fig.5-20 and Fig.5-21. Additionally, roundness error is converged to certain value in 80mm and 90mm depth from top deck when temperature scale is lower, but not converged in 10mm depth from top deck. This difference is probably because head cramping force. On the other hand, the average displacement amount of bore radius is getting bigger constantly while temperature scale is getting lower because of negative value of TEC in all temperature range of engine operation. Fig.5-22 and Fig.5-23 show the simulation result with TEC estimated by Duhee Y et al. Both results of roundness error and average displacement amount of bore radius have very similar tendency to that of Mounet N et al. This would be due to same aspect that negative value of TEC in all temperature range of engine operation. Fig.5-24 and Fig.5-25 show the simulation result with TEC estimated by Shibing T et al. While temperature scale is changing to lower, the roundness error in 10mm depth from top deck is getting lower remarkably, but that in bottom of the liner keeps constant. This is probably due to the lower temperature in bottom of the liner comparing top deck temperature. This also means that the liner material having the TEC like Shibing T's estimation can be possible to reduce remarkably lubrication oil consumption from top deck rather than bottom of cylinder especially lower engine speed temperature condition like standard drive. Furthermore, this can prevent blow back, which is gas leakage from crankcase toward combustion chamber.

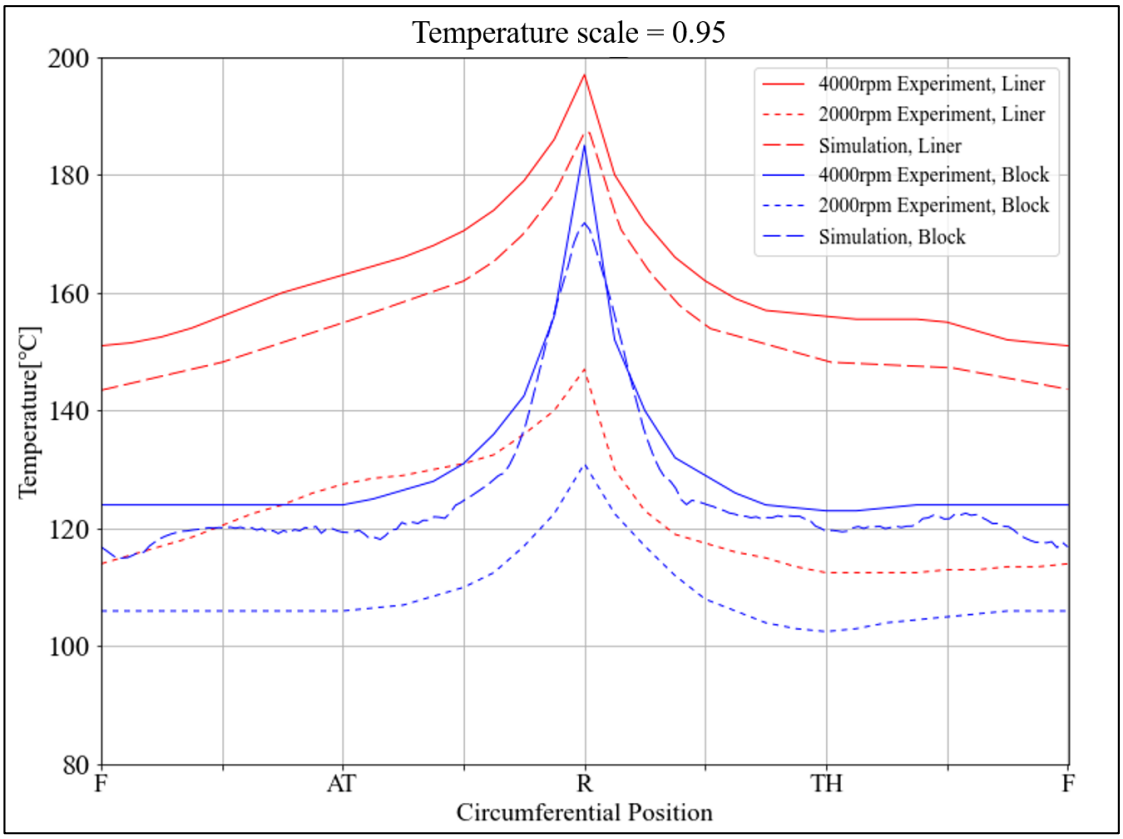

Fig.5-12

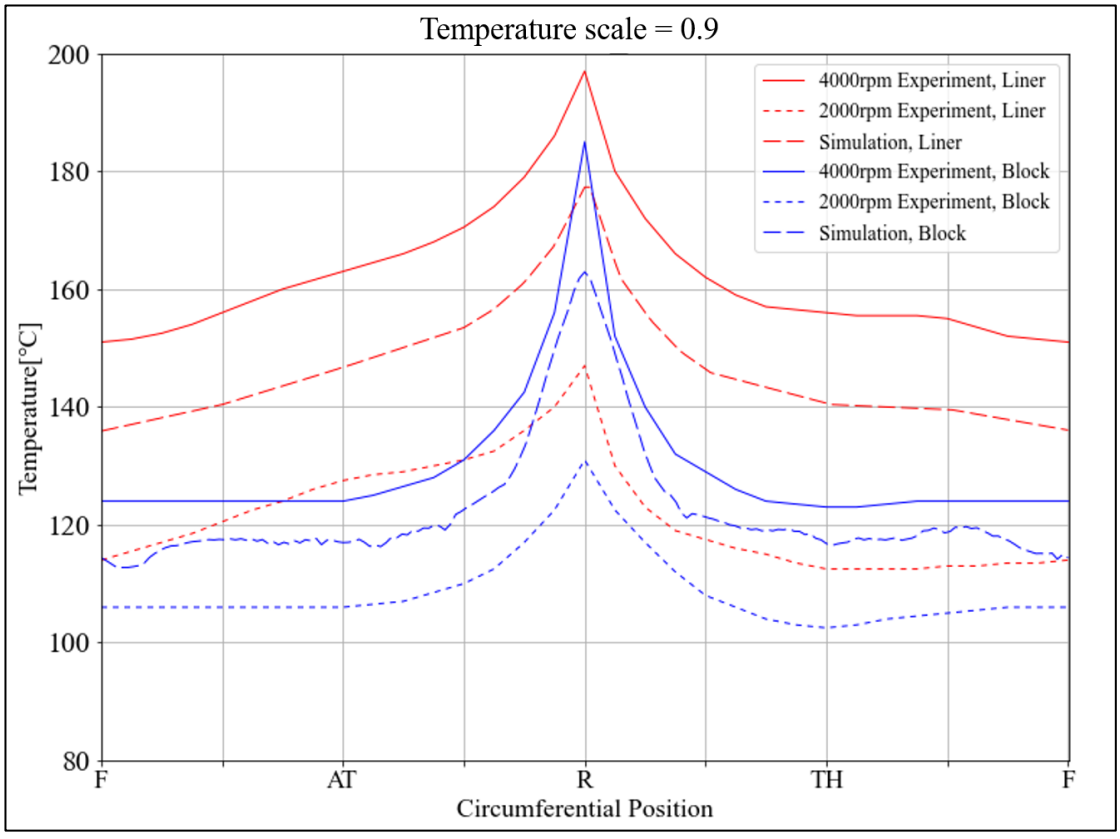

Fig.5-13

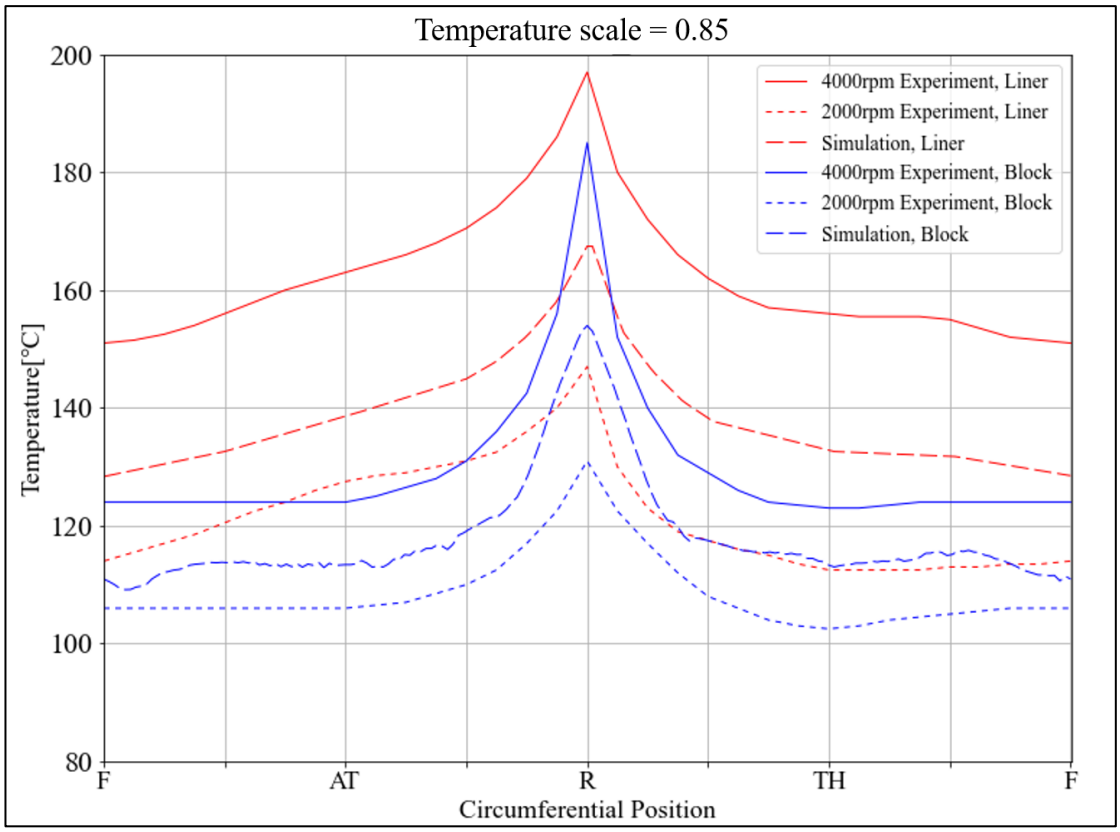

Fig.5-14

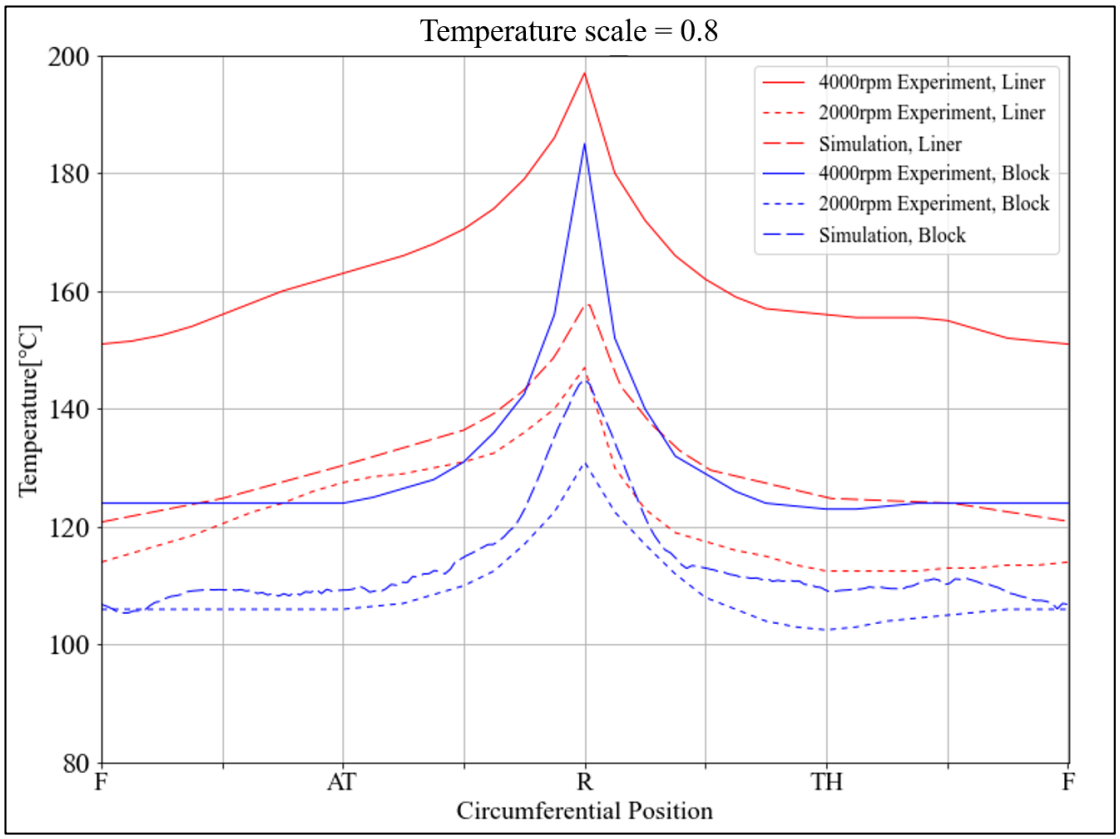

Fig.5-15

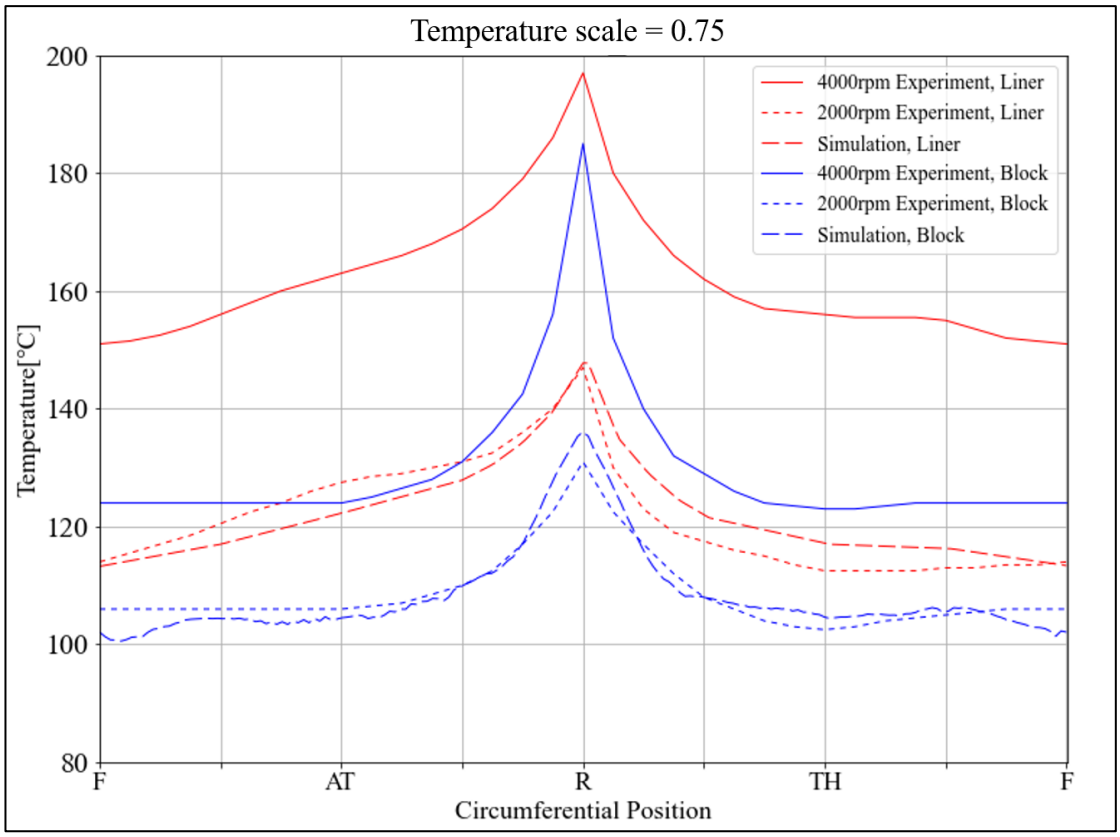

Fig.5-16

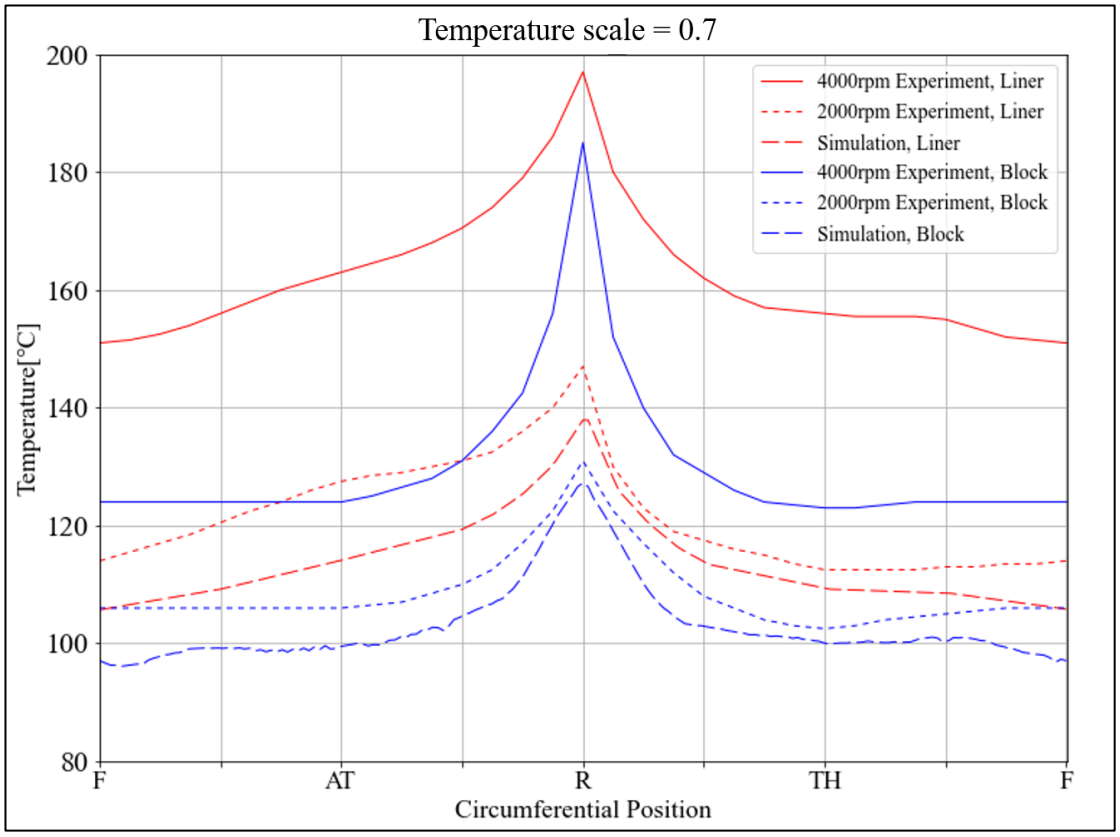

Fig.5-17

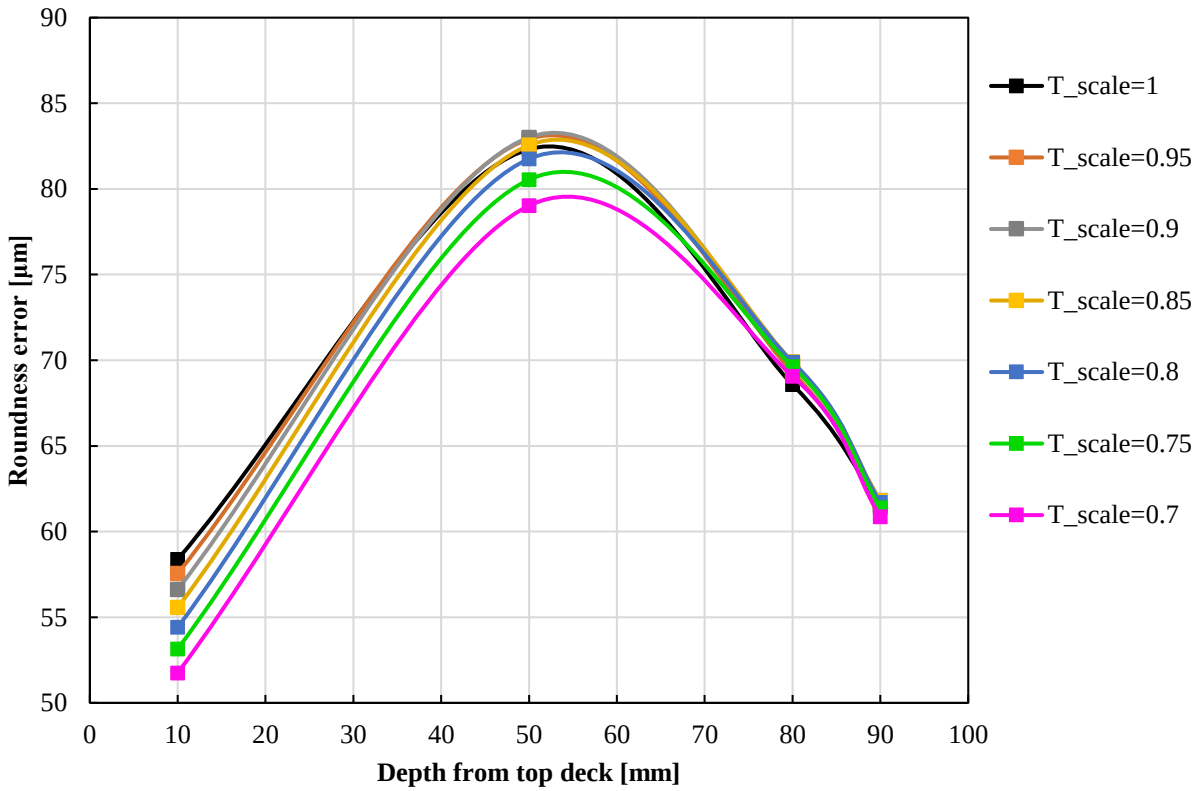

Fig.5-18 Roundness error in various temperature scale condition using gray cast iron

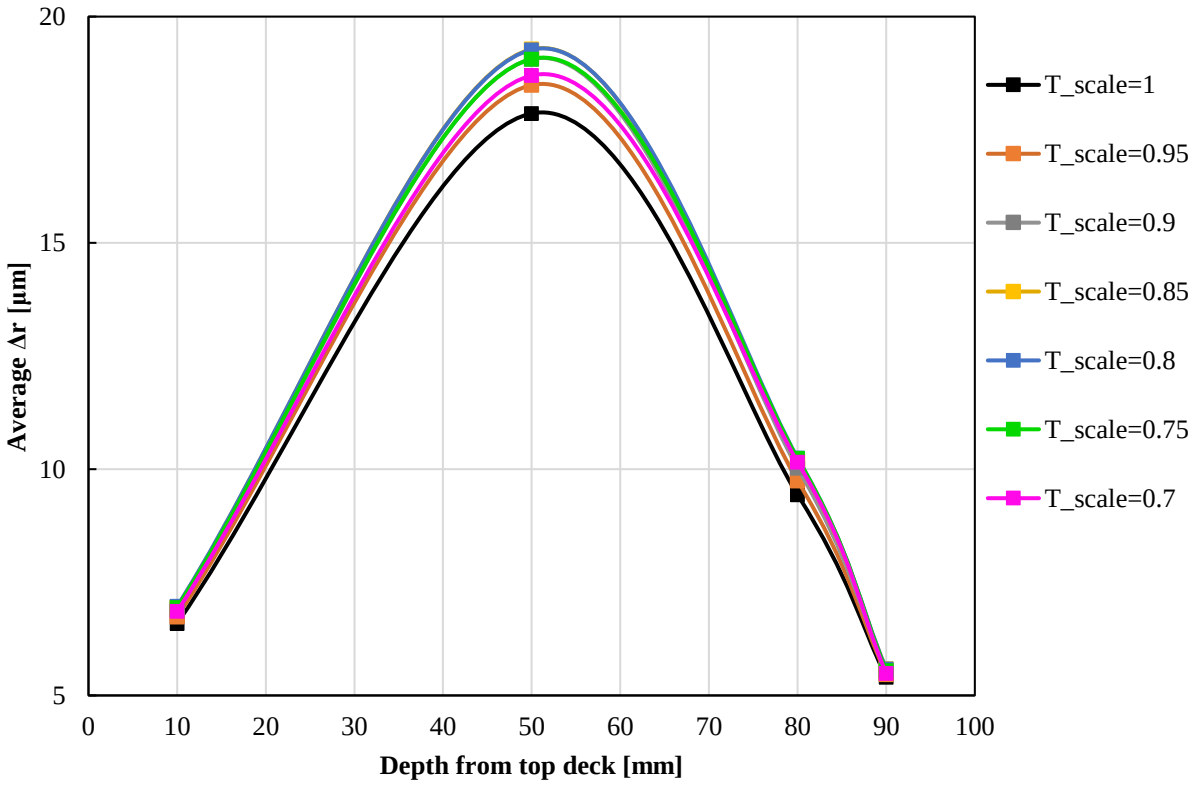

Fig.5-19 Average delta radius in various temperature scale condition using gray cast iron

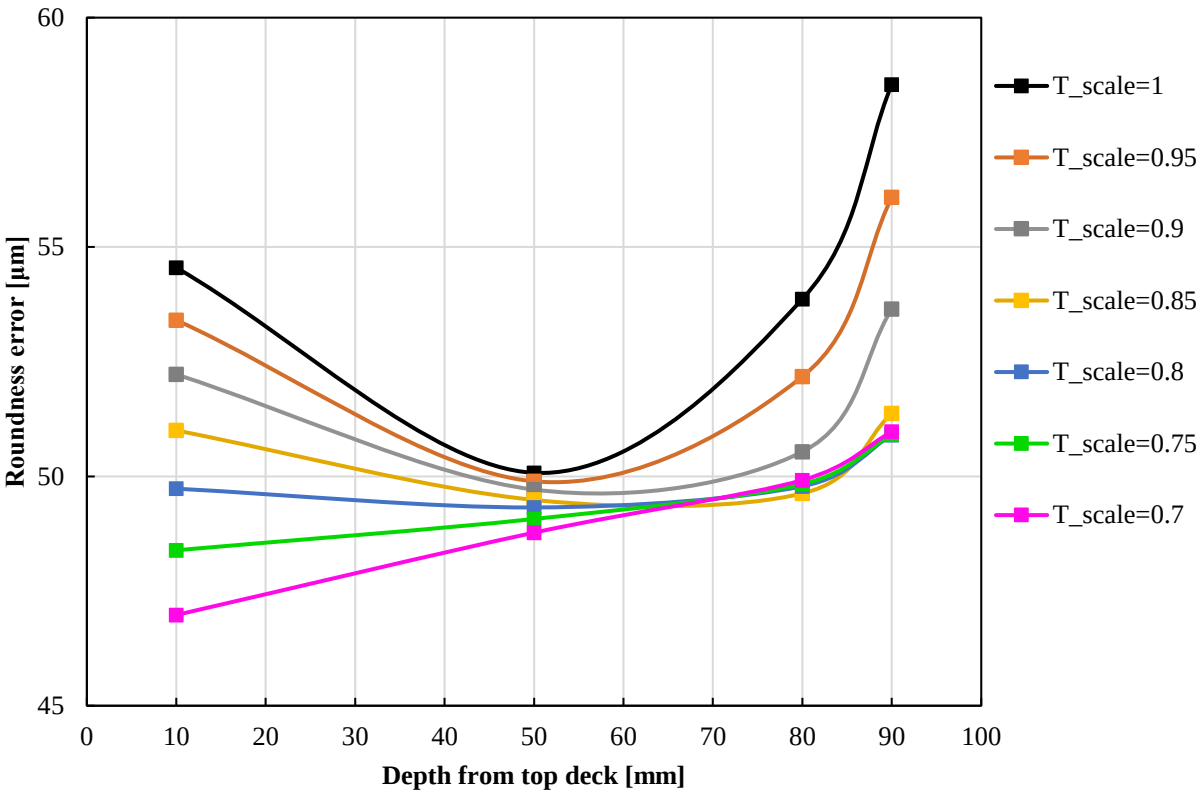

Fig.5-20 Roundness error in various temperature scale condition using TEC estimated by Mounet N

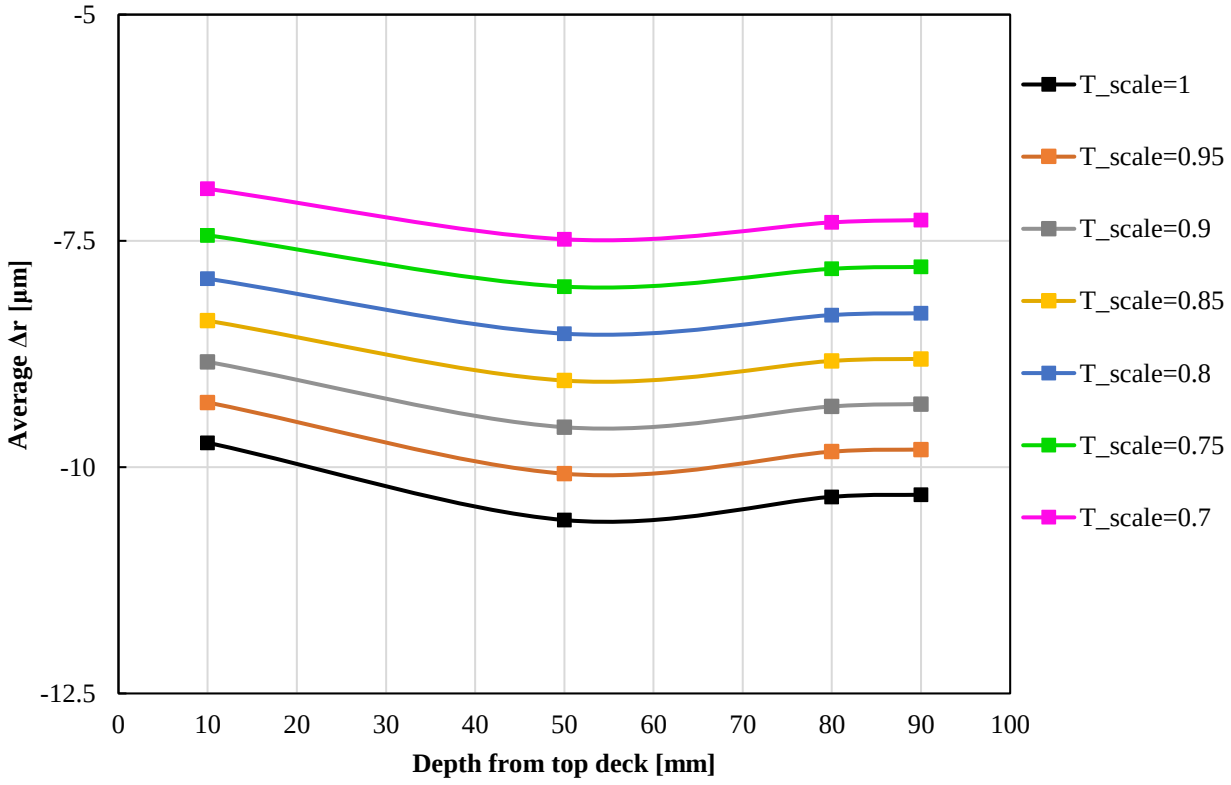

Fig.5-21 Average delta radius in various temperature scale condition using TEC estimated by Mounet N

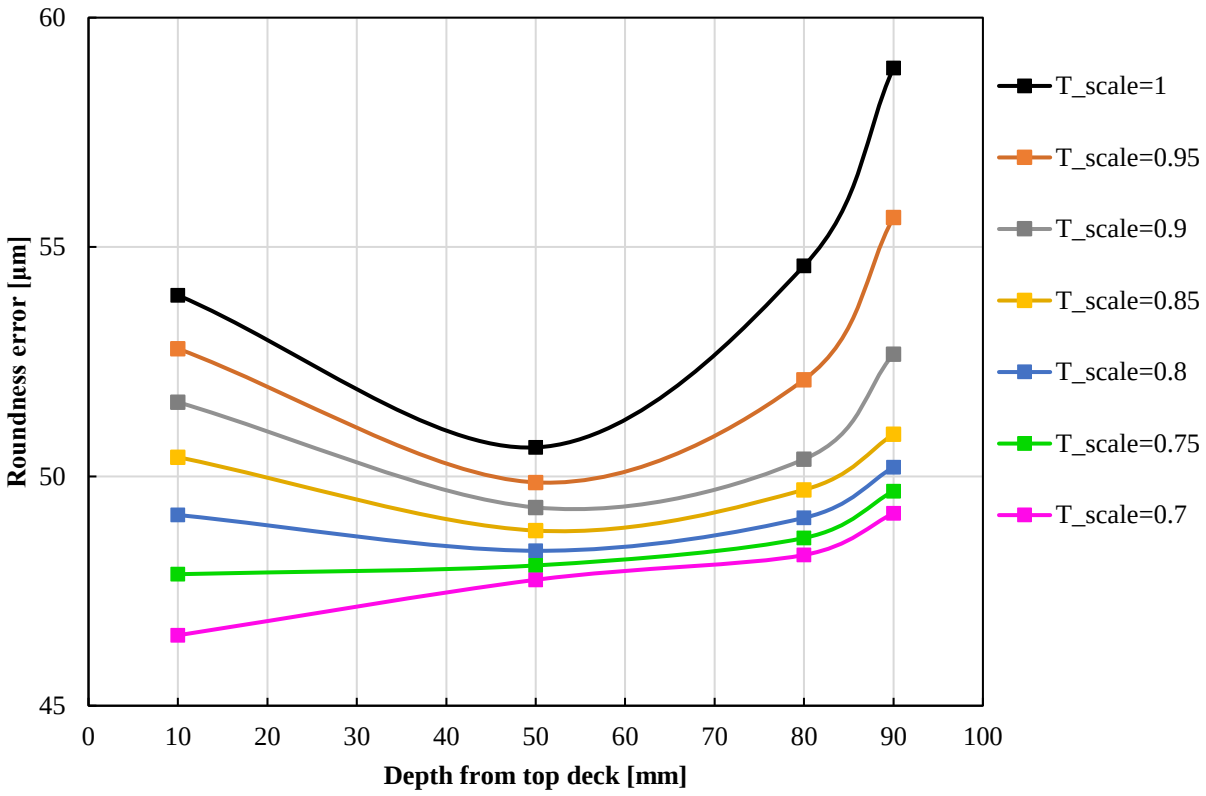

Fig.5-22 Roundness error in various temperature scale condition using TEC estimated by Dohee Y

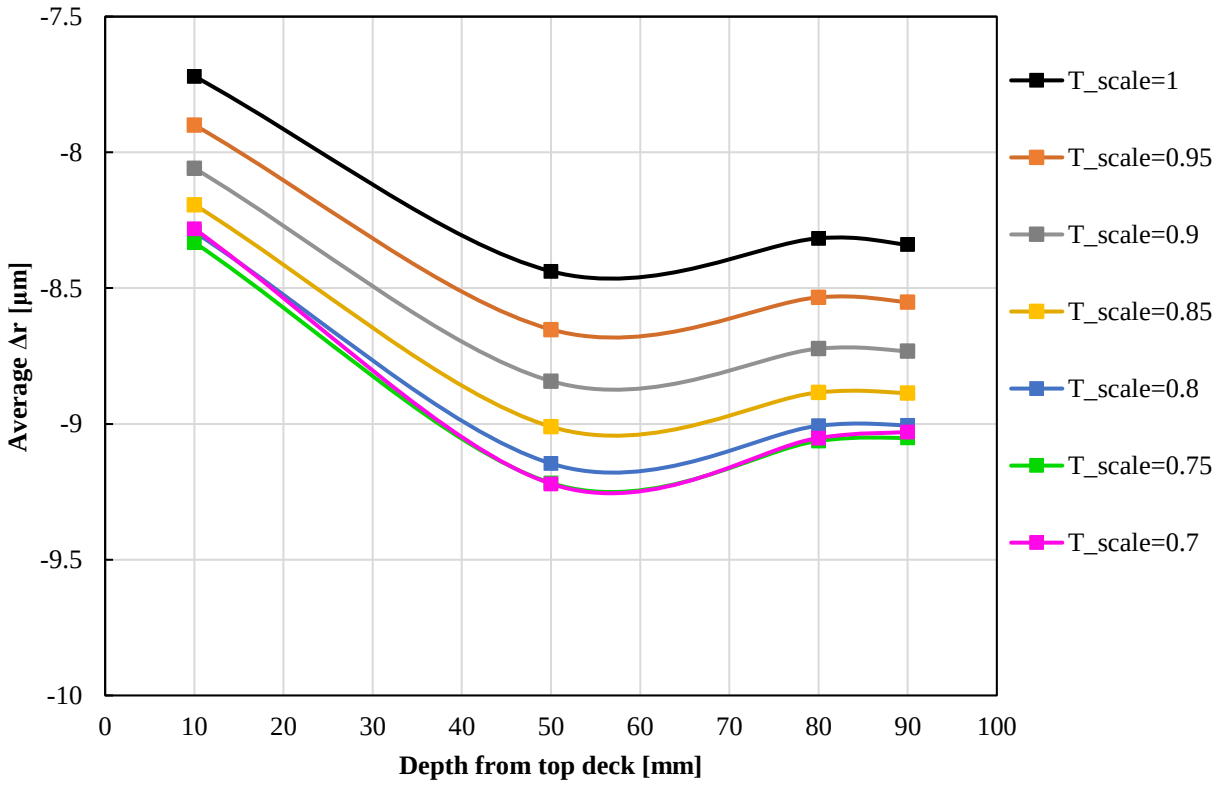

Fig.5-23 Average delta radius in various temperature scale condition using TEC estimated by Dohee Y

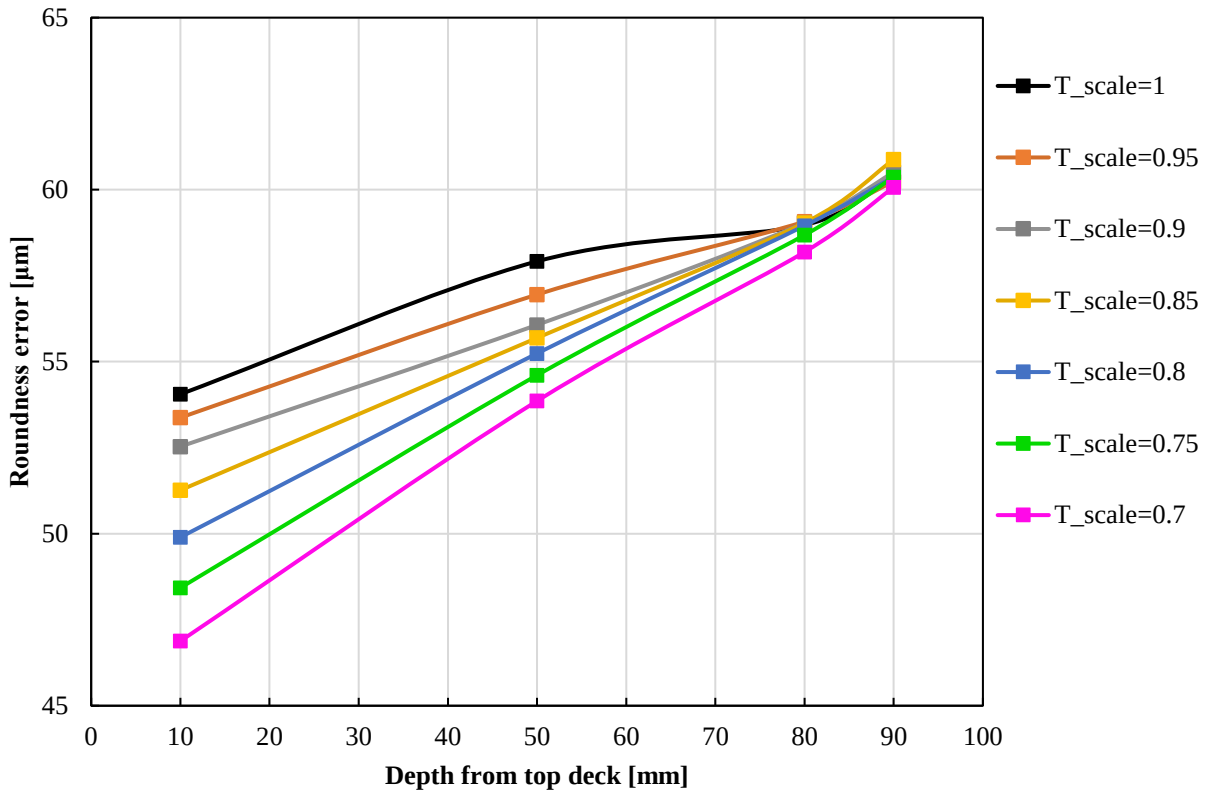

Fig.5-24 Roundness error in various temperature scale condition using TEC estimated by Shibing T

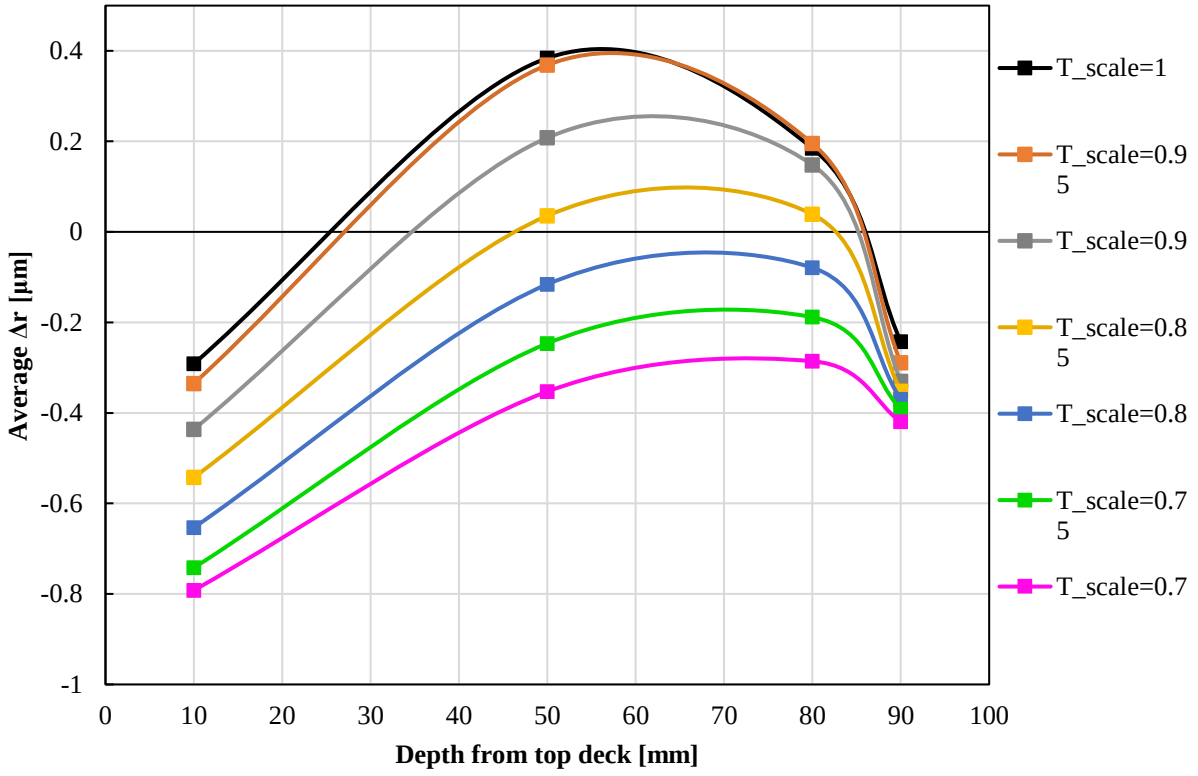

Fig.5-25 Average delta radius in various temperature scale condition using TEC estimated by Shibing T

Chapter 6. Conclusion

In this work, 3D physical model of 4-cylinder, 4-stroke gasoline engine was built and the simulation model for bore deformation of cylinder liner was constructed using 3D-CAE software, ANSYS MECHANICAL. With this original model, various simulations were conducted and these following conclusions was obtained.

- The most affectable material property on bore deformation of the liner is TEC.
- There is a peak of roundness error of the liner around zero while changing TEC of the liner.
- The influence by TEC of the cylinder block on bore deformation is bigger than that of the liner.
- The material having negative thermal expansion coefficient like graphene has remarkable potential improve the conformability between cylinder liner and piston.
- Especially, in lower engine speed condition, there is bigger potential to improve the conformability between cylinder liner and piston.

Acknowledgement

Most of the work was done at the Institute for Technical Combustion in Leibniz University of Hannover in Germany within scientific exchange program under the supervision of Eng. Ahmad Alshwawra.

The author is grateful to Eng. Ahmad Alshwawra at the Institute for Technical Combustion in Leibniz University of Hannover for suggesting the topic treated in this paper. The author also would like to thank him for many important instructions, discussions and technical assistance about the simulation works.

The author is also grateful to Prof. Friedrick Dinkelacker at the Institute for Technical Combustion in Leibniz University of Hannover for providing the author with the opportunity to work there as exchange program and the advices about my simulation work.

The author would like to thank A. prof. Hiroshi Tashima at Engine & Combustion Laboratory in Kyushu University for providing the author with the opportunity to work in the institute for Technical Combustion in Leibniz University of Hannover in Germany. Moreover, the author would like to thank him for fundamental and technical directions on the research work.

The author is also grateful A. Prof. Daisuke Tsuru at Engine & Combustion Laboratory in Kyushu University for many discussions and important advices about this simulation work.

References

[1]. ExxonMobile: “2019 outlook for energy: a perspective to 2040”. ExxonMobile, 28th Aug 2019.
https://corporate.exxonmobil.com/-/media/Global/Files/outlook-for-energy/2019-Outlook-for-Energy_v4.pdf

[2]. UNFCCC: “Paris Agreement”. 2015.
https://unfccc.int/sites/default/files/english_paris_agreement.pdf

[3]. UNFCCC: “Kyoto Protocol”. 1997.
https://unfccc.int/sites/default/files/08_unfccc_kp_ref_manual.pdf

[4]. IPCC (The Intergovernmental Panel on Climate Change)
https://www.ipcc.ch/

[5]. Gu C, Meng X, Xie Y and Zhang D: “The influence of surface texturing on the transition of the lubrication regimes between a piston ring and a cylinder liner”. Int J Engine Res, 2017, 18 (8), 785–796.

[6]. Li T, Ma X, Lu X, Wang C, Jiao B, Xu H and Zou D: “Lubrication analysis for the piston ring of a two-stroke marine diesel engine taking account of the oil supply”. Int J Engine Res, 2019.
https://doi.org/10.1177/1468087413519783

[7]. Hitosugi H, Nagoshi K, Ebina M and Furuhata S: “Study on cylinder bore deformation of dry liner in engine operation”. JSAE Rev, 1996, 17 (2), 113–119.

[8]. Styles G, Rahmani R, Rahnejat H and Fitzsimons B: “Incycle and life-time friction transience in piston ring–liner conjunction under mixed regime of lubrication”. Int J Engine Res, 2014, 15 (7), 862–876.

[9]. Delprete C, Razavykia A: “Piston dynamics, lubrication and tribological performance evaluation”. Int J Engine Res, 2018, 21(5), 725-741.

[10]. Koch F, Decker P, Gu¨lpen R, Quadflieg F-J and Loeprecht M: “Cylinder liner deformation analysis-measurements and calculations”. SAE Int J Engines, 1998, 107 (3), 838–847.

[11]. Alshwawra A, Pohlmann-Tasche F, Stelljes F and Dinkelacker F: “Enhancing the geometrical performance using initially conical cylinder liner in internal combustion engines-A numerical study”. Appl Sci, 2020, 10 (11), 3705.

[12]. Alshwawra A, Pasligh H, Hansen H and Dinkelacker F: “Increasing the roundness of deformed cylinder liner in internal combustion engines by using a non-circular liner profile”. Int J Engine Res, 2019.
https://doi.org/10.1177/1468087419893897

[13]. ANSYS documentation:
https://ansyshelp.ansys.com/account/secured?returnurl=/Views/Secured/main_page.html?v=2

01
[14]. Sui W and Zhang D: “Four methods for roundness evaluation”. Phys Procedia, 2012, 24 (C), 2159–2164.
[15]. Zakharov OV, Bobrovskij IN and Kochetkov AV: “Analysis of methods for estimation of machine work piece roundness”. Procedia Eng 2016, 150, 963–968.
[16]. Montgomery J: “Boundary Condition Influences on Shank Stress in 3D Solid Bolt Simulation”. Abaqus Users' Conference, 2008, 1-18.
[17]. JIS (Japanese Industrial Standard): https://www.jisc.go.jp/app/jis/general/GnrJISSearch.html
[18]. Karamangil MI, Kaynakli O and Surmen A: “Parametric investigation of cylinder and jacket side convective heat transfer coefficients of gasoline engines”. Energy Conversion and Management, 2006, 47 (6), 800–816.
[19]. Novoselov KS, Geim AK, Morozov SV, Jiang D, Zhang Y, Dubonos SV, Grigorieva IV and Firsov AA: “Electric field effect in atomically thin carbon films”. Science, 2004, 306 (5696), 666-669.
[20]. Novoselov KS, Jiang D, Schedin F, Booth TJ, Khotkevich VV, Morozov SV and Geim AK: “Two-dimensional atomic crystals”. Proceedings of the National Academy of Sciences, 2005, 102 (30), 10451-10453.
[21]. Geim AK and Novoselov KS: “The rise of graphene”. Nat. Mater, 2007, 6(3), 183-191.
[22]. Mounet N and Marzari N: “First-principles determination of the structural, vibrational and thermodynamic properties of diamond, graphite, and derivatives”. Physical Review B, 2005, 71 (20), 205214.
[23]. Duhee Y, Young-Woo S and Hyeonsik C: “Negative Thermal Expansion Coefficient of Graphene Measured by Raman Spectroscopy”. Nano Lett, 2011, 11 (8), 3227-3231.
[24]. Shibing T, Yang Y, Zhe L, Chao W, Ruhao P, Changzhi G and Junjie L: “Temperature-dependent Raman investigation on suspended graphene: contribution from thermal expansion coefficient mismatch between graphene and substrate”. Carbon, 2016, 104, 27-32.

Appendix

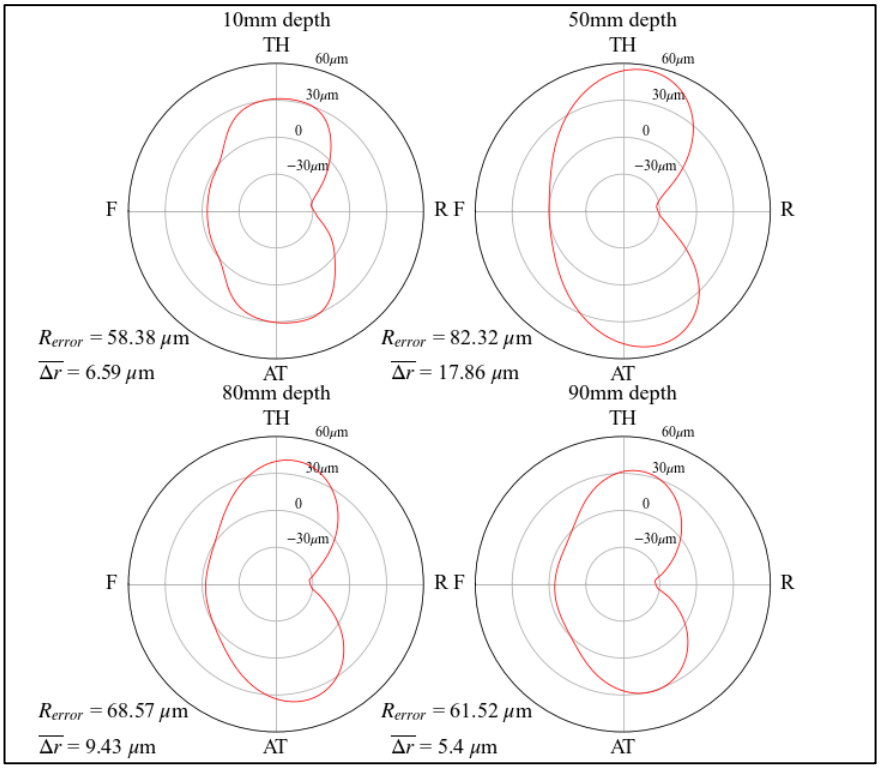

Fig.1 temperature scale is 1.0 using gray cast iron

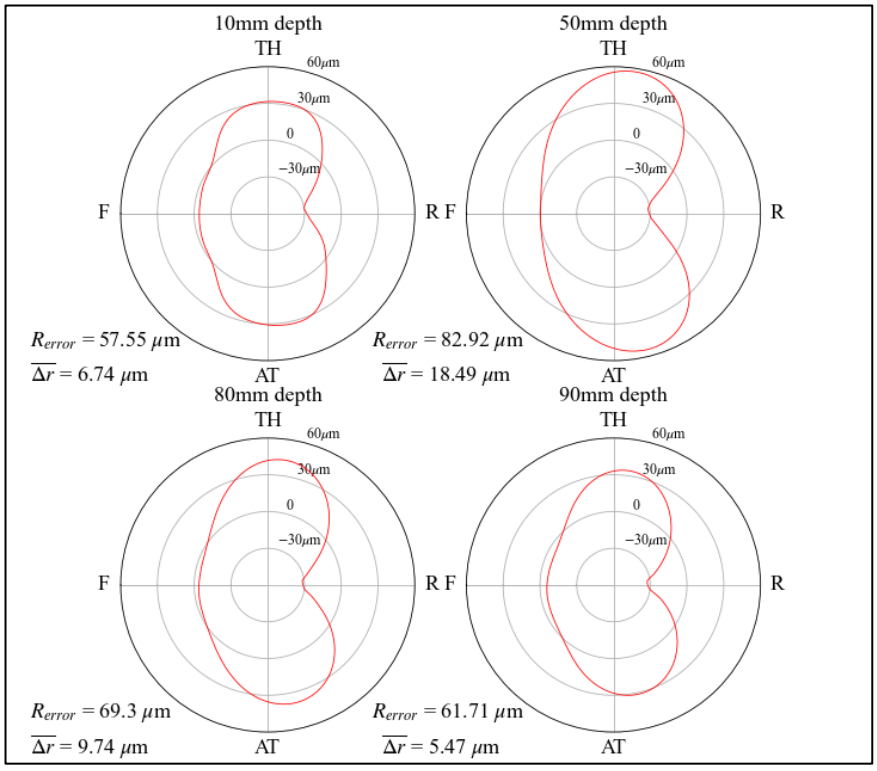

Fig.2 temperature scale is 0.95 using gray cast iron

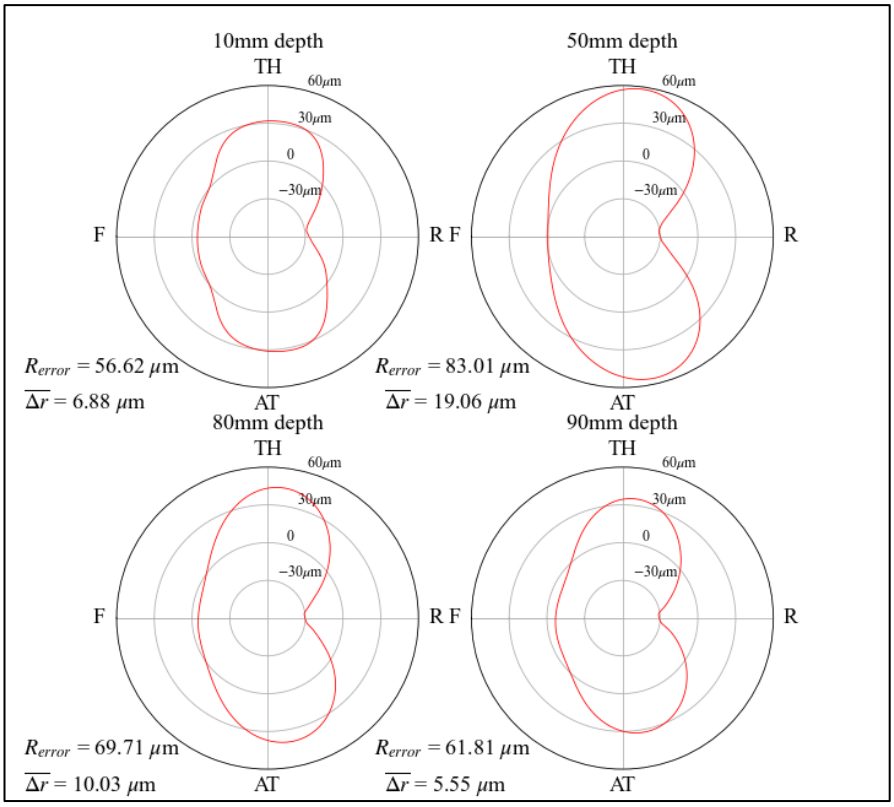

Fig.3 temperature scale is 0.9 using gray cast iron

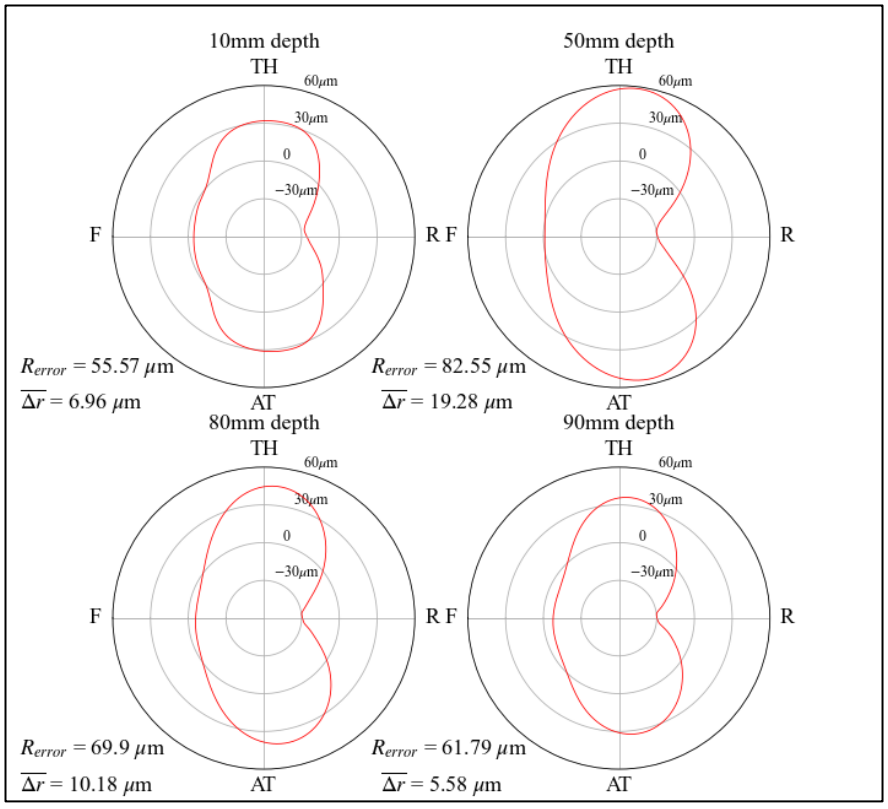

Fig.4 temperature scale is 0.85 using gray cast iron

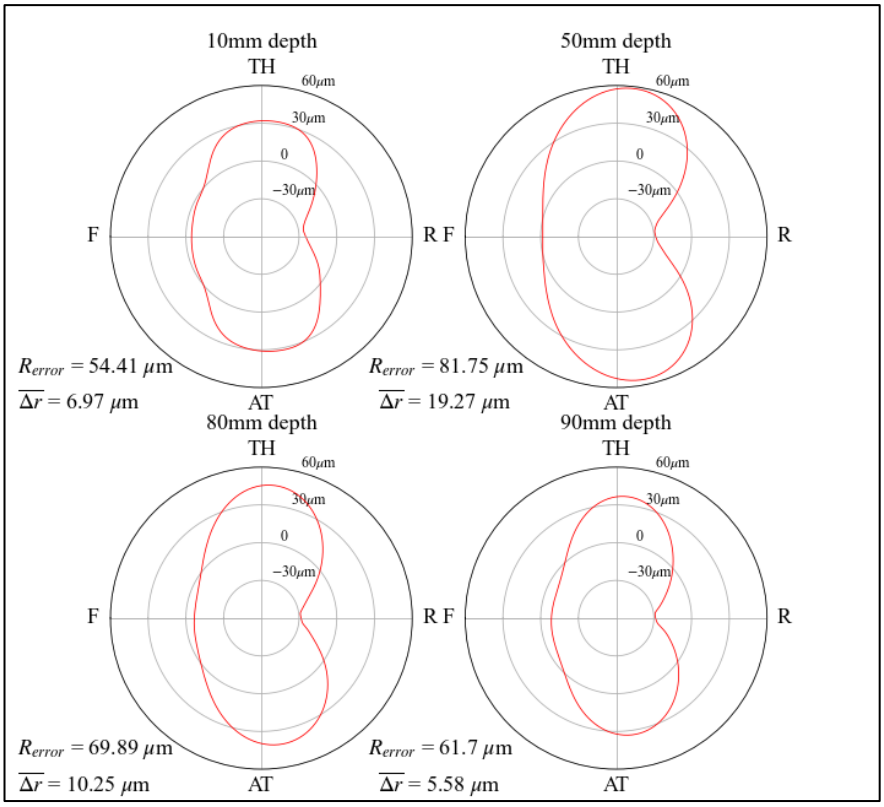

Fig.5 temperature scale is 0.8 using gray cast iron

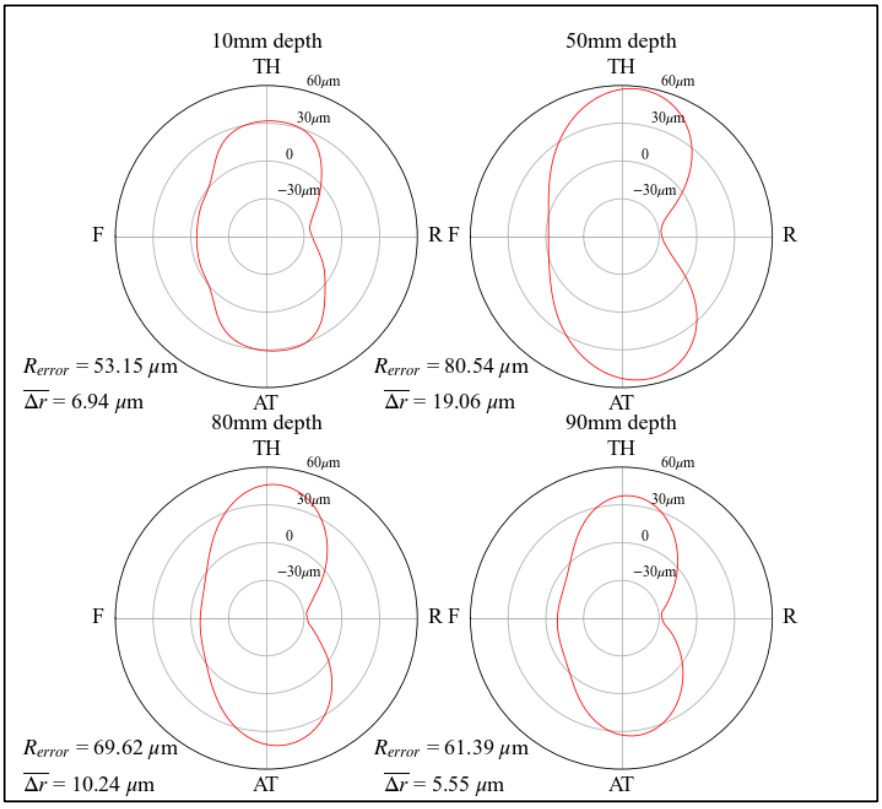

Fig.6 temperature scale is 0.75 using gray cast iron

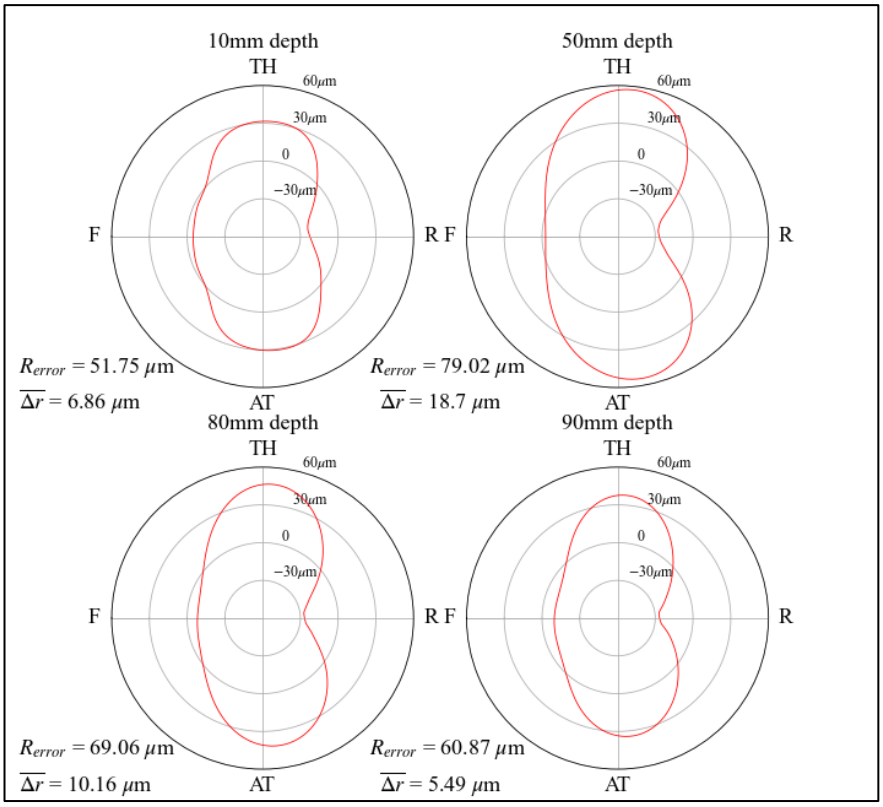

Fig.7 temperature scale is 0.7 using gray cast iron

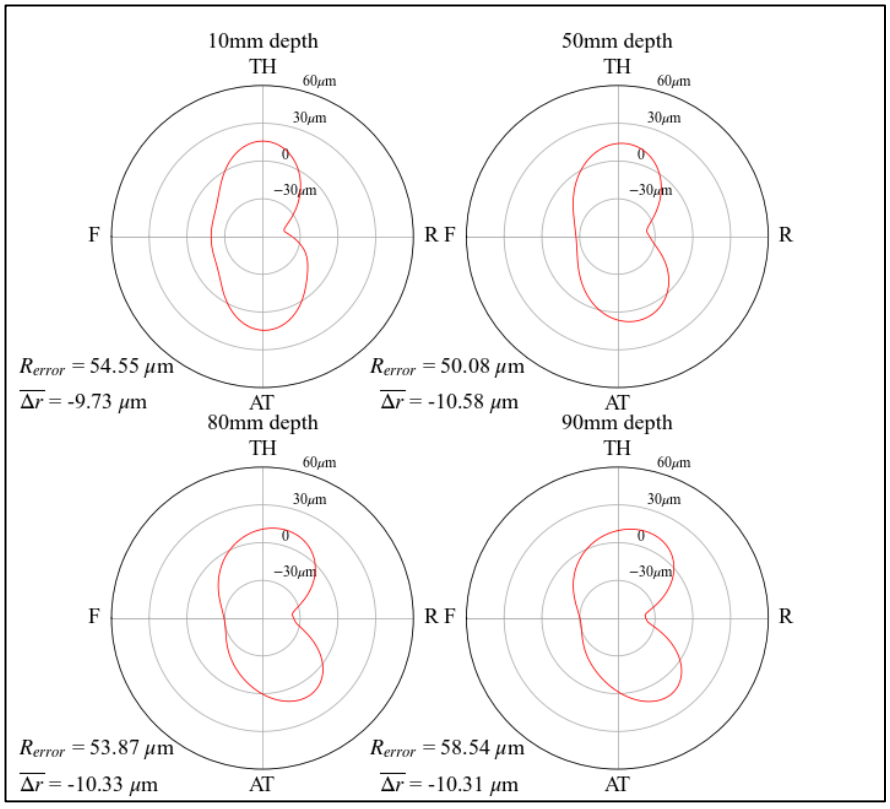

Fig.8 temperature scale is 1.0 using TEC estimated by Mounet N

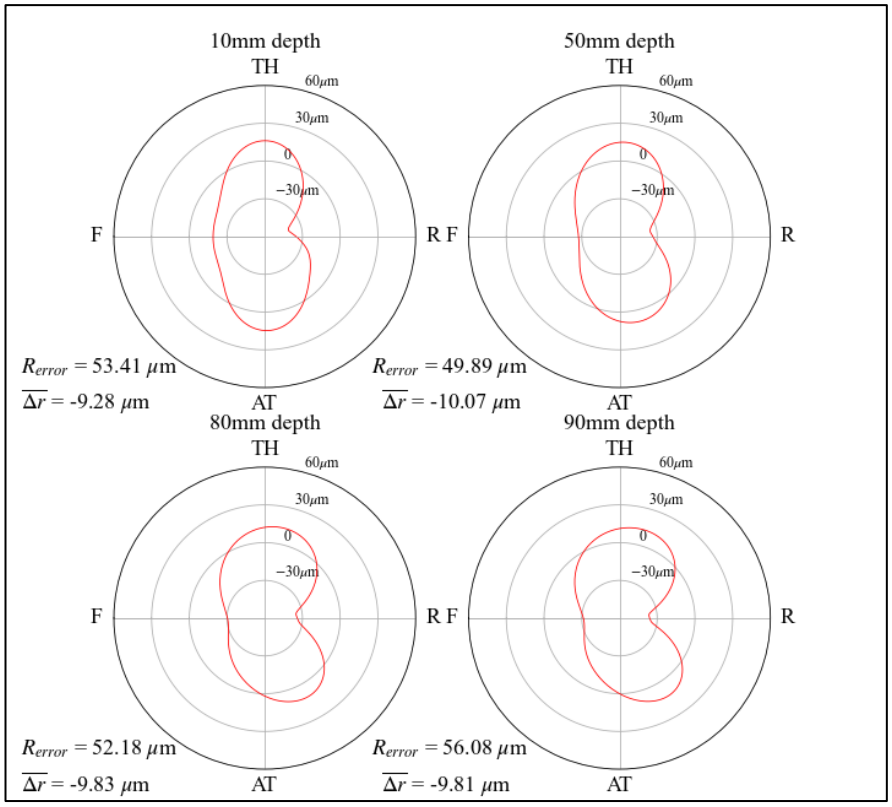

Fig.9 temperature scale is 0.95 using TEC estimated by Mounet N

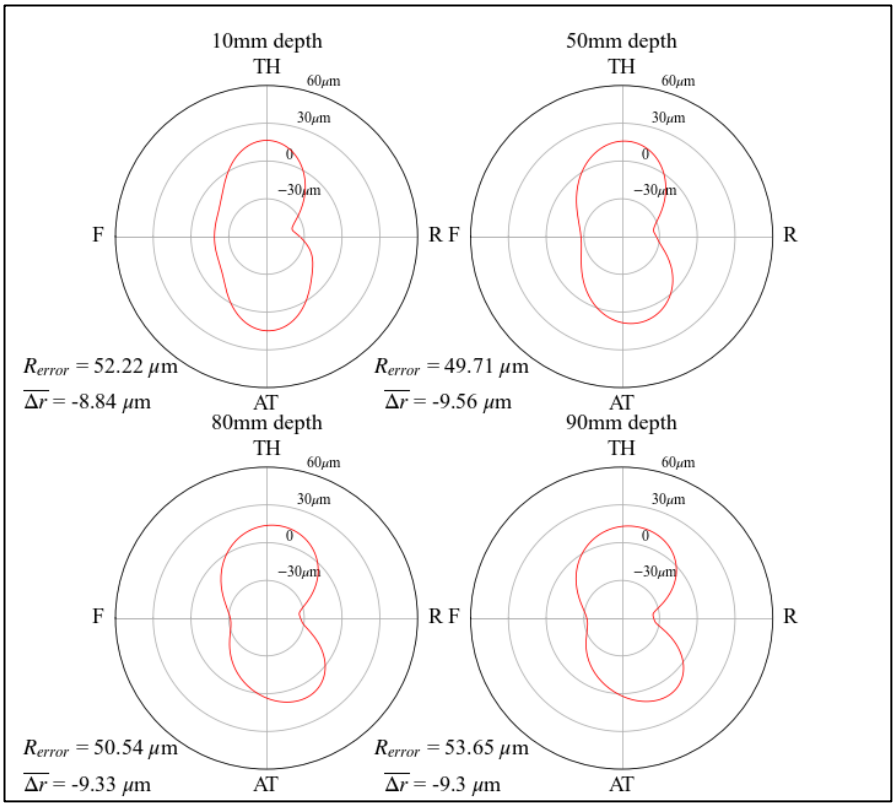

Fig.10 temperature scale is 0.9 using TEC estimated by Mounet N

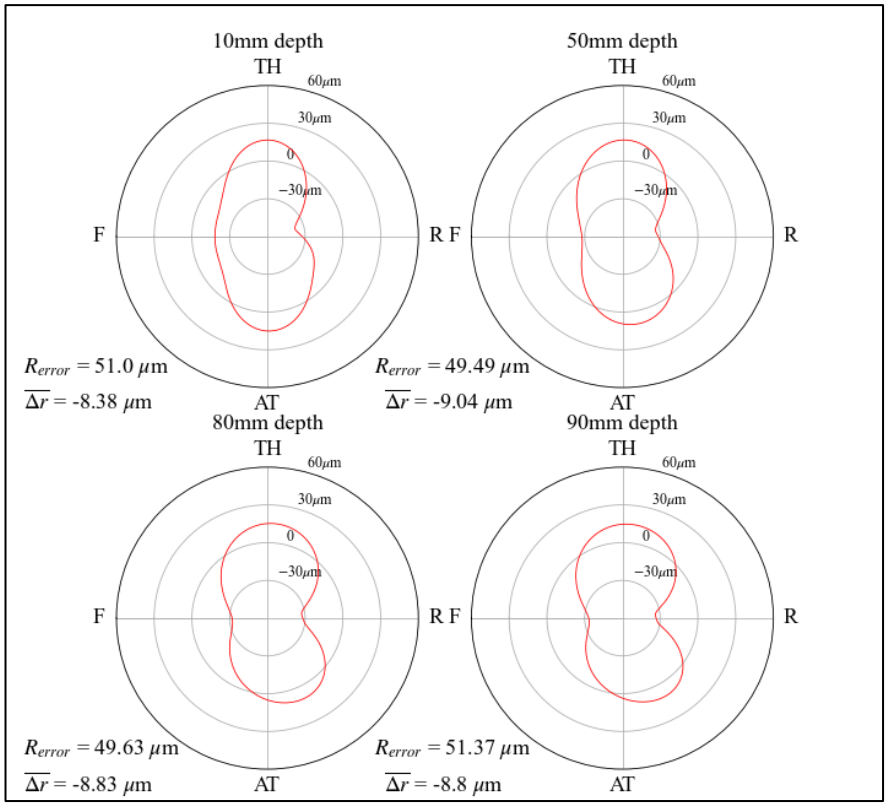

Fig.11 temperature scale is 0.85 using TEC estimated by Mounet N

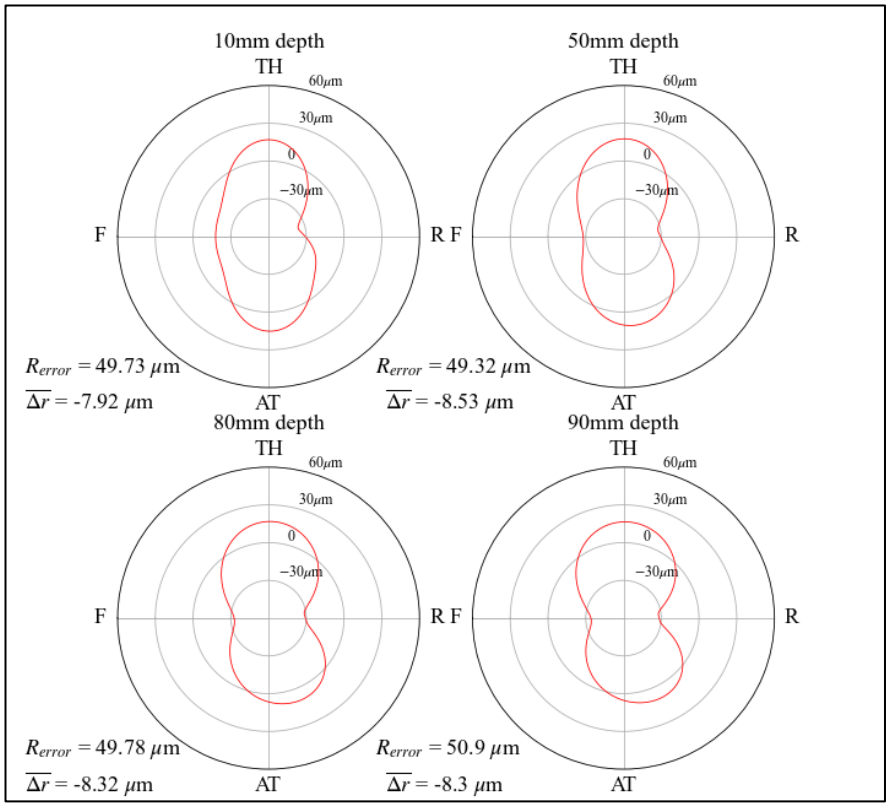

Fig.12 temperature scale is 0.8 using TEC estimated by Mounet N

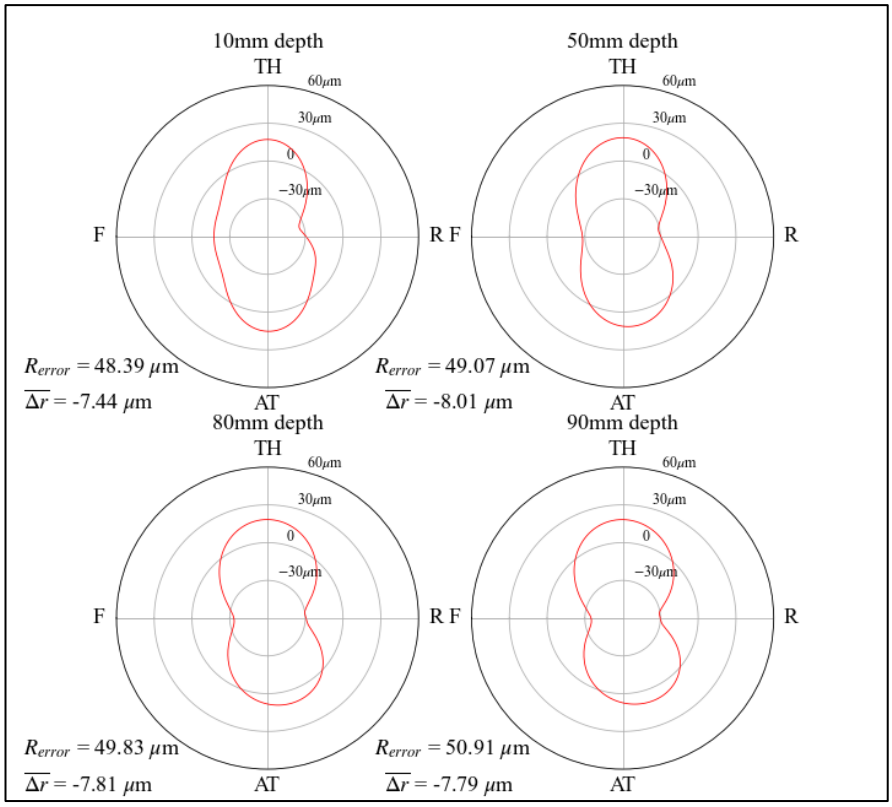

Fig.13 temperature scale is 0.75 using TEC estimated by Mounet N

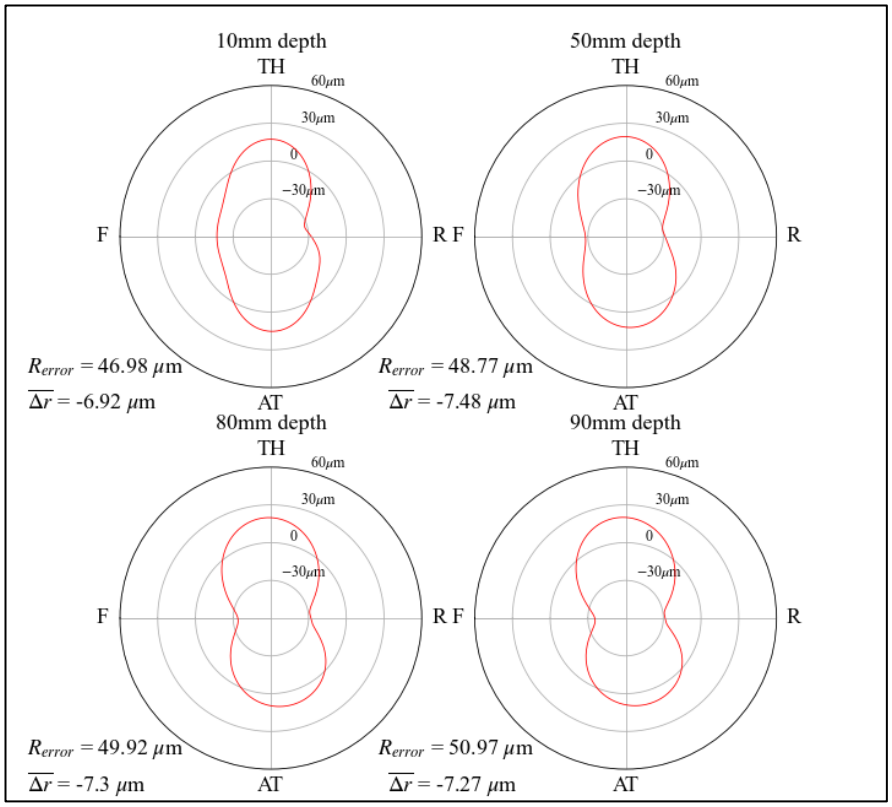

Fig.14 temperature scale is 0.7 using TEC estimated by Mounet N

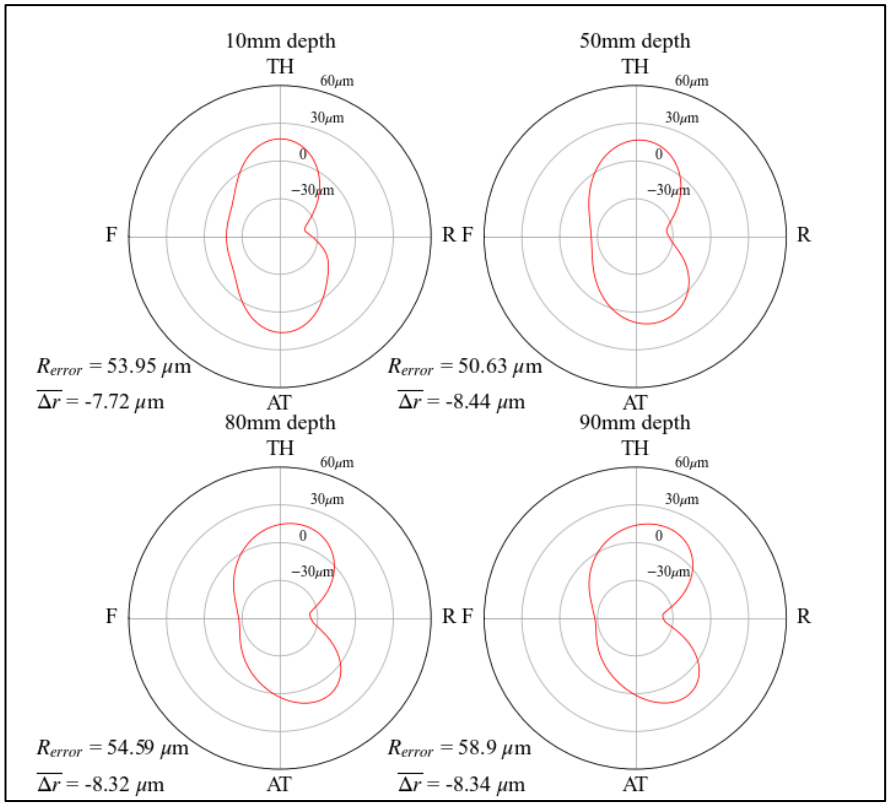

Fig.15 temperature scale is 1.0 using TEC estimated by Dohee Y

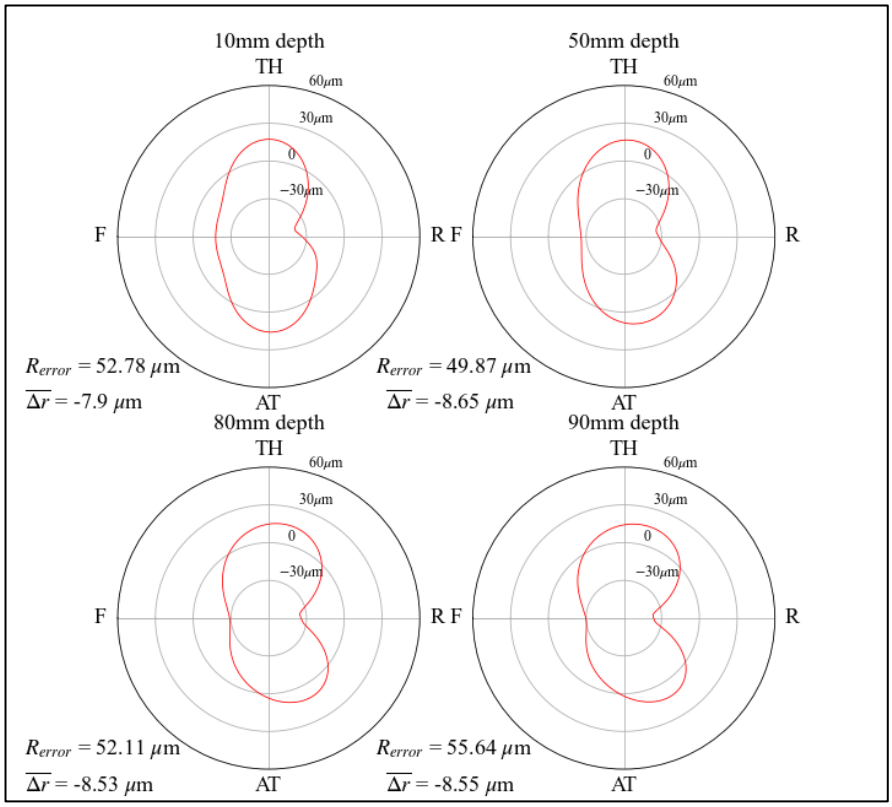

Fig.16 temperature scale is 0.95 using TEC estimated by Dohee Y

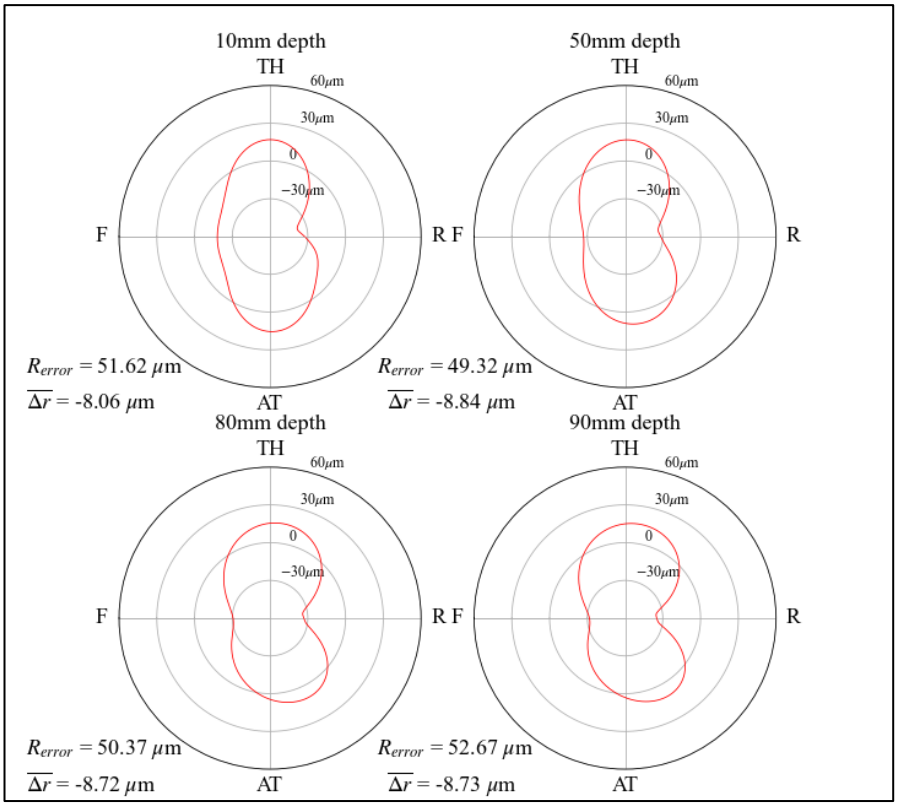

Fig.17 temperature scale is 0.9 using TEC estimated by Dohee Y

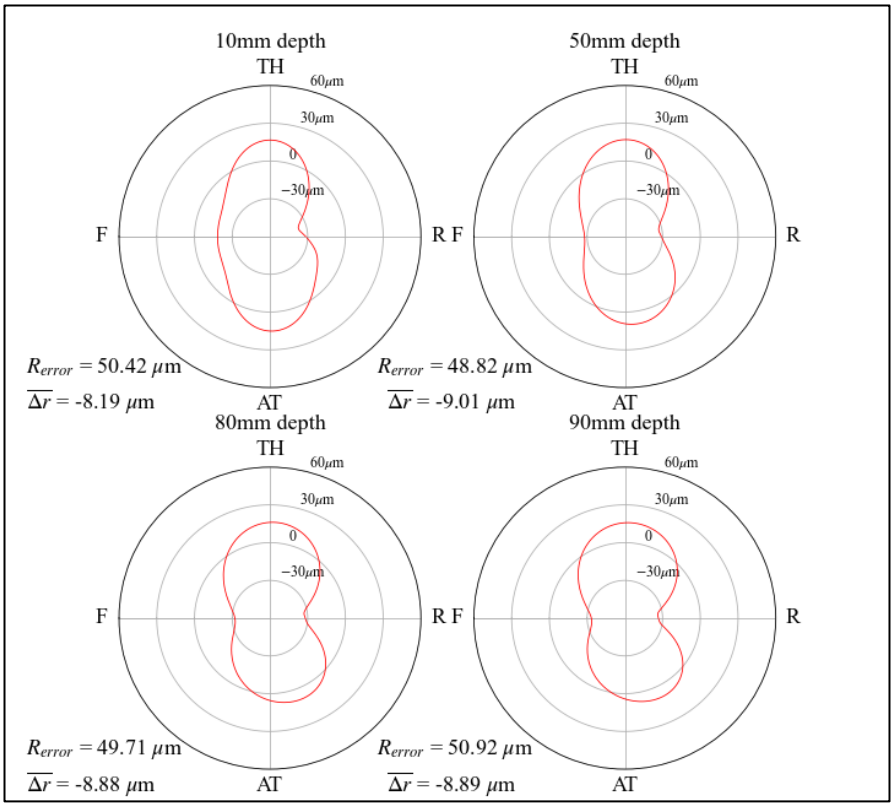

Fig.18 temperature scale is 0.85 using TEC estimated by Dohee Y

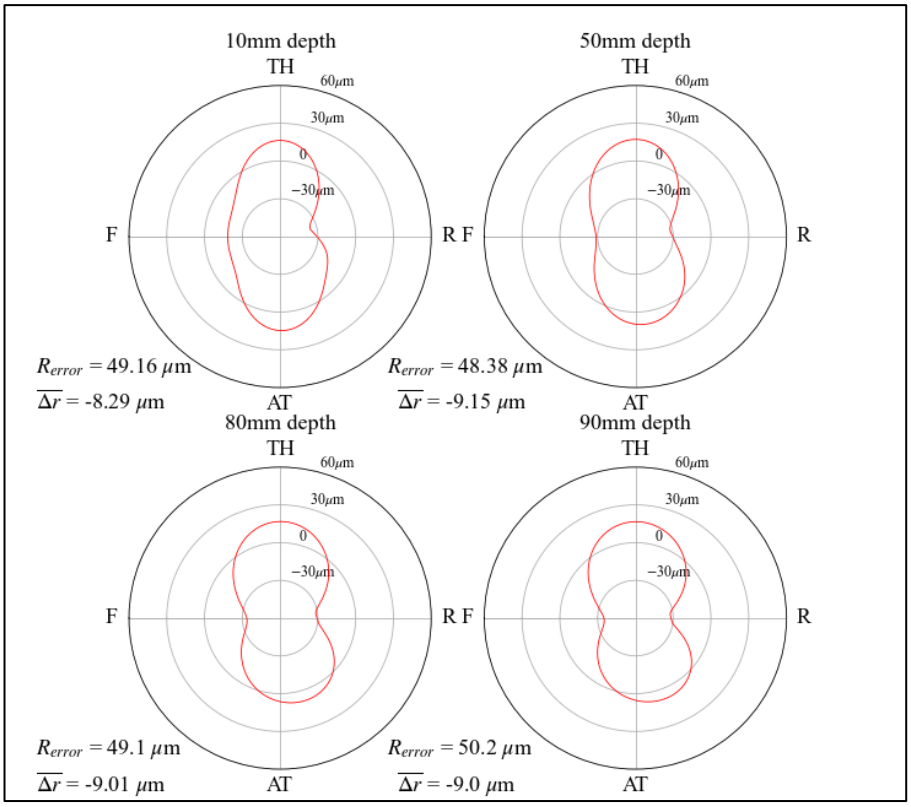

Fig.19 temperature scale is 0.8 using TEC estimated by Dohee Y

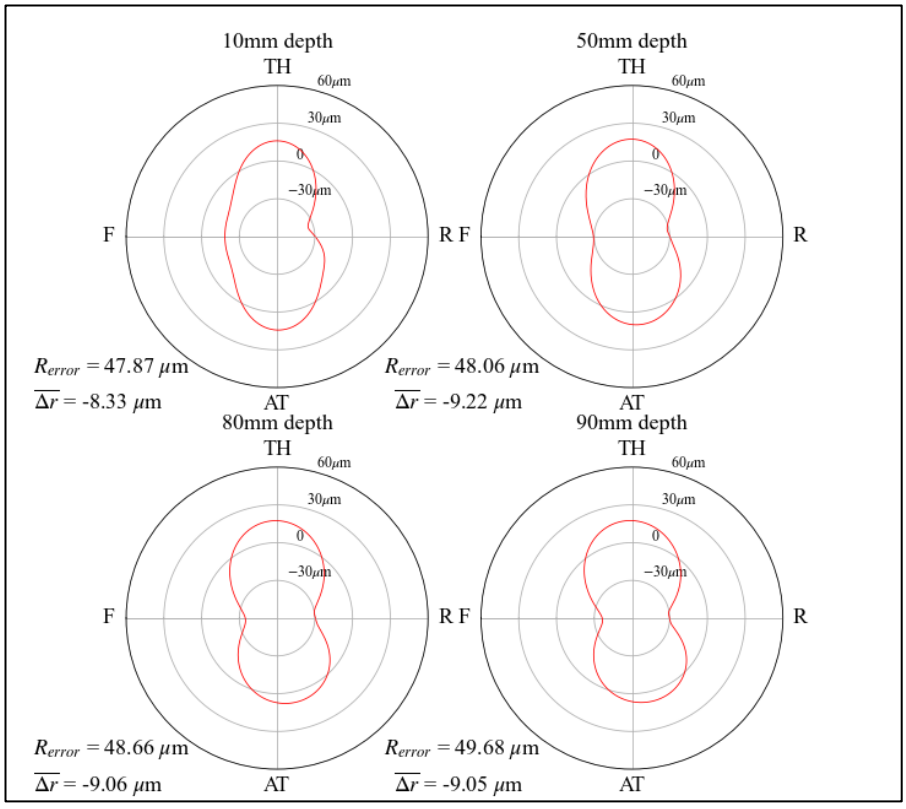

Fig.20 temperature scale is 0.75 using TEC estimated by Dohee Y

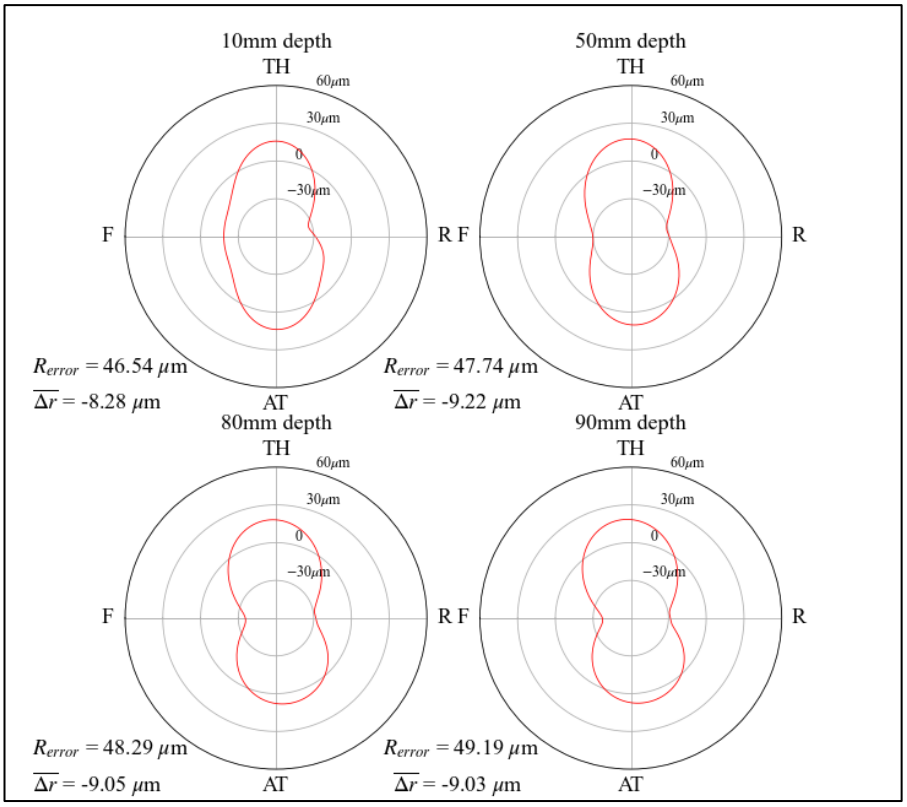

Fig.21 temperature scale is 0.7 using TEC estimated by Dohee Y

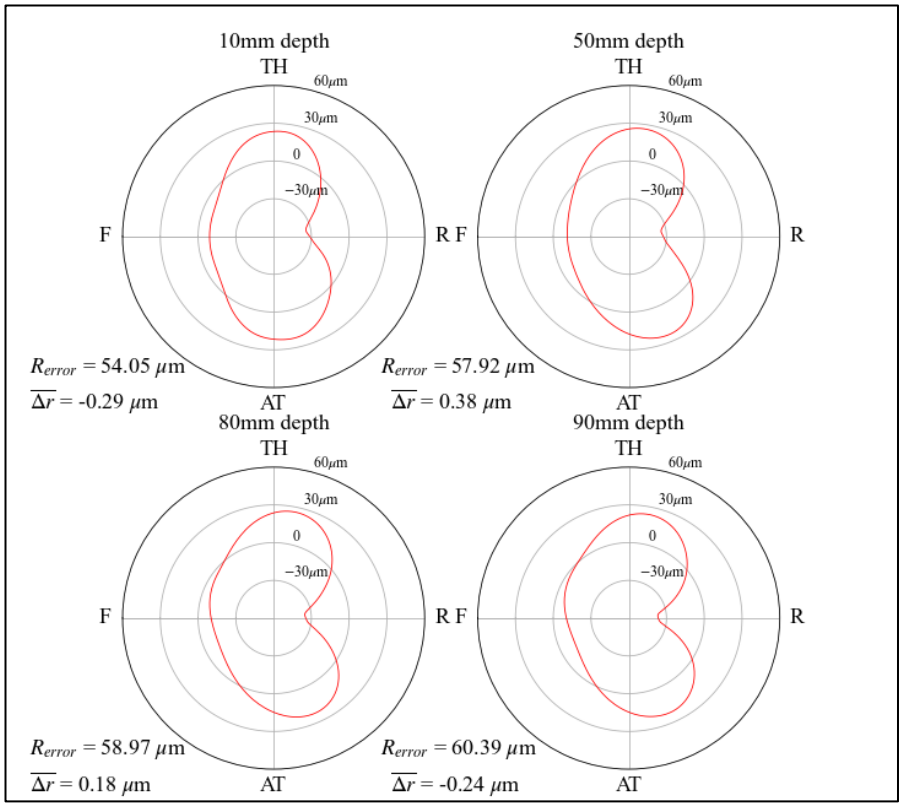

Fig.22 temperature scale is 1.0 using TEC estimated by Shibing T

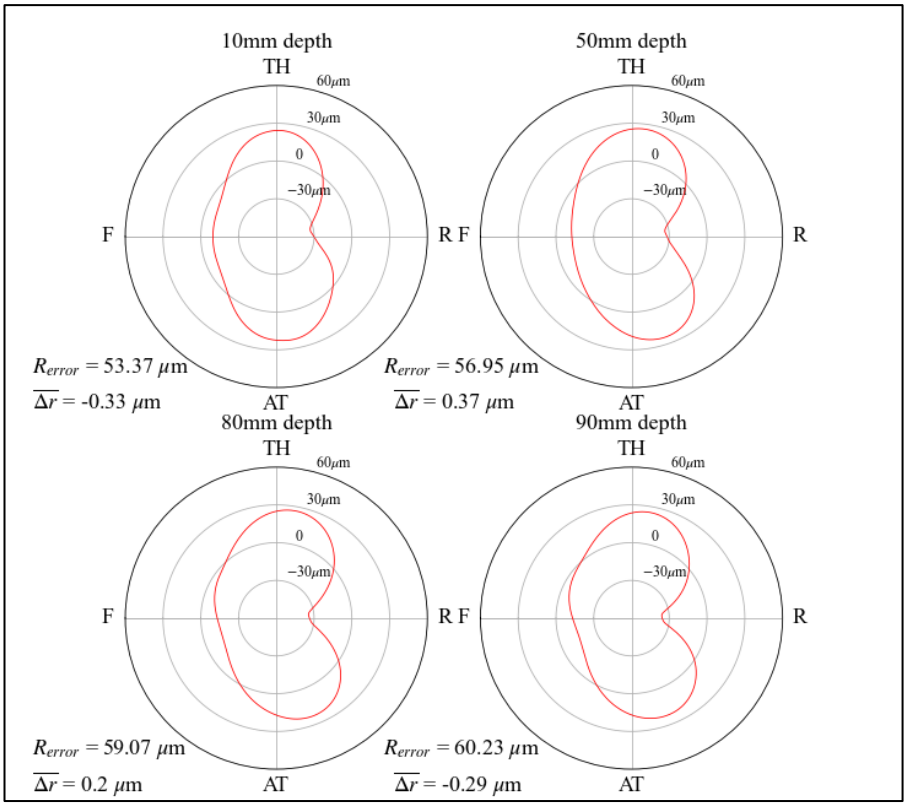

Fig.23 temperature scale is 0.95 using TEC estimated by Shibing T

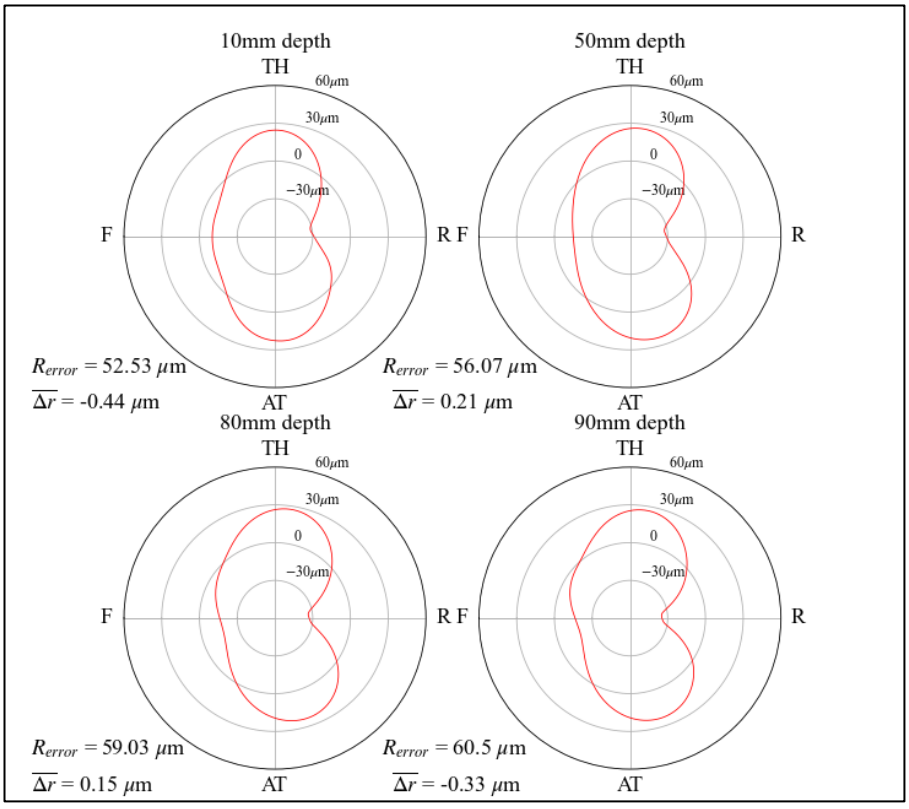

Fig.24 temperature scale is 0.9 using TEC estimated by Shibing T

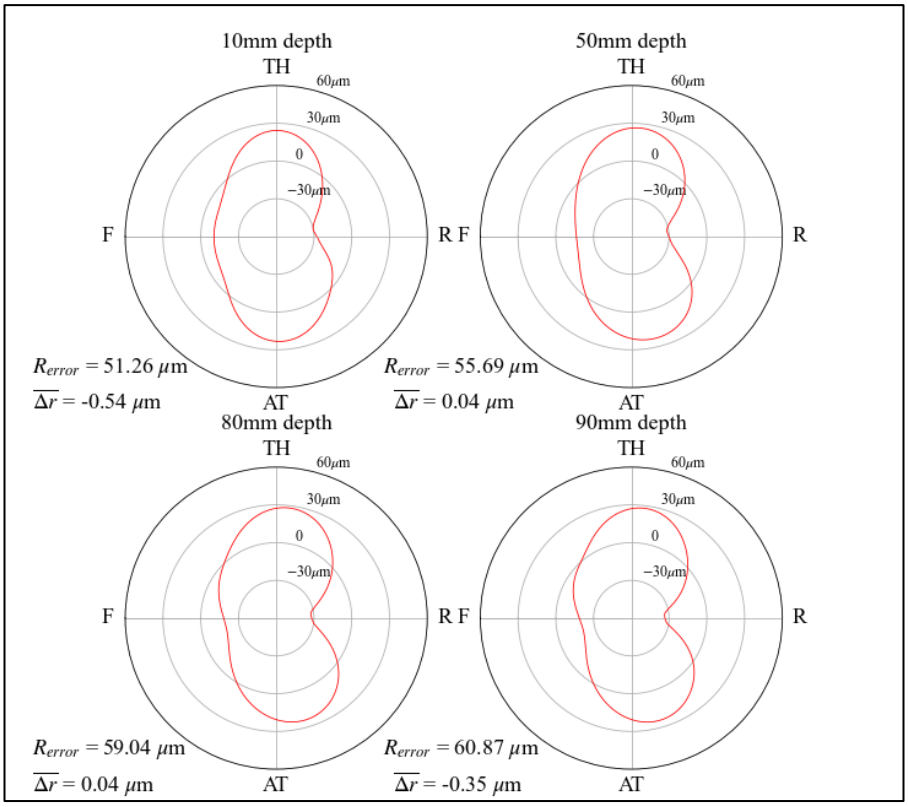

Fig.25 temperature scale is 0.85 using TEC estimated by Shibing T

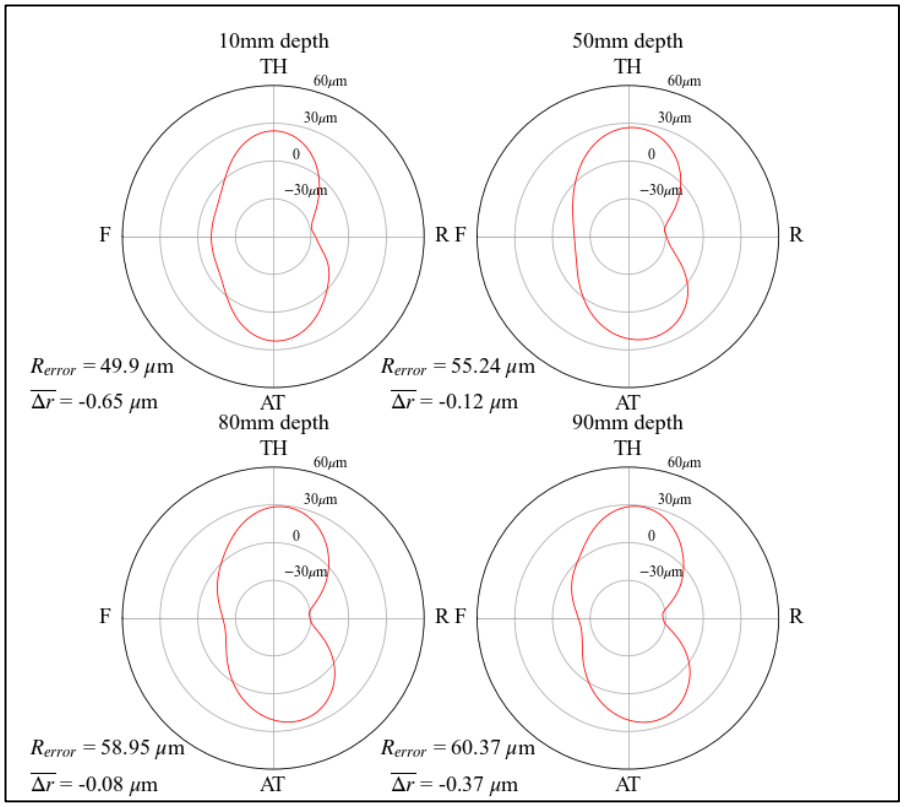

Fig.26 temperature scale is 0.8 using TEC estimated by Shibing T

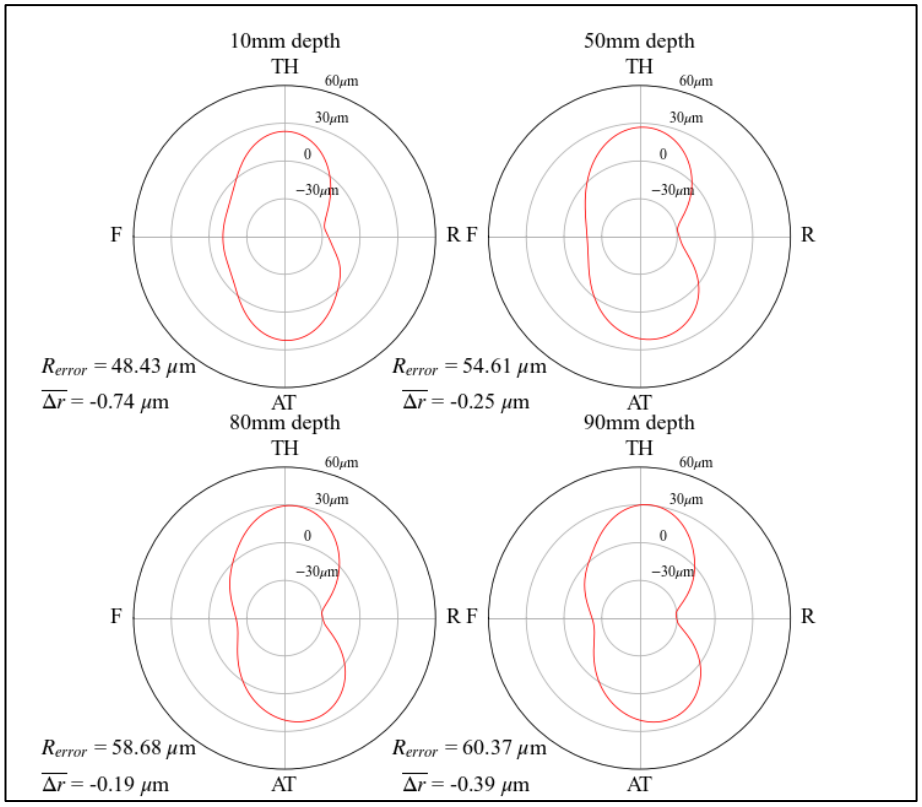

Fig.27 temperature scale is 0.75 using TEC estimated by Shibing T

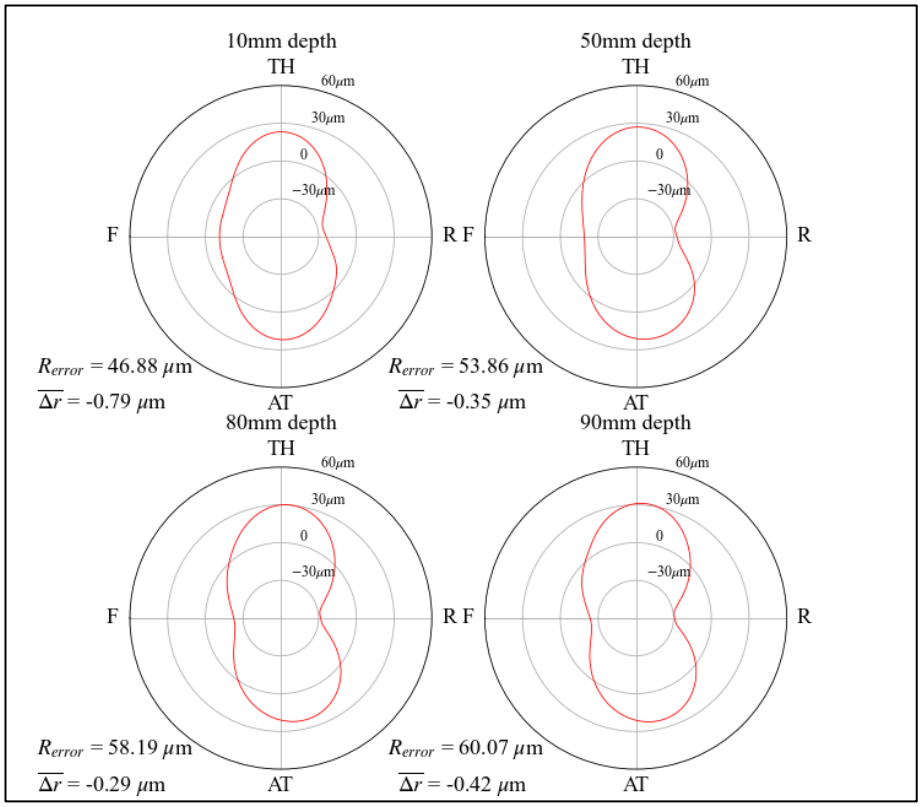

Fig.28 temperature scale is 0.7 using TEC estimated by Shibing T